DISSERTATION

OPTICAL LATTICE DECELERATION OF A CRYOGENIC METASTABLE ATOMIC HYDROGEN BEAM

Submitted by

Samuel F. Cooper

Department of Physics

In partial fulfillment of the requirements

For the Degree of Doctor of Philosophy

Colorado State University

Fort Collins, Colorado

Summer 2023

Doctoral Committee:

Advisor: Dylan C. Yost

Jacob L. Roberts
Martin Gelfand
Alan Van Orden

ABSTRACT

OPTICAL LATTICE DECELERATION OF A CRYOGENIC METASTABLE ATOMIC HYDROGEN BEAM

Hydrogen is the most abundant and simple naturally occurring element in existence, making it an ideal platform for study of fundamental atomic physics. Theoretical physics has the capacity of making extraordinarily precise predictions of atomic hydrogen's energy levels, owing to hydrogen's innate simplicity. To provide valuable new information to the theoretical models, such as definitions of fundamental constants, requires pushing experimental measurement of these energy levels to extreme precision, and obtaining experimental values that agree or disagree with theory provide a rigorous test of fundamental physics. Unfortunately, hydrogen has yet to benefit from the advent of laser cooling and trapping techniques pioneered in other species due to the prohibitive ultraviolet wavelengths required. As a consequence, modern best measurements to-date are limited by uncertainties due to thermal energies of atomic hydrogen samples. The next generation of ultra-high precision experiments will require new ways to obtain slow and or cold atomic hydrogen. This work contains progress made towards this goal, where advent of a novel high power UV radiation source on this experiment opened the viability for exploring new horizons. Specifically detailed in this dissertation are the efforts toward generating a cryogenic helium temperature beam of metastable (2S) atomic hydrogen with velocity characterization and a first ever demonstration of a novel, all-optical deceleration method which utilizes an electro-optically controlled far detuned optical lattice. In the proof-of-principle experiment a velocity selected portion of the atomic hydrogen beam was decelerated from 300 ms^{-1} to 280 ms^{-1} in a single 30 ns optical pulse.

ACKNOWLEDGEMENTS

In the completion of this work, and all of the moments leading up to this point, I am deeply indebted to many people who've guided me and perhaps even carried me through the rough patches along the way. Wholeheartedly, I recognize that no part of what I have completed or accomplished in life comes from a solitary and isolated effort and I owe it all to my family and community who awarded me with the privileged opportunities I've been so fortunate to enjoy. While attempting to write a few lines of text to entirely capture my thanks is futile, it is entirely worth doing the best I can. First and foremost, I want to thank my parents Patrick, Sarah, Lana and Keith, and my brother Arthur. At the core of who I am, they have contributed the most to, no created, who I am as a person and the value system that I live by which delivered me to this place and pursuit. I am sincerely grateful for my Father, Patrick, whose curious drive, and thoughtful playfulness, I value. My Mother, Sarah, whose confidence in character I hope to embody. Lana, for her kindness and perseverance, and for domesticating my father while still encouraging him to dive into his projects fully. Keith, for your example, to work hard, and know what to value and where the bounty gained through sacrifice is worth the cost. Most of all, Arthur, for being a role model of boldness, resilience, toughness, and force of will. Though younger than me, I've certainly spent most of the time looking up to the way he remains unapologetically himself. Thank you for the years of play, the years of example, and the future of brotherhood.

I cannot go any further into these acknowledgements before I express my deep gratitude to my advisor, Dylan Yost, for all that he did, all that he put up with, and the incredible opportunity he awarded me in taking me into his group as a student. To be allowed to train as an apprentice under Dylan's guidance, competent master of a niche specialized technical craft, is the rarest of privileges I cannot possibly take for granted. Viewed in this way, Dylan as professor of knowledge and a master of what he knows, he by no means had any obligation to take on training me as his student. For Dylan, who has all the responsibility of a university professor, I am incredibly grateful for the substantial amount of energy he had to expend to first teach me what it even means to get a

PhD, let alone what it takes to bring me up to the point of being even remotely useful, especially with how utterly clueless I was when I started. Thank you for showing me how, by example, to leave as few questions up for the "experts" as possible, and not to be afraid of digging into all of the little black boxes we take for granted in technology daily and having confidence that there is always a simple, intuitive picture for understanding how anything works. To Dylan, however, I am most indebted I am indebted for the precise application the law of diminishing returns, or the 80-20 rule – the practice that 80% can be accomplished with 20% of the effort, or sometimes, to complete the last 20% of effort, another 80% must be applied. I know I never fully passed this class, and still struggle to apply it usefully in my daily life. In due time, however, I hope to never spend an hour or two of my work day researching the definitions and analysis of fastener standards and instead apply this same level of interest and attention to detail in the direction of useful, important, and equally interesting problems of consequence. Thank you for your patience over the years maintaining a mentorship with me.

But truly, as in any good quest, the value in the end is not reaching the goal, rather it's contained in the friends we make along the way. This endeavor is no exception. I could not possibly have persevered the challenges of adult life and a getting a PhD without the incredible group of friends I made in the very special place of Fort Collins, CO. It would be hard to name and thank everyone I love and was impacted by over the course of grad school, so anyone I leave off this list, know for certain I don't take you for granted, and I hope that I can show my thanks in other ways. Firstly, my lab cohort, Adam Brandt, Cory Rasor, Zak Burkley, Ryan Bullis, Will Tavis, Lange Simmons, Scott Johnson, and Chase Mallory. Adam, thank you for all of the physics conversations. I think much of my insight into how things work IRL can be attributed to the uncountable number of interactions we had since starting as labmates, roommates, and office mates over the years. Especially once the anger detected in the responses died down, hah. Cory, thank you so much for all of your help over the course of every project in the lab. I'm not actually sure what would have been finished or successful without you. Also, thank you for literally being better than me at every hobby we share, it really helps to be pushed in this way and I honestly will miss the days when we could

easily climb at Horsetooth in the morning, play billiards at Match-ups Monday night, or just get a limit bouldering session it at Whetstone or Ascent after a long day in the lab. Zak, thank you for the days and nights you worked to make the 243 system a reality. That laser truly is the workhorse of our lab and without it, nothing we have done since could be possible. Ryan, what a guy. How do you work so hard? Thank you very much for coming in so frequently, working diligently, being helpful, and staying so late on the days we could collect data. It was seriously such a great benefit to have you join the group and I can't wait to see what you accomplish in your time in Dylan's lab. More importantly however, thanks for kicking my a** at basketball and the many games of 7's we got to play in the short time we overlapped, I'm looking forward to continuing these traditions. Will, thank you for carrying the torch on this project, I hope it is incredibly successful and you get to demonstrate what will become some of the most important experiments in atomic hydrogen research. Lange, I literally could not have coded half of my research without the couple of key important lessons you gave me on computer science, data structures, programming, Monte Carlos, Runge-Kutta, Symplectic integration, and efficient tabulation over loops. I can't believe how much I learned from you in the short time we had to work on the project together. Scott, thanks for the super rad day out in Eldo and all the super fun nights talking about rad climbing topics and shooting pool at Match-ups. Chase thanks for the fun days out with photography and the cool conversations we got to have about drone flight and robotics. To my incoming graduate class cohort, how could I possibly have survived the homework and exams? I don't think I would have, but with Chase, Alex, Emmett, Katie, Logan, Ramesh, Zak, Matt, Adam, Kahl, instead of just survival these evenings are remembered with great fondness and many laughs. Pascal, thank you for being the chillest roommate ever, and for all of the absurd philosophical dives we took at random times of the week. It was always great to get some of the existential and angsty knots verbalized. Emmett, it has always been fun to talk about planes, trains, automobiles, and movies with you. Gus, thank you for all of the cryogenic technical help, as well as the good times running and hanging out at 209. Julie, thanks for the hilarity that was 209 and the great list of workouts to do during the lockdown. Without you I could not have stayed in shape in those years. Ski-cation

scientist crew, Weston, Annalise, Matt, Gus, Adam, Julie, Chase, Jaz, thank you for the repeated year after year of memories. I hope those trips never stop. Jaime, Marc, Callie, Vallen, Jamie thank you for all of the laughter, exciting adventures and friendship that you have granted me with. You have made life a beautiful time even when I'm struggling and I look forward to an indefinite celebratory future.

To my family, all of you, thank you so much for your kindness, care, love, patience and support.

FOREWORD

In the post-war summer of 1947 at a particularly famous conference in Shelter Island, NY, two measurements made by microwave techniques performed on hydrogen that were generating all of the chatter (see [1], p. 290). This conference was the first time in 5 years that some of the world's most notable physicists were able to meet together and discuss the future of science without the menace of war. The guestbook included names like Bethe, Schwinger, Oppenheimer, Feshbach, and Feynman to name just a few. With such a cast, and such a task as determining the future of physics, it might sound a bit surprising that a microwave spectroscopy experiments were the shows on center stage, at least, not already knowing the history (see [1] for a historical article on the Shelter Island conference). It was two measurements of anomalies shaking up the world as it was once known. The first being hydrogen's anomalous $2S_{1/2}$-$2P_{1/2}$ splitting presented by W. E. Lamb [2], and the second a hint of an anomalous electron magnetic moment (see [3] for a quick read on the anomalous magnetic moment of the electron) in hydrogen's hyperfine spectrum by I. I. Rabi [4]. These findings were not so controversial because of the cleverness of the measurement per se, rather it was the revolutionary implications discovered in the precise experiments. What was found by Lamb and Rabi residing deep in the spectrum of hydrogen, signaled indisputable anomalies in the hydrogen energy spectrum which were so tiny they were previously imperceptible, was the birth of Quantum Electrodynamics (QED) which ultimately put physics the path that led to the Standard Model (SM).

This example is just one out of a pattern of advances sparked by studying hydrogen dating as far back as the 1880s and the observations of solar spectroscopy (See Rigden, J.S. Hydrogen: The essential element. Harvard U. Press, Cambridge, Mass. (2002) for a great storyline on hydrogen's role in the development of quantum mechanics.). The known spacing of the hydrogen spectrum took decades for a truly quantitatively predictive model to come to light – scientific theories having shifted over the following years from plum pudding to Saturnal rings. Finally in 1913, the impressively successful Bohr model of hydrogen's gross structure was able to explain the empiri-

cal determined Balmer formula and in doing so unraveled the underlying scaling constant in terms of more fundamental quantities. Despite all of its success, the Bohr model still could not explain the similarly long standing observation of a "fine structure splitting" within the gross spectral structure of hydrogen. This puzzling spectral splitting would endure many years without a solution until the stroke of genius by P. A. M. Dirac in 1928 with the formulation of his famous relativistic wave equation. Dirac's equation was truly remarkable in all that it was able to accomplish. Two major successes being, that it could predict the fine structure splitting to better than a part per million and explain the degeneracy breaking as an relativistic interaction of the electron's intrinsic spin and its own orbital motion, and to some, one of the greatest victories of theoretical physics with the prediction of the anti-electron, or positron, nearly a decade before its discovery. With Dirac theory having such success, the 1947 Lamb shift discovery was certainly shocking. Yet, the presence of even finer underlying details in the hydrogen spectrum anomalous to the elegance Dirac theory opened wide a door leading to a world of new and untested realms of natural law in the creation of QED.

For physics to progress, one direction physicists may go is to study a system as simple as possible – where as much of the complexity has been stripped down as far as it can be so that all of the phenomena remaining is that which is fundamental. In terms of naturally occurring matter, it doesn't get simpler than the hydrogen atom: a single electron bound to one proton by the coulomb interaction. It's this simple structure and its overall abundance that allows hydrogen to remain at center stage in the development of modern physics for more than a century, and to continue to be the platform where we return to test our understanding and probe deeper for new laws. Again, as new experiments have pushed up against the the limits with how precisely the energy level spectrum can be resolved, the field has uncovered the scent of yet another revolution in physics.

DEDICATION

Dedicated to my brother, Arthur.

TABLE OF CONTENTS

LIST OF FIGURES

Chapter 1

Introduction

The energy levels of hydrogen can be written down as

$$E_{nlj} = hcR_\infty \left(-\frac{1}{n^2} + f_{nlj}(\alpha, \frac{m_e}{m_p}, ...) + \delta_{l0}\frac{C_{NS}}{n^3} r_P^2 \right), \tag{1.1}$$

where R_∞ is the Rydberg constant is one of our best known fundamental constants, and the first term of eq. 1.1 is the gross energy band structure stemming from the Coulomb potential. The $f_{nlj}(\dots)$ term accounts for the fine structure splitting and lamb shift by taking into account corrections due to Dirac theory, hyperfine splitting, reduced mass effects, and QED loop corrections [15, 16]. The final term in eq. 1.1 contains the remaining portion of the Lamb shift containing a correction to the energy levels given the finite size of the charge distribution of the nucleus, r_P. The constants α and the electron-proton mass ratio, m_e/m_p, are determined in precision measurements in other systems [16] leaving the Rydberg constant and the RMS charge radius, r_P to be determined by measuring separate E_{nlj} in hydrogen. The Rydberg constant is related to a list of fundamental constants as

$$R_\infty = \frac{m_e e^4}{8\varepsilon_0^2 h^3 c} = \frac{m_e c \alpha^2}{2h}, \tag{1.2}$$

which through these the relationships that this makes the precise determination of R_∞ a method of staking down the value of α and providing for self consistency within QED. Aside from the inherent interest in high precision measurements r_P as a sensitive test of Quantum Chromodynamics (QCD) calculations on the lattice, precision measurements of R_∞ and r_P allow for tests of QCD [17].

Theoretical QED calculations have spectacular precision despite the slow convergence of higher order corrections only scaling by powers of the fine structure constant, $\alpha \approx 1/137$ This allows precision measurements to be compared to very high precision theory predictions. One textbook example of a high precision bound state QED calculation is that of the hydrogen $2S_{1/2} -$

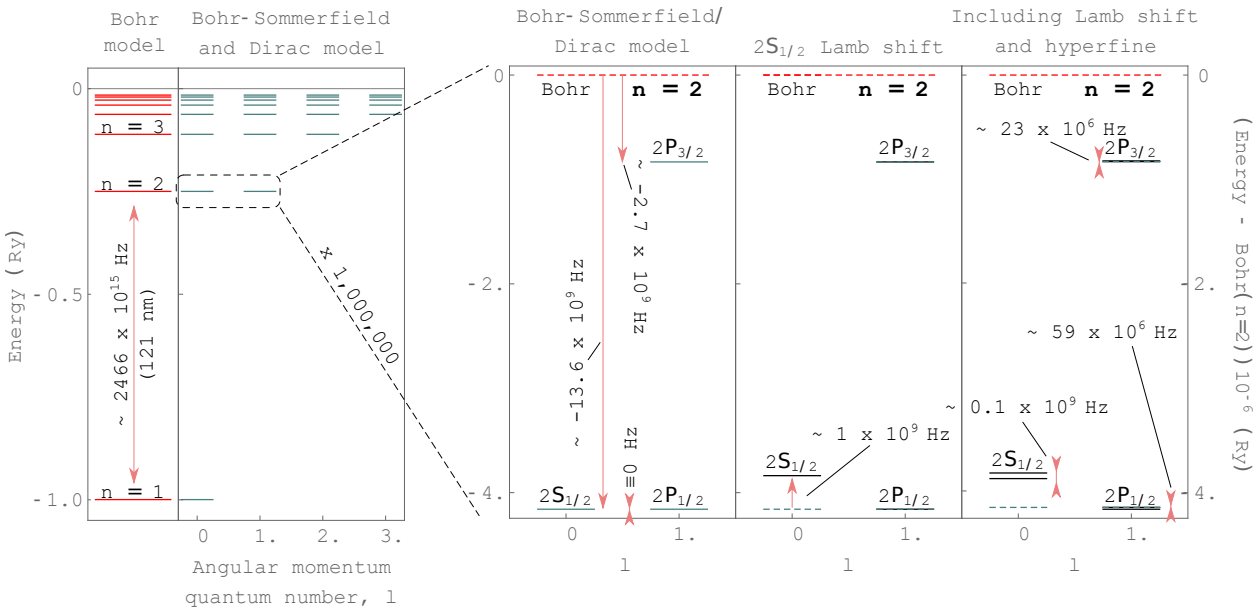

Figure 1.1: The increasing precision of theoretical models in hydrogen drawn to scale. The semi-classical Bohr model explains the gross structure of hydrogen and birthed the concept of quantized energy orbits where the electron must only transition by integer sized jumps to release the light as was previously observed in the Balmer spectrum. Observations of a million times finer quantized structure of the hydrogen emission spectrum had already been observed, and the first extension to the Bohr model by Sommerfield included higher angular momentum elliptic orbits and the relativistic change in mass energy which lead to the first the prediction/explanation of this fine structure splitting. The Dirac theory followed Sommerfield's elliptic orbit model, but fully included special relativity and greatly expanded on the Schodinger picture of the atom. However a measurement of the Lamb shift in 1947 proved Dirac theory to not be the complete picture, and even finer splittings occur due to the interaction between the nuclear and electron spins.

$2P_{1/2}$ energy splitting, dubbed the Lamb shift. As seen in the zoomed in window of fig. 1.1, the 1 GHz energy splitting is very finely resolved against the backdrop of the overall hydrogen gross structure. Each of the terms contributing to this interval are tabulated in detail in [16, 18, 19] and the references therein. This remarkably small splitting can be calculated to the absolute precision of 300 Hz, and involves nine separate expansion terms which are separately plotted in fig. 1.2 for values prior to 2010 (updated measurements are in a later figure).

Calculation of the hydrogen Lamb shift requires very few input parameters, one of them being the measured proton RMS charge distribution, r_P which may be established by QCD calculations of the quark-gluon sea that composes the proton. However, due to the challenges theorists face in QCD calculations, prior to 2010, the best Lamb shift calculation required the proton charge distribution to be determined through fits of world hydrogen spectroscopy data or electron proton

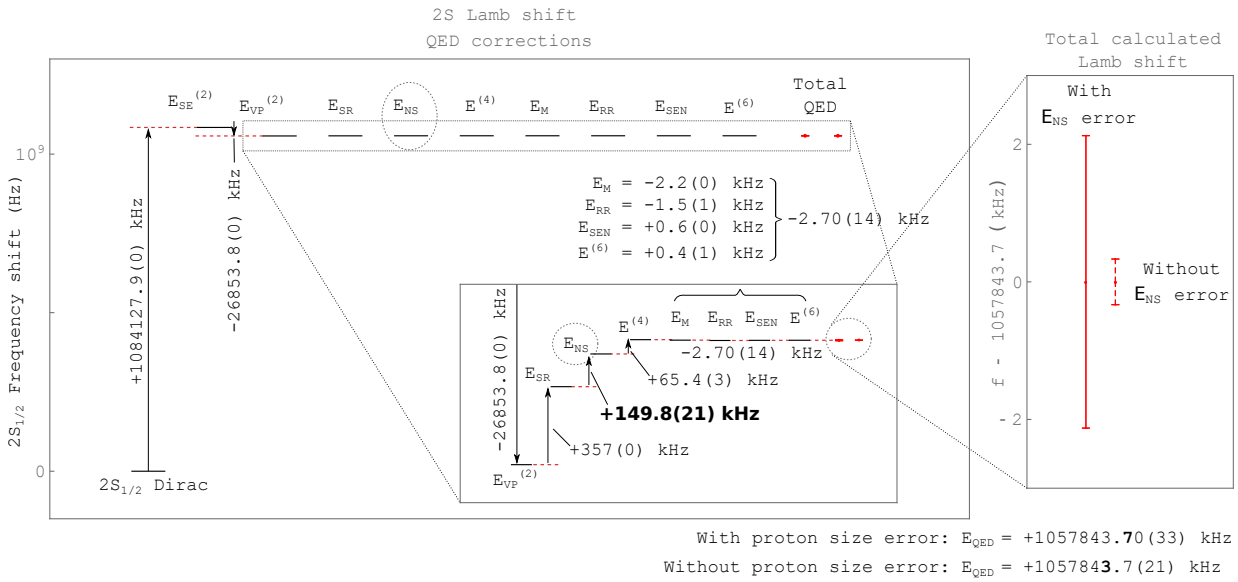

Figure 1.2: Hydrogen 2s level Lamb shift contributions. QED effects that contribute to the 2s Lamb shift include Dirac reduced mass shifts E_M, relativistic recoil E_{SR} , electron self energy $E^{(2)}_{SE}$, polarization of the vacuum $E^{(2)}_{VP}$, two and three-photon self energy $E^{(4)}$ and $E^{(6)}$, radiative recoil E_{RR}, proton self energy E_{SEN}, and RMS proton charge distribution E_{NS}. Values were obtained from [5] and are plotted to scale. The majority of the 2S Lamb shift contribution comes from the electron self energy, and although the last four corrections, E_M, E^{RR}, $E_{(SEN)}$, and $E^{(6)}$, don't visually appear to be significant, they total to a -2.7 kHz with a significantly smaller uncertainty, at 140 Hz, than the proton charge distribution contribution of 2.1 kHz. This large error in the term E_{NS} which derives from the hydrogen spectroscopy determination of r_P motivates the greater precision of the muonic hydrogen determination of r_P so that more precise higher order QED calculations are not rendered overwhelmed.

scattering experiments [18]. At the time, further high order QED corrections could not be applied because the theoretical uncertainties were limited by the experimentally measured proton radius. This is easily seen in fig. 1.2 for the uncertainty of the E_{NS} term which dominates the overall calculation uncertainty [20–23]. A measurement with improved precision of r_P was necessary to to progress further which in turn would lead to an even more precise determination of the Rydberg constant [20]. As the effect of the RMS proton charge radius correction scales by the lepton reduced mass as m_r^3 [24], the perfect way to determine the proton size is to perform spectroscopy on muonic hydrogen and gain a factor of 8 million increase in sensitivity to r_P due to the 207 times greater mass. When the findings at Paul Sherrer Institute (PSI) were published in 2010 [25], and repeated in 2013 [24], the measurement repeatedly established a value of r_P discrepant from all previous normal hydrogen data by 7σ [24]. A plot of the at-the-time new muonic hydrogen proton

radius determination against the hydrogenic world data is shown in 1.3 where the uncertainty in the muonic and hydrogenic proton radius is the shaded red and blue regions respectively. This large statistically significant discrepancy between muonic and normal hydrogen is the proton radius puzzle, see for example [24, 26] for detailed reviews of this subject.

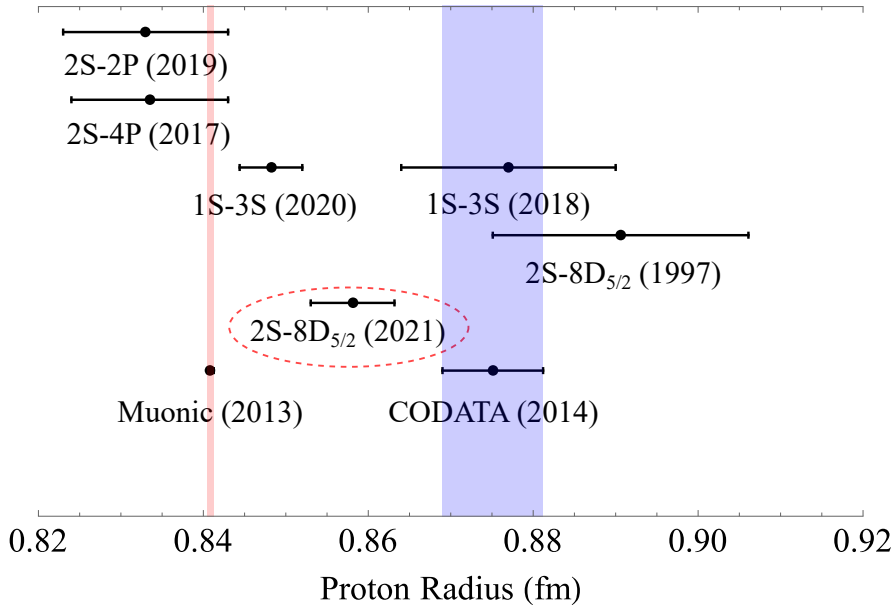

Figure 1.3: A selection of result determination of the proton radius when combined with the 1S-2S transition [6], with our determination circled. The uncertainty for the muonic value is the width of the red line, as compared to the world hydrogen which is the width of the blue.

The explanation of the puzzle could come in multiple ways. One way this could be is that the QED calculations for the $f_{nlj}(\dots)$ are not accurate. However, as claimed in [24] these values have been repeated by multiple groups and checked and rechecked making this justification highly unlikely. An exciting explanation could require starting afresh with questions about the foundational physics assumptions that our theories are currently based on e.g. lepton universality. Lepton universality has also been questioned in recent high precision measurements of the muon anomalous magnetic moment (g-2) which is also highly discrepant from the electron g-2 [27, 28]. Of course a revolution of physics from a fundamental level is not to be taken lightly, and so new and repeated measurements need to be made. If the solution to the proton radius puzzle were to lie in experiment, it would point to an unknown correlated systematic existing in the previous hydrogen

which demands new measurements and a re-measure of some of the most problematic data (as the muonic measurement being incorrect is significantly improbable). As shown in fig. 1.3, a number of measurements have come out since the muonic experiment, including one from our group (2S-$8D_{5/2}$ [8]). As is evidenced by the 2017, 2019, and 2020 hydrogen measurements, there has newly been some strong agreement with the muonic value [29–31].

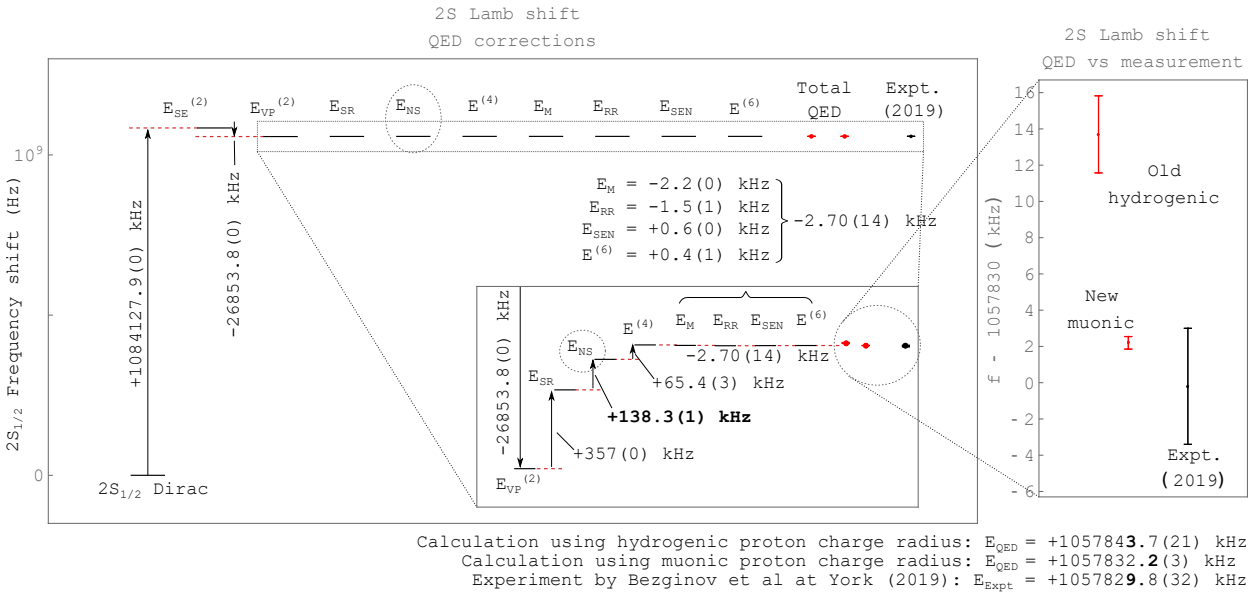

Figure 1.4: Hydrogen 2s level Lamb shift calculations using the muonic hydrogen determination of the RMS proton charge radius as input. The 2019 measured value strongly excludes the hydrogenic determination of r_P. Values were obtained from [5] and are plotted to scale.

Figure 1.4 shows the newest lamb shift measurement (2019) [31] compared to the calculations using both the original 2014 hydrogenic proton size versus the more precise muonic value as input data. As is readily apparent in the good agreement with the calculation using the higher precision proton size, it would seem that evidence is leaning toward an experimental solution to the proton radius puzzle, and the muonic hydrogen value should be assumed to be the correct one. Taking this value as the correct RMS proton charge radius brings up a secondary curiosity however. Our determination of the proton size circled in red in fig. 1.3 lies closer to the muonic value than the previous one from Paris, it still was discrepant by 2.2σ. In fact, from [8] it would seem that many of the transitions involving higher lying n and l states tend to be shifted preferentially toward larger pro-

ton radii. Cast in a different light, if one assumes the proton radius measured by muonic hydrogen, the Rydberg constant extracted from these measurements are shifted. In this case, the hydrogen atom serves as a high precision testing ground for the potential variation in the Coulomb potential at close range since the Rydberg constant is the natural scaling to the electrostatic potential. Variation in the parameter that may depend on quantum numbers would then be an indication of an intrinsic short range screening. As shown in fig. 1.5, when the Rydberg constant determined from the hydrogen spectroscopy measurements are plotted assuming the muonic hydrogen proton size as shown in fig. 1.5 there is an suggestive trend for the higher n transitions toward higher Rydberg constant. As mentioned in [8] and discussed in [7, 32], the variation of the Rydberg constant over inter atomic distances could arise from the existence of a massive boson which couples the proton to the electron and modifies the coulomb interaction. When a Yukawa correction is included, the Rydberg constant extractions from the Hydrogen data show a better agreement, as shown in fig. 1.5b.

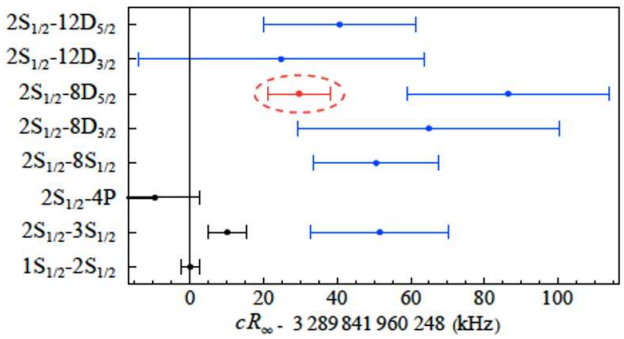

(a) Rydberg constants determined by hydrogen spectroscopy.

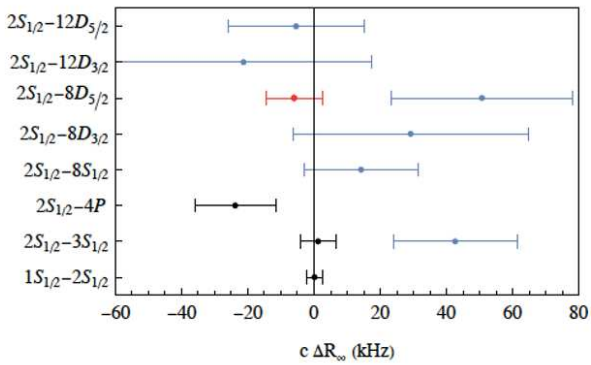

(b) Rydberg constants with Yukawa modification.

Figure 1.5: (a) The Rydberg constant determined by hydrogen spectroscopy data assuming the muonic hydrogen proton charge radius as input data. The higher lying n states clearly are shifted from 0. (b) If the Coulomb potential due to the proton is modified by the precense of a massive boson to reflect a Yukawa potential for close range interactions, the scatter in Rydberg constant variation in the hydrogen data may be reduced. This is discussed in [7,8] as a potential underlying new physics in precision hydrogen spectroscopy.

Maybe this points to an unknown correlated systematic, or it could again be some other problem with the theory. Regardless of the explanation, new measurements with new techniques are

needed. There are other proposed searches for beyond standard model (BSM) physics using hydrogen [33] which also require diving deeper into the atomic spectrum than is currently routine. To accomplish this task, experimental techniques must enter into a new paradigm where hydrogen atoms can be manipulated with great control. To date however, perhaps the most effective AMO tool in manipulating atoms, laser cooling, has been moslty out of reach of precision hydrogen spectroscopists for decades. Motional systematic effects that tend to be negligible in many heavier single valence species because the samples may be cooled to very low temperatures tend to dominate in hydrogen.

Table 1.1: Three of the highest precision transition measurements performed on atomic Hydrogen. Fractional uncertainties better than a few parts per trillion were obtained, however, limiting systematics still relate to atomic motion. This includes the 2S-8D measurement, where probe laser power is the root cause of the AC stark shift, but for a given atomic signal, the laser intensity could be scaled down if the atoms transit times through the beam were longer.

Transition	Measured value	Fractional uncertainty	Limiting systematic	Citation
1S-2S	$2,466,061,413,187,035(10)$ Hz	4.2×10^{-15}	SODS, TOF	[6]
1S-3S	$2,922,743,278,665.79(72)$ kHz	2.4×10^{-13}	Residual Doppler	[30]
2S-8D	$770,649,561,570.9(2.0)$ kHz	2.6×10^{-12}	AC stark	[8]

As an example, a selection of the three highest precision hydrogen spectroscopy measurements to date are shown in Table 1.1 with remarkable demonstrations of fractional uncertainty in the range of a few parts per trillion or better. The limiting systematics can often be traced to the atomic motion. In the case of the 1S-2S and 1S-3S measurements done at MPQ, the largest uncertainties reported were residual Doppler shifts and statistics, which in essence can be cast as a consequence of time-of-flight broadening and limited signal to noise ratio for the transition signal. Due to hydrogen's relatively light mass, the cryogenic samples used in those experiments (on the order of 5-6 K) have mean velocities centered at 300-400 m/s. Using a clever method of measuring slower that thermal atomic velocities, the MPQ group was able to resolve a second-order Doppler shift of **2.4 kHz** on a 1 Hz line for the 1S-2S measurement [6]. In the case of the 1S-3S measurement,

Grinin et al reported the most significant uncertainty being the second-order Doppler effect and the residual first order Doppler effect due to the coupling of atomic motion to the frequency chirp of the laser pulses [34]. In the 2S-8D measurement done at CSU [8], the limiting systematic is the AC stark shift which is not immediately recognizable as a velocity or motional systematic effect. However, the AC stark shift arises due to the high intensity of the laser power required to excited the two-photon 2S-8D transition and is characterized through an extrapolation of the laser line center as a function of laser power (intensity). If instead the atoms were transiting the probe lasers at much lower speeds, or instead residing within a magnetic/optical trap, then the laser powers can be significantly reduced to excite the transitions dramatically reducing the effect of AC stark shifts.

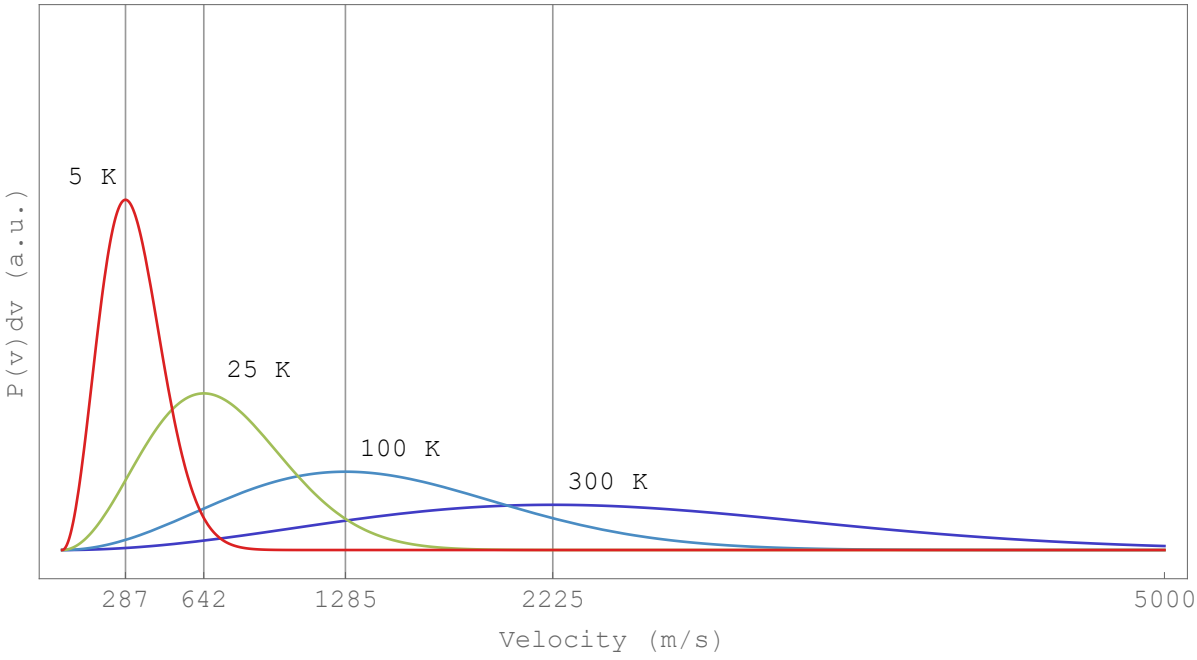

Figure 1.6: Velocity distribution for atomic hydrogen at a few temperatures ranging from 300 K down to 5 K. Even at the lowest temperatures practically reached without laser cooling or the aid of a dilution refrigerator around 4-5 K, the most probable atomic velocity is $300\,\mathrm{m\,s^{-1}}$.

Where many AMO experiments have laser cooling and trapping available to improve control, this is not typical in hydrogen. This is because hydrogen's natural laser cooling transition (1S-2P) require VUV radiation at 121 nm which is extremely challenging to produce, and is exacerbated by the high velocities of hydrogen at room temperature due to its tiny mass. For example, at 4 K, approximately the lowest temperature possible to be reached in hydrogen without the aid of laser cooling or a dilution refrigerator, hydrogen's mean velocity is $300\,\mathrm{m\,s^{-1}}$ as shown by the velocity distribution plotted in fig. 1.6. For an atomic beam experiment attempting to measure the 1S-2S transition at room temperature with an intersecting 100 µm spot size laser beam, there would be broadening on the order of 1 MHz strictly due to transit time broadening.

The binding energy of hydrogen's ground state is notoriously deep and poses an even greater difficulty. Hydrogen's ground state energy lies so deep that VUV lasers are required to do Doppler cooling on the atom. These light sources are very difficult to generate and the power can be lost by optics that have 50-80% transmission or reflection losses, and the beam handling must be done in vacuum. Still, in spite of these challenges, some demonstrations of Doppler cooling have been successful. In the early 90's a cold hydrogen sample was successfully Doppler cooled [35]. As is summarized by [36], the demonstration in [35] used a a pulsed Ly-alpha laser with an average power of 160 nW that could deliver 2.5 nW at the location of atoms. This was used to cool magnetically trapped H which had evaporatively been precooled to 80 mK, all within in a dilution refrigerated magnetic trap. At these powers, it took more than 15 min to reach just 8 mK. In this experiment, the two-photon 1S-2S transition was subsequently excited for a spectroscopic determination of the energy difference. Although an improvement of the transition linewidth due the laser cooling was observed, the precision achieved does not beat the best measurement of the 1S-2S transition which was performed in a 5 K effusive atomic beam. In fact, all of the highest resolution spectroscopy measurements to date all have occurred in thermal beams, where no such techniques of laser cooling have been employed. Even without laser cooling, these measurements have reached impressive fractional uncertainties despite the relatively high temperature samples of hydrogen as is displayed in Table 1.1. In a separate line of experiments, motivated by tests of the

fundamental symmetry CPT with Anti-Hydrogen, a few groups have made the effort to continue novel laser development to perform Doppler cooling of hydrogen. In an impressive recent experiment [37], the ALPHA collaboration was able to demonstrate the direct cooling of antihydrogen atoms and a measurement of the 1S-2S lineshape compressed by the cooling. This demonstration is an impressive feat, however, the Doppler cooling rates at even the best available laser powers are quite low, on the order of 240 s per shot.

Significant effort has gone towards addressing the atomic velocity directly in ways other than using Lyman-alpha radiation. For example, some efforts have been made at pulsed field Zeeman and coil-gun deceleration deceleration in a beam [38–40]. In fact, a 12 stage switching magnetic field Zeeman deceleration method has successfully been demonstrated to load a quadrupole magnetic field trap over a decade ago [39]. These feats demonstrate impressive advancement of their respective technologies, however, it is still attractive to explore other possible avenues to reduce the temperature or velocity of hydrogen samples. Some techniques of cooling H using the 243 nm two-photon transition are also proposed by cycling the long lived 2S atoms out of the 2S state with another field [41] and even sub Doppler capable methods using a Sisyphusian scheme in [36]. Another exciting experiment under development is the work at Columbia to trap and cool diatomic hydride molecules such as BaH or CaH to sub Doppler temperatures then use a resonant photodissociation technique to separate the hydrogen atoms from the molecule leaving them left over in a cold trap without experiencing heating [42–44].

An attractive feature of hydrogen is the long-lived 2S state. The 2S level in hydrogen has no where to radiatively decay to without a twp-photon emission (which is largely suppressed through a small matrix element) making the 2S state metastable with a lifetime of 122 ms. This is the reason that the 1S-2S line has such a narrow natural linewidth making it attractive for precision spectroscopy [6, 22, 45]. This feature of the hydrogen spectrum has driven the development of advanced laser sources at the DUV wavelength of 243 nm nonlinear crystals as well as highly reflective optical coatings can be made by commercial suppliers. Efficiently exciting the 1S-2S transition comes with its own technical hurdles in that it requires significant laser powers to drive any

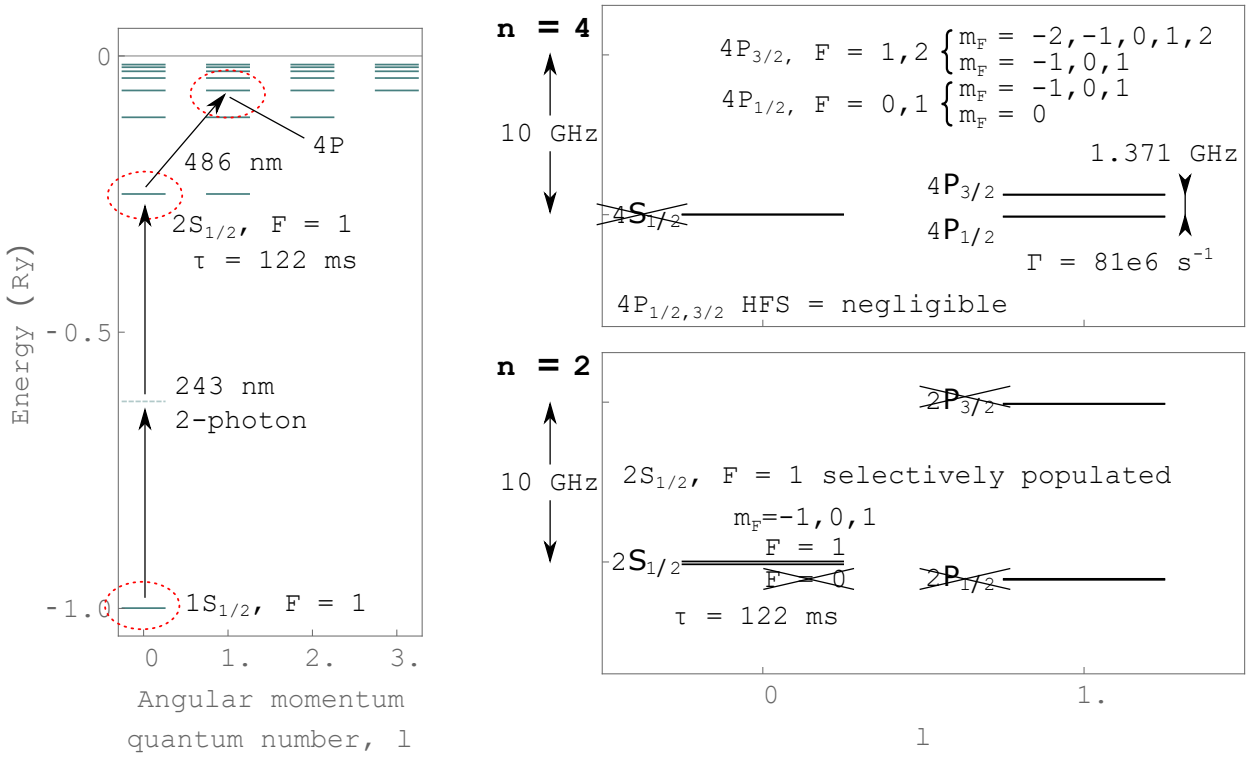

Figure 1.7: Relevant atomic energy levels for this work (drawn to scale). Hydrogen's ground state (1s) lies 1 Ry below the continuum, and the $n = 2$ manifold is reached by 243 nm two photon transitions to the 2s which has a lifetime of 122 ms. Atoms excited to the long lived 2S state can be excited to many of the Balmer allowed transitions in with visible wavelengths, with the longest wavelength at 656 nm, and the second at 486 nm. The 2S hyperfine splitting is resolved with an magnitude of 177 MHz which the laser linewidth is capable of selectively populating. Linear polarization is used allowing all three m_F states to be populated. In the n=4 manifold which lies 486 nm above the n=2, only the P states are considered as they are the only ones dipole allowed to connect to the 2S state. The fine structure splitting is 1.371 GHz, and the hyperfine splitting is assumed to be negligible in this case, however all of the $2S_{1/2}$ and $4P_{1/2,3/2}$ magnetic sublevels are considered (discussed in a later chapter). The 4P state decay rate is $81 \times 10^6\,\mathrm{s}^{-1}$.

appreciable population to the 2S state. With the novel laser system developed in our lab, we have the ability to excite this transition. Once the atom is in the 2S state, many visible dipole-allowed transitions become accessible where laser radiation is significantly easier to generate. Methods like Doppler cooling would not be viable as cycling transitions out of the 2S state would cause spontaneous emission back to the 1S ground state, causing atoms to go dark after a single photon scatter. However, spontaneous emission free techniques such as far detuned optical traps or optical lattices that do not quench the 2S state are possible.

An often employed tool for optically manipulating neutral atoms and molecules is through the use of the Optical Dipole Force (ODF) [46, 47]. The ODF, which we will examine a more detail in chapter 5, is the mechanism underlying far detuned dipole traps (optical tweezers) which have been used in fields as diverse as single-molecule biophysics [48], and quantum computing [49]. A periodic dipole trap, or "optical lattice", is generated when light is retroreflected into a standing wave, allowing molecules or atoms to be stored in a periodic potential whose lattice sites are spaced on the order of an optical wavelength. The periodic dipole trap is regularly used to store atoms in 1D, 2D, and 3D lattices of light for many uses such as optical clocks or quantum computing []. Time dependent lattices have also been employed in atom interferometry to manipulate the motion of matter waves for measurements like the first observation of Bloch oscillations in a periodic potential [50], high precision determinations of α [51], or the gravitational constant, G [52, 53]. Optical lattices have also been used to decelerate the velocity of molecular beams [46]. It is interesting to apply similar techniques as is accomplished in atom interferometry experiments and molecular beam deceleration to an atomic hydrogen beam.

The demonstration of optical deceleration of hydrogen completed in this dissertation was achieved by trapping metastable 2S atoms moving in an atomic beam within a comoving optical lattice and decelerating the atomic motion through deceleration of the optical lattice. The motion of the optical lattice is straightforward to control with off-the-shelf electro-optics and RF electronics. Once the atoms are decelerated, new opportunities exist for precision measurement as well as the potential for loading magnetic and optical traps. This method then follows the outline in fig. 1.8. Atoms are first excited from an atomic beam into the 2S state where they will live for a relatively long time. To manipulate the motion of these 2S atoms, we generate an optical lattice detuned from the 2S-4P transition of the atom at 486 nm. Because we do not want to quench the the 2S atoms with spontaneous emission, large detunings are necessary. Since the trap depth of an optical lattice depends inversely on the laser detuning from resonance, we must make a high power laser at 486 nm to compensate for the laser detuning while still having deep enough traps to capture measurable quantities of atoms to be manipulated and decelerated.

Figure 1.8 contains the three main steps that we had to complete for the demonstration of the experiment proposed above. First, we needed to generate a beam of atomic hydrogen and build an effusive atom beam-line apparatus. This is discussed in Section 2.2 and is published in [12]. It was also useful in [12] to characterize the ground state and metastable atomic beams for the velocity distribution so that atomic trajectory dependence in the AC stark shift could be accurately quantified in the precision measurement completed in [8]. The second step, which was accomplished concurrently with the first, was to build a laser source to excite the 1S-2S two-photon transition and characterize the metastable atomic beam which is published in [54] and discussed in Section 3. We then could finally design, build and perform the deceleration experiment which included construction of a high power 486 nm light source and optical lattice control electronics and electro-optics discussed in chapter 5.

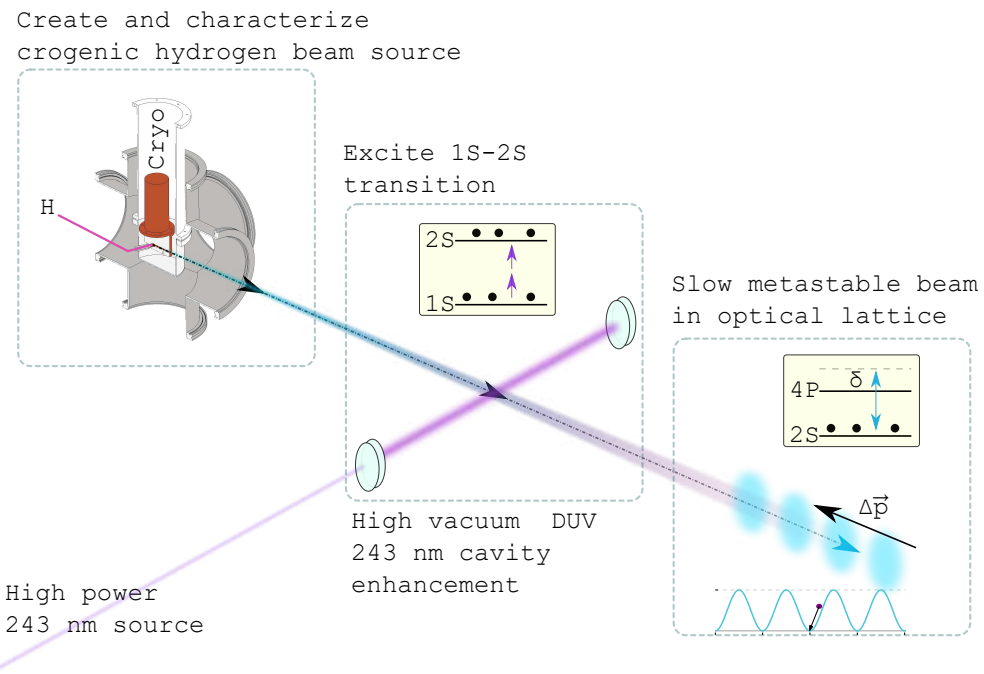

Figure 1.8: Outline of experiment for this work. A cryogenic atomic beam with velocity characterization was first constructed, alongside a high power 243 nm resonant enhancement cavity to efficiently excite the 1s-2s transition and generate a cryogenic metastable hydrogen beam with velocity characterization. A laser system for the 486 nm optical lattice was also constructed and used to demonstrate an all optical method of decelerating metastable atomic hydrogen with a time varying optical lattice.

Chapter 2

Atomic beam generation

The highest resolution hydrogen spectroscopy has been achieved with cold effusive atomic beams (4-6 K). As the molecular/atomic beam method has been around since the time of Nobel Prize winners Stern, Rabi, and Kusch [55–57] there has been much development over the years. Ovens and other types of sources are used in many species, however for hydrogen two types of beam source dominate the field which are pulsed supersonic expansion [14, 58, 59], and thermally effusive beams. Typically for hydrogen spectroscopy the choice of thermally effusive beams are chosen since they can be used to make cryogenic temperature beams that are low density (non-interacting) with high continuous flux and are also compatible with standard microwave discharge sources of atomic hydrogen. There are a limited examples of pulsed supersonic expansion style atomic beams used in hydrogen research, however recent progress has made this method of atomic beam generation relatively attractive. Supersonic expansion beams rely on pulsed operation of a solenoid valve and therefore have limited duty cycles, however they have a distinct advantage that their radial as well as axial temperatures are quite low (narrow velocity distributions). In a recent example demonstrated in the Merkt group in France, [14], the axial (beam-direction) temperature of the atoms was as low as 15 mK, or spread over a velocity range of 30 m/s, centered at a velocity near 1200 m/s. A beam source with this performance would in fact couple extremely well with the velocity slowing performed in this work, therefore the experiments in this thesis are potentially exciting to extend to pulsed atomic beam sources. Other than this case, effusive beams serve as the workhorse for hydrogen measurements. Significant amount of groundwork has been laid prior to this dissertation in the design of atomic beams of hydrogen [11]. Much of the design considerations center around only a few aspects which are: delivery of atomic hydrogen to a cryo-cooler nozzle without significant recombination losses; thermal shielding for the cryogenic system; beam formation of an effusive low-density beam in the molecular flow regime (to limit in-beam interactions); collimation; and beam characterization such as the velocity profile using a direct

mechanical beam chopper. An overview of our atomic beam formation apparatus is shown in Fig. 2.1.

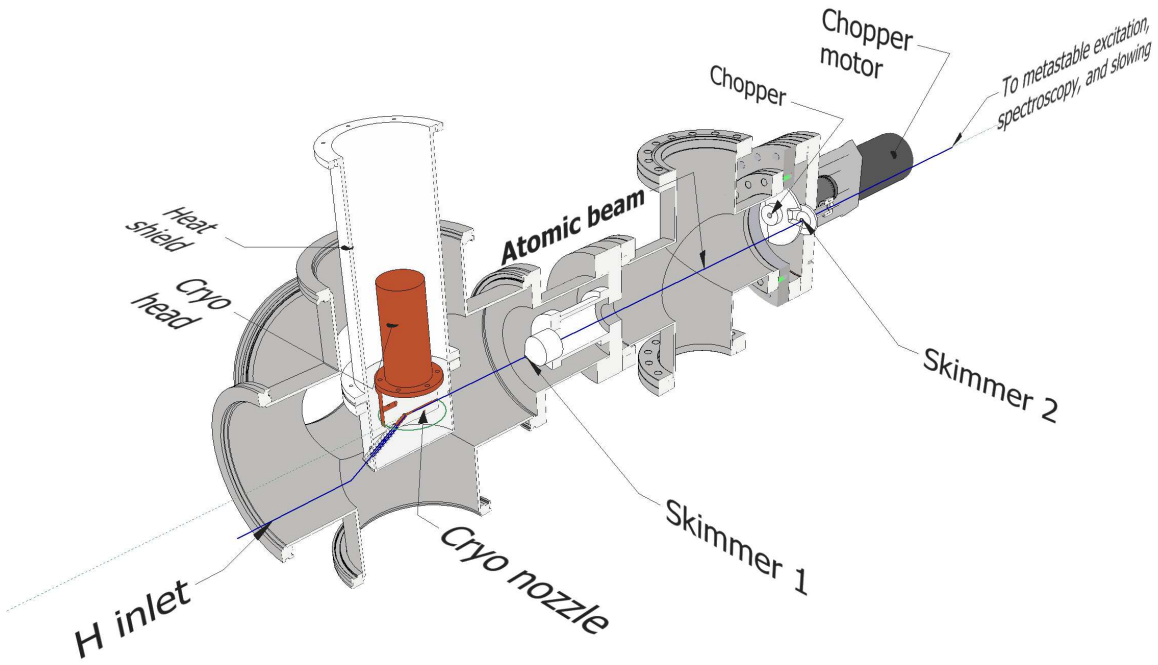

Figure 2.1: Partial section view of the first two stages of the atomic beam apparatus designed and built in this work. Dissociated atomic hydrogen is transported from the microwave discharge by a Teflon tube to the cryogenic nozzle in the first chamber. Atoms are cooled through collisions with a metallic nozzle cooled by a closed cycle Gifford-McMahon cryostat and the atomic beam is defined by the nozzle cylinder aspect ratio and two subsequent skimmers. Generation of atomic hydrogen from a molecular source is described in Section 2.1. The vacuum chamber and cryogenic design is discussed in Section 2.2, and a study of nozzle geometry selection in Section 4.2. The atomic beam profile is discussed in Section 2.2 and detection of atomic hydrogen is discussed in Section 2.3. The second differentially pumped chamber has a DC motor driven chopper installed for velocity studies as discussed in Chapter 4.

This chapter describes the work done to generate the ground state and metastable atomic beams and their respective velocity characterizations [12, 54]. As is seen in Fig. 2.1 the formation of the cryogenic atomic beam is made by flowing atomic hydrogen through a nozzle which will cool the atoms before letting them freely effuse into a vacuum chamber. Afterwards, the transverse profile of the beam is formed by two metallic skimmers. Since gaseous hydrogen is a diatomic molecule, the atoms must first be separated by breaking the molecular bond. We perform the

dissociation to atomic hydrogen in a microwave discharge common to low temperature plasmas [60] (Section 2.1). There are some material considerations to keep in mind when dealing with atomic hydrogen which is discussed throughout this chapter with emphasis on limiting surface recombination ($2H \longrightarrow H_2 + \Delta E$). After formation, the beam is sent to downstream chambers for spectroscopy, slowing, and detection. The hydrogen detection methods are also covered in this chapter (Section 2.3) as well as some atomic beam profile and flux calibrations (Section 2.2) and the work surrounding the 1S-2S two-photon excitation to generate the metastable 2S hydrogen beam (Section 3) in [54]. Finally, at the end of the chapter is the work on the velocity characterization used to briefly study atomic beam nozzles (Section 4.2).

2.1 Microwave discharge

The atomic hydrogen is first dissociated from molecular hydrogen in a microwave discharge operating at 2.45 GHz. A schematic of the gas foreline and dissociator system is shown in Fig. 2.2a. The microwave cavity (Opthos Instruments) is based on the Evenson design from [60], and the microwave source is a voltage-controlled oscillator (Mini-Circuits ZX95-2390A-S+) amplified by a 100 W power amplifier (Mini-Circuits ZHL-100W-242+) with ≈40 W typically used to sustain the discharge. The discharge is contained within an air cooled quartz tube with a 500 micron conductance limiting aperture. The low pressure side of the aperture is connected directly to a Teflon tube that delivers the atomic hydrogen to a cryogenic nozzle (section 2.2). For reference, a circuit diagram for the hydrogen dissociator microwave power supply with mini-circuits parts numbers is show in Fig. 2.2b.

It is useful to estimate the atomic flux and density to make signal to noise ratio (SNR) estimates. Gas flow calculations follow from the work shown in Appendix A. As shown in Fig. 2.2a, molecular hydrogen is transported to the microwave discharge through a series of tubes where the pressure is stabilized with a pressure feedback mass flow controller (Alicat). On this inlet gas line is a flow calibration volume which has a significantly larger containment volume (0.36 L) than the rest of the delivery lines which is used to determine the molecular throughput of the inlet system. A

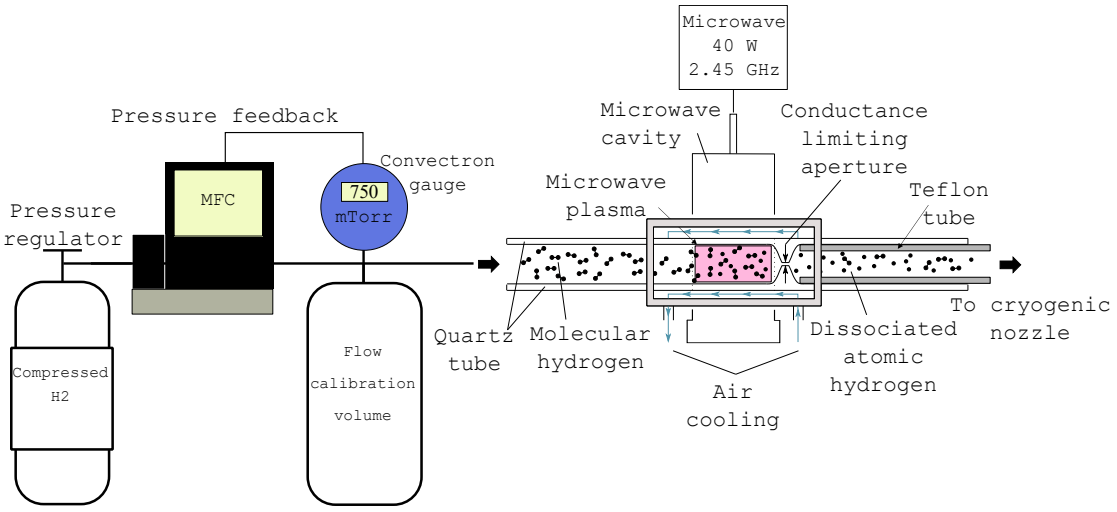

(a) Hydrogen Delivery

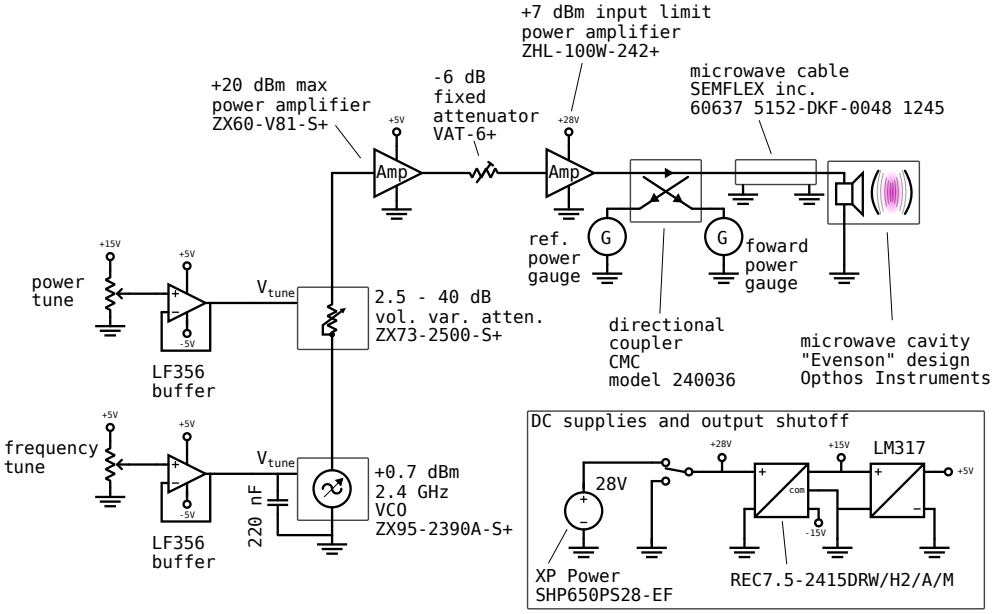

(b) Micrwave circuit

Figure 2.2: (a) Diagram of the hydrogen inlet gas flow and microwave plasma discharge subsystem. Molecular hydrogen from a compressed gas cylinder flows to the plasma discharge region and is metered by a mass flow controller (MFC, Alicat) with pressure feedback. Pressure stabilized control translates to flow control by way of the conductance limiting aperture with vacuum held on the outlet. The flow rate is measured by pumpout time of the calibration volume. Atomic hydrogen is generated in an aircooled microwave cavity. Atomic hydrogen effusives through the orifice into a teflon tube and transports the gas to the cryogenic nozzle. The orifice and plasma discharge are contained in a custom blown quartz glass tube. (b) Hydrogen discharge microwave circuit. Part numbers included. RF Frequency is tuned with a VCO, typically set to 0.664V to operate at 2.45 GHz. Forward power is controlled with a voltage controlled variable attenuator before amplification and typically run for output powers of 40 W.

plot of this data collected for the calibration volume of 0.36 L and a conductance limiting aperture with a diameter of ≈ 0.5 mm is plotted in Fig. 2.3.

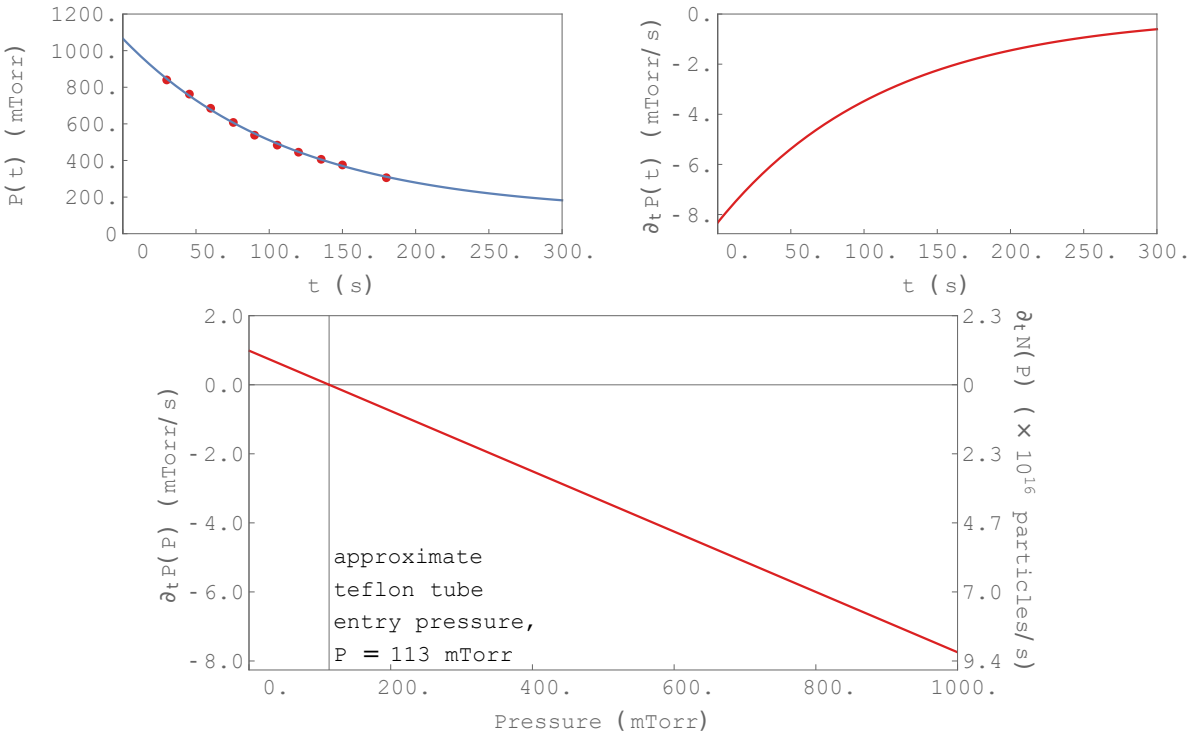

Figure 2.3: Pumpout measurement data and exponential fit of a single initial gas load for throughput calibration. Temperature assumed to be 300 K and the calibration volume had a $V = 0.36$ L and the particle flux is approximately 7×10^{16} particles per second.

The optimal operating pressure for generating atomic hydrogen was empirically found to be between 700 and 800 mTorr. Higher discharge pressures increased the flux but also produced a noticeable increase in the heat load on our cold nozzle. At pressures above 1.2 Torr, the H_1 beam flux dropped, which we believe is due to recombination in the discharge region. As seen in Fig. 2.3, we estimate that the atomic flux is $\approx 7 \times 10^{16}$ particles/s through the hydrogen discharge in this operation range. Because of the continuity of the gas flow at the teflon tube (gas in equals gas out), this is also the total flux out the nozzle in particles per second. A rough measurement of the dissociation fraction of the hydrogen beam was made by comparing the 1 amu to 2 amu ion currents in a quadrupole mass spectrometer (QMS) residual gas analyzer (RGA) with the discharge

on versus being shut off the atomic beam composition was found to be on the order of 50% atomic hydrogen. This forms the upper limit of the atomic hydrogen throughput in our system. All of the estimates here assume a constant room temperature flow of hydrogen through the transport tubes, but this obviously breaks down when the nozzle is cryogenic (<5 K). Below the freezing point of H_2, $T \approx 14$ K, the throughput out of the nozzle will be less than at the discharge conductance limiting aperture. Although we have not specifically studied the formation of hydrogen ice in our system, we have observed that this effect varies with the nozzle temperature. Above 14 K we observe a flux consistent with these estimates, but in the range of 6–14 K there is a significant loss of hydrogen atoms. However, below 6 K we see a near full recovery of the atomic hydrogen signal. This recovery may be due to the presence of a complicated ratio of atomic and molecular hydrogen phases, as well as recombination induced thermal energy supporting a steady state of ice sublimation. One hypothesis is that a small fraction of helium leaked into the discharge could improve both the nozzle at cryogenic temperatures, and discharge characteristics. Optimization of the cold temperature throughput in this way remains to be studied.

2.2 Vacuum and cryogenic apparatus design

2.2.1 Atomic beam profile

The atomic beam divergence profile is formed by the nozzle and two skimmers as shown in Fig. 2.4. As is discussed in appendix A, a gas flowing down a tube will adsorb and desorb from the walls following a cosine law [61]. This causes two things to occur for a gas with a source located on one end of a tube, and vacuum on the other. For any collision with the wall, there is a chance that the particle will reemit back toward the source direction, meaning that the probability to transmit out the vacuum end of the tube to be reduced. This causes a tube to act as a restriction to the gas flow, lowering the conductance of the tube to below that of a simple orifice. The second effect in a straight tube is that some atoms have a probability of sticking to a wall, the reemitting down tube nearly parallel with the walls to transmit with a low angle with respect to the tube axis, i.e. causing the tube to have a forward peaked emission pattern. Since the cryogenic nozzle is essentially just a

narrow tube, this means the atomic nozzle forms a forward peaked beam of atoms in the molecular flow regime, as depicted by the blue arrows in Fig. 2.4 [62–66]. The maximum atomic beam divergence angle is approximately 0.5° limited by the two skimmers which are separated as shown in Fig. 2.4. For a higher precision determination of the gas flow pattern from a nozzle, a Monte Carlo (MC) ray tracing simulation would be necessary (see for example the methods in [**?**]).

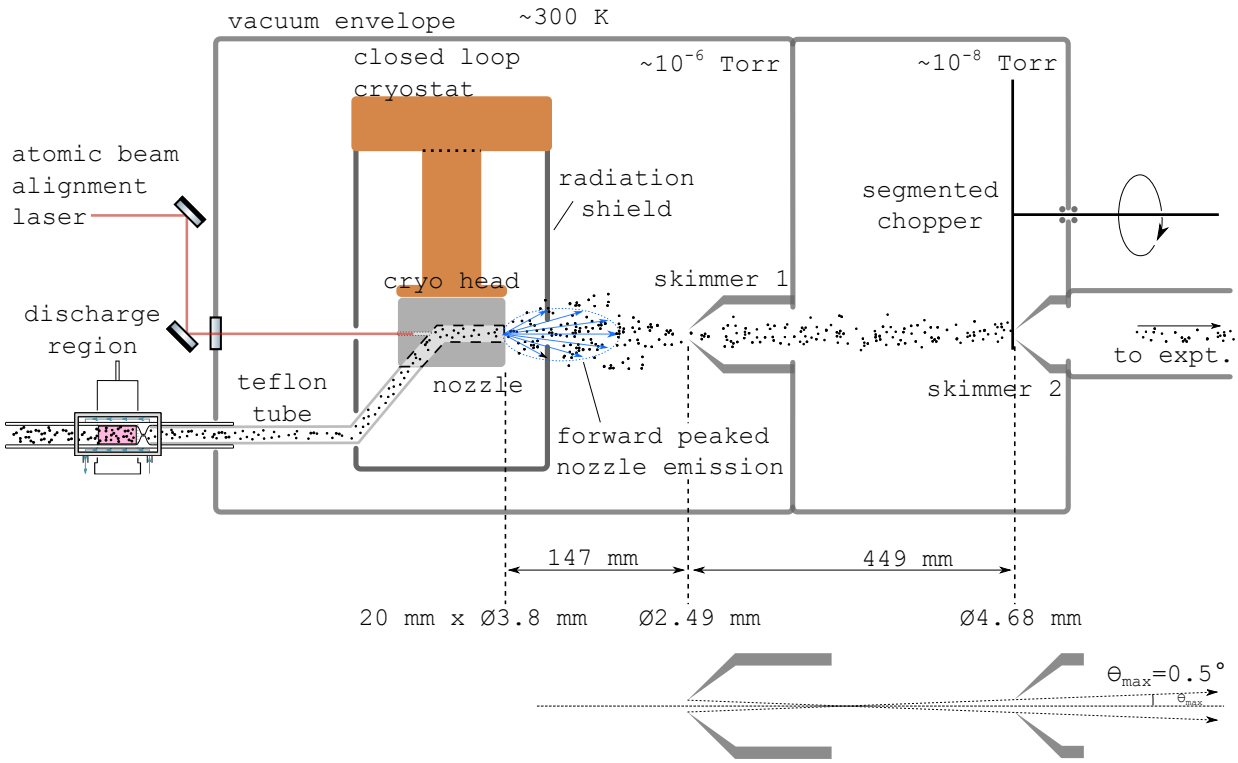

Figure 2.4: Atomic beam formation apparatus diagram. A Teflon tube which reduces hydrogen recombination losses transports H atoms from discharge to cryogenic nozzle. The cryogenic nozzle is mounted to the cold head of a two stage closed loop cryostat, and enclosed within an cryogenic heat/radiation shield. The beam divergence is formed by the nozzle and two skimmers whose dimensions and separations are indicated in the figure. A chopper interrupts the beam before the second skimmer for time of flight and other atomic beam modulation needs. The atomic beam can be aligned to the laser spectroscopy and slowing apparatus by shining a collimated laser through a window in the vacuum chamber and an opening on the nozzle, or through an alignment jig, machined separate of the nozzle.

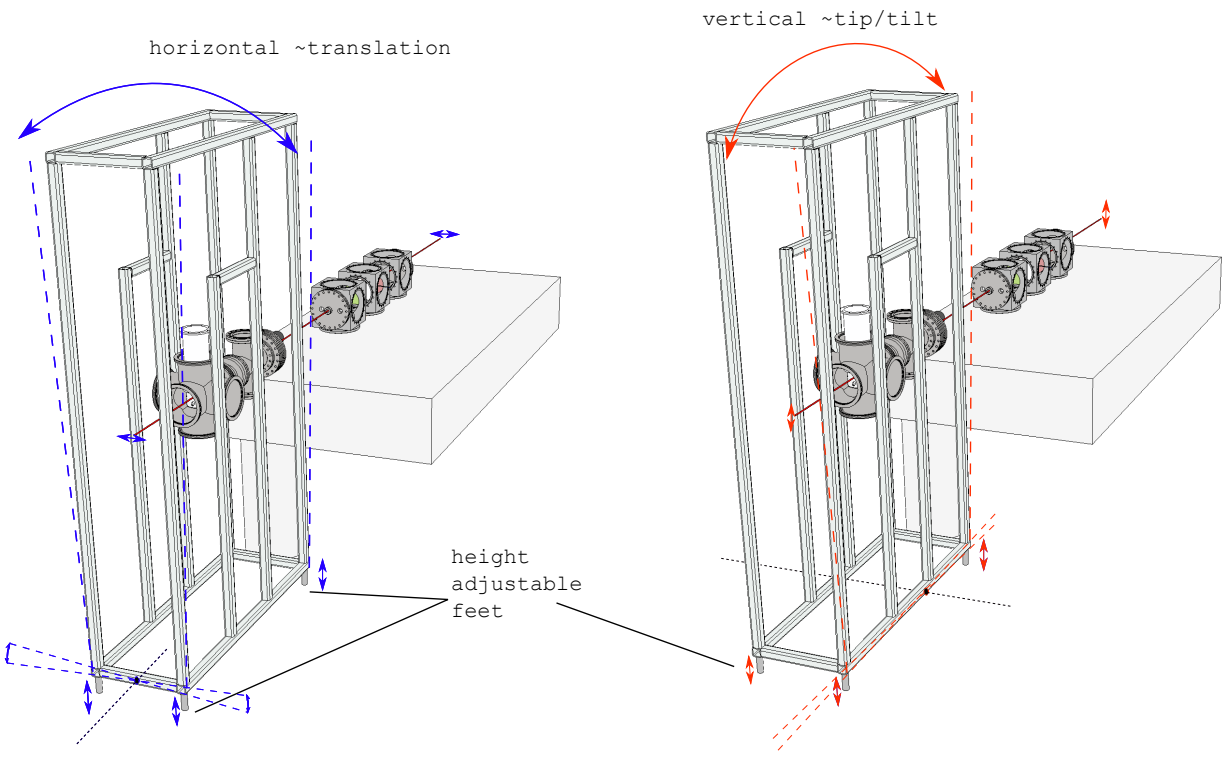

Figure 2.5: Diagram of fine/rough adjustment of atomic beam alignment for initial setup or optimization. An alignment laser is set up on a breadboard attached at the nearest flange of the vacuum chamber. Blue shows the method for adjusting the atomic beam horizontally with respect to the spectroscopy chamber and optical table, red shows vertical tip and tilt. The dotted black line at the base shows the pivot axis when feet on opposite sides of the pivot are adjusted in opposite directions. The height adjustable feet are screwed into and out of the 80-20 frame and are locked into place with an interference nut.

2.2.2 Atomic beam alignment

Some alignment freedom is present in the structure of the atomic beam apparatus which was used to do the initial leveling with respect to the lab frame, as well as an in situ fine tuned adjustments for spectroscopy. Atomic beam alignment uses a reference laser which is aligned either through a nozzle with a hole drilled axially with the nozzle beam, or using a temporary alignment jig and the two atomic beam skimmers. The apparatus is then moved by adjusting the beam stand's feet so that the laser beam passes through the same height stick at a near and far location. Figure 2.5 shows the alignment jig and structure which the atomic beam apparatus is mounted on where the adjustable feet to the vacuum stand are used to tip and tilt the angle of the hydrogen beam with respect to the lab frame and optical tables. The atomic beam is currently aligned to be level and

6" above the optical table which supports the rest of the vacuum chambers. Once set, only minor adjustments need to be made to the atomic beam angle to optimize spectroscopy signals. The spectroscopy and slowing apparatus can then be assembled based on a secondary reference laser aligned back through irises attached to the optical table top which are coaxial with the primary atomic beam alignment laser.

2.2.3 Heat shield

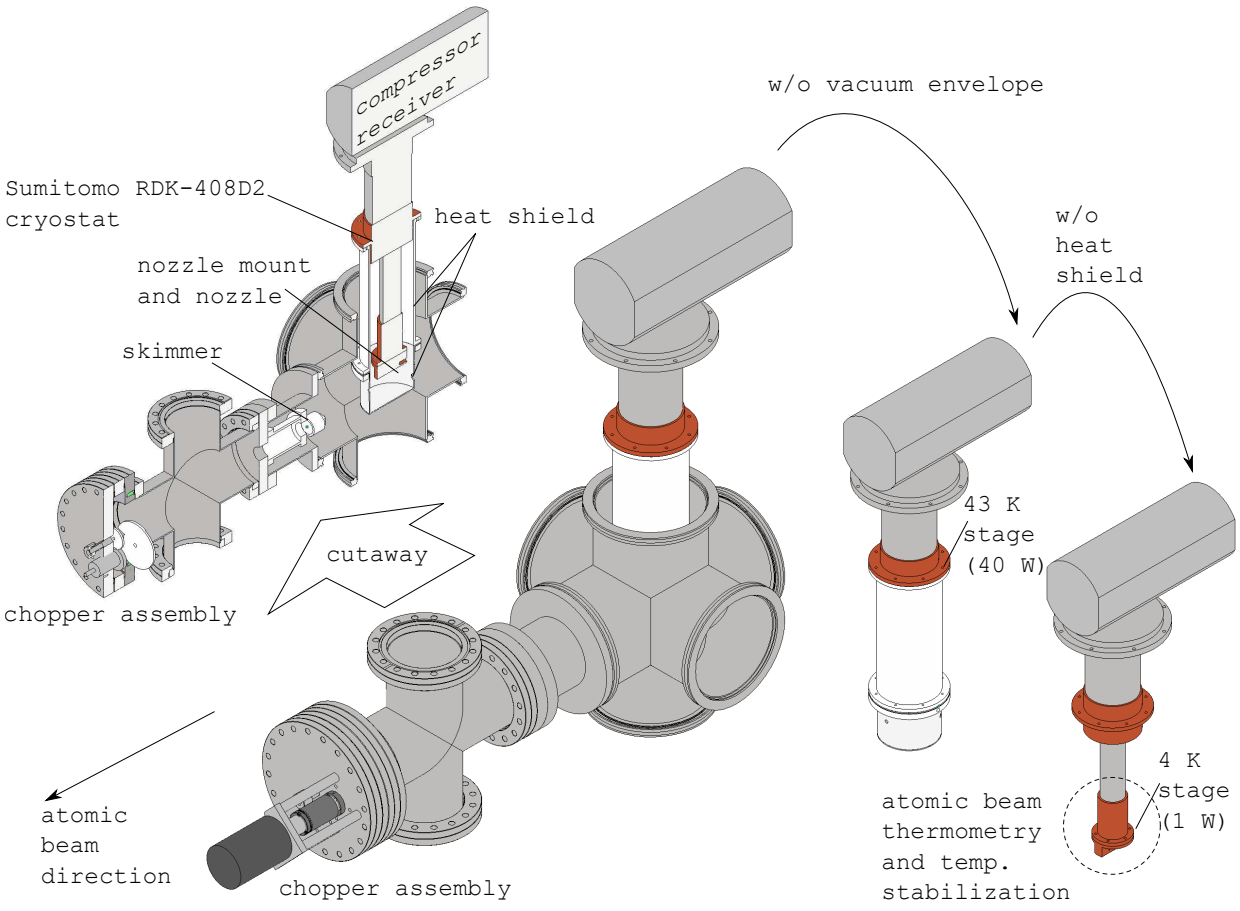

Figure 2.6: The atomic beam vacuum apparatus and it's internal components related to the cryogenic cooling separated. The heat shield is made of 1100 aluminum. Dimensioned drawings are these parts are included in the appendices.

The cryogenic chamber and atomic beam apparatus is housed inside of CF and ISO type vacuum chambers, as depicted in Fig. 2.6. The cryogenic nozzle chamber has a constant flow of

hydrogen leaking into it under vacuum so it does not require as high of a vacuum, allowing us to use the large viton O-ring style ISO160 6-way cross. The cryostat we use is a Sumitomo RDK-408D2, with a F-70L helium compressor, which is mounted to the 6-way cross with custom flanges (see appendices for engineering drawings.) As shown in Fig. 2.6, the central 4 K stage is contained within a 43 K radiation shield which is attached to the first stage of the cryostat and has a cooling power of roughly 40 W. Since the cryostat will be contained in vacuum, convective and conductive thermal loads on the cryostat are negligible, leaving radiation as the primary heat load. Without a cryogenic radiation shield, the nozzle would be subjected to black body radiation (BBR) from the entire internal surface area of the 300 K stainless steel vacuum chamber.

Since the utility and performance of the atomic beam is closely connected to the nozzle temperature it is imperative to keep it as cold as possible. Since the rate at which heat flows is proportional to the temperature difference between two bodies, an item kept at 4 K will very rapidly heat if connected to the environment at roughly 300 K. The first major step to reducing heat transmitted to the nozzle is by placing it in vacuum and connecting it directly to a conductive refrigeration source. In vacuum there is negligible convective heat flow between objects, and if two bodies are disconnected physically, that leaves radiation as the only source of heat to the cryogenic nozzle. By itself, radiation can cause a significant heat load since the power emitted by a surface scales with temperature as T^4.

Black body radiation (BBR) is described by Planck's law [**?**] *

$$B_\lambda \, \mathrm{d}\lambda = \frac{2hc^2}{\lambda^5 \left(e^{\frac{hc}{k_B \lambda T}} - 1 \right)} \mathrm{d}\lambda, \tag{2.1}$$

which describes the irradiance per unit solid angle as a function of wavelength for a differential element of black body surface. Plotted in Fig. 2.7 is the spectral distribution of BBR as a function of wavelength for a few temperatures.

*see [**?**] for fun on Planck's treatment solved the ultraviolet catastrophe by introducing quantization, and [**?**, **?**] for statistical mechanical treatments of the Black Body radiation energy distribution.

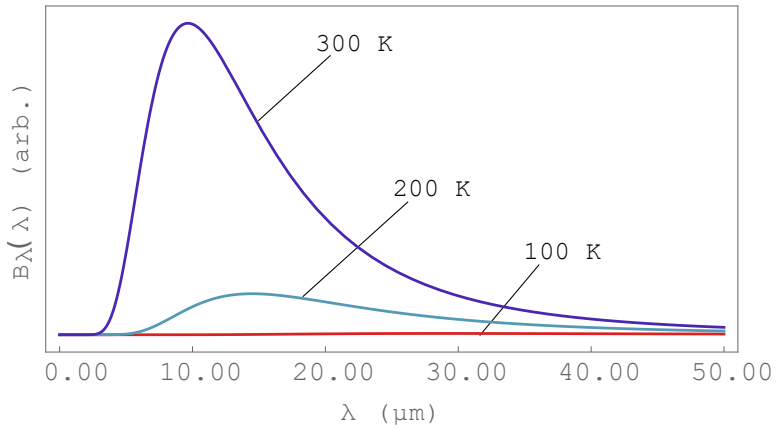

Figure 2.7: B_λ plotted over wavelength in arbitrary units. As can be seen, the integral of the distribution reduces significantly for decreased temperature as its peak moves towards longer wavlengths.

To determine the total radiated power from a differential area element, $Q = \mathrm{d}P/\mathrm{d}A$ as a function of temperature, we can integrate Eq. 2.1 over a hemisphere of solid angle and over the entire radiation spectrum.

$$Q_{BB}(T) = \int_0^{2\pi} \mathrm{d}\phi \int_0^{\frac{\pi}{2}} \sin(\theta)\cos(\theta)\,\mathrm{d}\theta \left(\int_0^{\infty} \frac{2c^2 h}{\lambda^5 \left(e^{\frac{ch}{\lambda k_B T}} - 1 \right)} \mathrm{d}\lambda \right)$$

which yields the Stefan Boltzmann law of total radiated power for an ideal black body emitter

$$Q_{BB}(T) = \sigma T^4, \tag{2.2}$$

where

$$\sigma = \frac{2\pi^5 k_B^4}{15c^2h^3} \approx 5.67 \times 10^{-8}\,\mathrm{W/m^2/K^4}.$$

This is the law of thermal radiation emission for a perfect black body emitter in thermal equilibrium. No material is a perfect black body emitter due to surface reflection and transmission effects, and therefore the ratio of the true surface absorption/emission to the ideal black body, ε is the emissivity of the surface, giving

$$Q(T) = \varepsilon \sigma T^4, \tag{2.3}$$

for an imperfect black body. Integrating this equation over the surface area of a body, assuming a uniform surface composition, gives the total thermal energy radiated per unit time from an object

$$P = \oint_A Q \, \mathrm{d}A = A\varepsilon\sigma T^4. \tag{2.4}$$

Plotted in Fig. 2.8 typical stainless steel vacuum chamber ($\varepsilon \approx 0.5$ with a surface area of $0.5\,\mathrm{m}^2$ will be radiating inward with a power of roughly 100 W, whereas at 40 K would instead only radiate 36 mW. Therefore, is imperative to separate the cold head from a hot environment since the cryostat has limited cooling power at 4 K (on the order of 1 W) whereas at 40 K and 80 K it can extract 40 and 200 watts respectively.

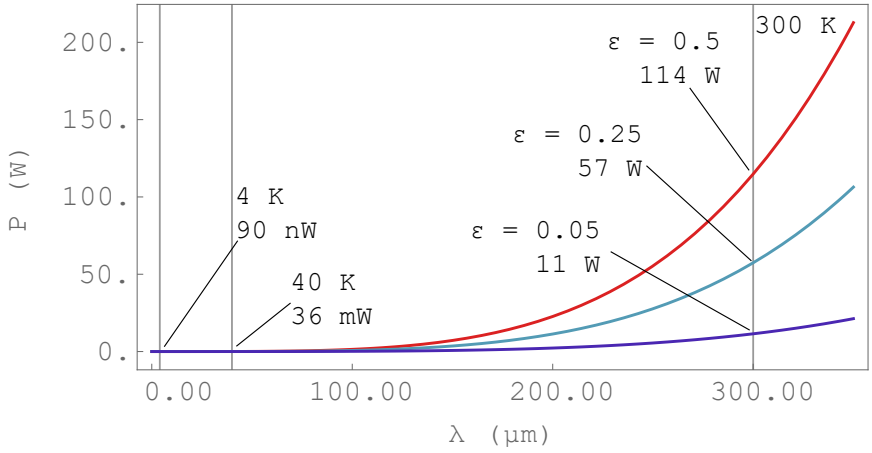

Figure 2.8: The Stefan-Boltzmann Law plotted for approximately $0.5\,\mathrm{m}^2$ of stainless steel. For imperfect black body emitters, such as reflective surfaces like polished Aluminum or Copper, the power radiated at thermal equilibrium is greatly reduced as shown by the three emissivity curves and the power radiated at 300 K.

The internal energy of an object, j, will change with respect to time as

$$\frac{\mathrm{d}U_j}{\mathrm{d}t} = -P^{(emitted)} + \sum_i P_i^{(absorbed)}, \tag{2.5}$$

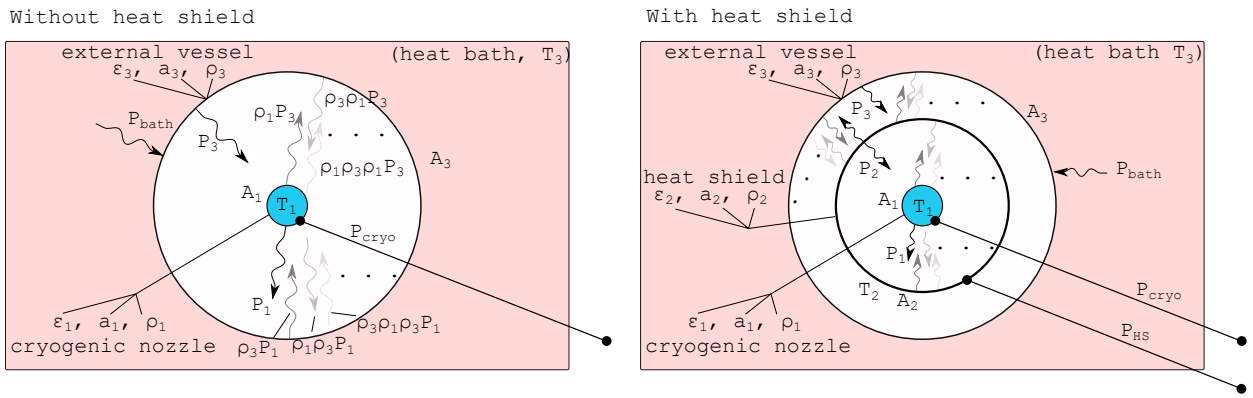

Figure 2.9: Two heat radiative heat load diagrams. The first is without a heat shield, the second includes a refrigerated radiation shield. The powers that are absorbed by each object takes the incident radiation power multiplied by the absorption coefficient, $a_i = \varepsilon_i$, and each reflection is the incident radiation multiplied by the reflection coefficient, $\rho_i = 1 - a_i = 1 - \varepsilon_i$, as is described in the text.

where all of the sources of absorbing radiation are added up in the $P^{(absorbed)}$ term, including the refrigerator, re-reflected radiation, etc. Figure 2.9 shows a diagram of this physical model with all of the sources of absorbed radiation included.

In general it is difficult to calculate the heat flow between two objects due to the surface to surface view factors which depend on the object geometries [68, 69]. However, in the case of the lowest order heat shielding calculations, a few simplifying assumptions can be made. First, in the case of a heat shield placed completely within another body, the problem can be modeled accurately assuming that all of the heat not supplied by the refrigeration and thermal reservoir is exchanged completely between the containing vessel and the internal vessels. Second, the angular dependence of the surface emission and reflectance is assumed to be perfectly "Lambertian" which means that it is a perfect diffuser for light and emits/reflects with equal intensities in all directions. Second, all of the black body emitters can be assumed to be perfectly opaque grey bodies so transmitted powers are zero, and will have emissivities $\varepsilon_i < 1$, that are spectrally and angularly independent. Next, the grey bodies are forced to be in thermal equilibrium so that their temperatures are isothermal. A consequence of thermal equilibrium is the Helmholtz-Stokes reciprocity in means the bodies are equal emitters as they are absorbers of radiation will have absorption coefficients, $a_i = \varepsilon_i$. Since the transmission of the bodies is zero, they will have reflection coefficients,

ρ_i, such that $\rho_i + \varepsilon_i = 1$. Lastly, the view factors, $F_{i\to j}$, between the surfaces that are exposed to each other can be assumed to be 1, which leads to an upper limit on the amount of shielding necessary to isolate a cold region. In reality, only a perfectly convex surface contained completely within a larger surface can be equal to one. In the case depicted in Fig. 2.9, the outer surface can emit radiation back at itself which would modify/reduce the amount of cooling necessary to hold the nozzle at a low temperature. The case of a set of concentric cylinders is considered at the end of this section.

For the example without a heat shield in Fig. 2.9, the power emitted from the containing vessel, P_3, is absorbed by the central body (i.e. nozzle) with a coefficient of absorption, a_1, plus all of the repeated diminishing reflections, $(\rho_3\rho_1)^i$, giving a term $a_1P_3(1+\rho_3\rho_1+(\rho_3\rho_1)^2+\dots)$. Additionally, the small amount of radiation that the nozzle emits into the vacuum, P_1, can reflect back at itself off of the containing vessel and bounce back and forth, creating a term $a_1\rho_3P_1(1+\rho_3\rho_1+(\rho_3\rho_1)^2+\dots)$. Adding all of this up for the nozzle, equation 2.5 becomes

$$\frac{\mathrm{d}U_1}{\mathrm{d}t} = P_{cryo} + a_1P_3(1+\rho_3\rho_1+(\rho_3\rho_1)^2+\dots) + a_1\rho_3P_1(1+\rho_3\rho_1+(\rho_3\rho_1)^2+\dots) - P_1,$$

$$\frac{\mathrm{d}U_1}{\mathrm{d}t} = P_{cryo} + a_1P_3\sum_{i=0}^{\infty}(\rho_3\rho_1)^i + a_1\rho_3P_1\sum_{i=0}^{\infty}(\rho_3\rho_1)^i - P_1,$$

which reduces to

$$\frac{\mathrm{d}U_1}{\mathrm{d}t} = P_{cryo} + a_1P_3\frac{1}{1-\rho_3\rho_1} + a_1\rho_3P_1\frac{1}{1-\rho_3\rho_1} - P_1, \tag{2.6}$$

where P_{cryo} is the power necessary to keep the temperature of the cryohead stable. Following the same logic, the outer body is

$$\frac{\mathrm{d}U_3}{\mathrm{d}t} = P_{bath} + a_3P_1\frac{1}{1-\rho_3\rho_1} + a_3\rho_1P_3\frac{1}{1-\rho_3\rho_1} - P_3. \tag{2.7}$$

where P_{bath} is the rate at which the energy flows from the environment into the vessel, and P_3 is the rate at which energy is emitted as BBR from the vessel from its internal surface. Because the system would be at thermal equilibrium, the internal energy of both bodies will not be changing in

time, so $\frac{dU_1}{dt} = \frac{dU_3}{dt} = 0$ making

$$\begin{aligned} P_{cryo} &= P_1 - \frac{a_1 P_3}{1-\rho_3\rho_1} - \frac{a_1\rho_3 P_1}{1-\rho_3\rho_1}, \\ P_{bath} &= P_3 - \frac{a_3 P_1}{1-\rho_3\rho_1} - \frac{a_3\rho_1 P_3}{1-\rho_3\rho_1}. \end{aligned} \tag{2.8}$$

The radiation shield is made of 1100 alloy aluminum since at cryogenic temperatures it performs similar in heat conductivity and emissivity, $\varepsilon_{Al} = 0.05$ (polished), as copper, $\varepsilon_{Cu} = 0.05$ (polished)[†]For emissivities and areas $\varepsilon_1 = 0.05$, $\varepsilon_3 = 0.5$, $A_1 = 0.125\,\mathrm{m}^2$, $A_3 = 0.5\,\mathrm{m}^2$ at temperatures $T_1 = 4\,\mathrm{K}$ and $T_3 = 300\,\mathrm{K}$, we get

$$\begin{aligned} P_{cryo} &= -10.93\,\mathrm{W}, \\ P_{bath} &= -P_{cryo} = 10.93\,\mathrm{W}. \end{aligned}$$

Lucky for us, the 10.93 W of cooling that happens to the cryohead, provides an additional source of air condition for the lab as the heat reservoir (our lab) must supply this energy to stay in thermal equilibrium.

The analysis is the same with a heat shield in place, except that one must account for the heat exchange between the heat shield and the outer vessel, the exchange between the nozzle and the shield, as well as the dual surfaces that are emitting radiation. This becomes

$$\begin{aligned} P_{cryo} &= P_1 - \frac{a_1 P_2}{1-\rho_2\rho_1} - \frac{a_1\rho_2 P_1}{1-\rho_2\rho_1}, \\ P_{HS} &= 2P_2 - \frac{a_2 P_1}{1-\rho_2\rho_1} - \frac{a_2\rho_1 P_2}{1-\rho_2\rho_1} - \frac{a_2 P_3}{1-\rho_2\rho_3} - \frac{a_2\rho_3 P_2}{1-\rho_2\rho_3}, \\ P_{bath} &= P_3 - \frac{a_3 P_2}{1-\rho_2\rho_3} - \frac{a_3\rho_2 P_3}{1-\rho_2\rho_3}. \end{aligned} \tag{2.9}$$

where we have again made all of the same assumptions as earlier. With the intermediate heat shield having emissivity of $\varepsilon_2 = 0.05$, $A_2 = 0.25\,\mathrm{m}^2$, and $T_2 = 40\,\mathrm{K}$, we get that

[†]Total emissivity values taken from engineeringtoolbox.com (accessed 2022/07/21). Emissivity is spectral dependent, and highly surface dependent, however for ballpark estimations I've made the greybody assumption, where emissivity is spectrally flat.

$$P_{cryo} = -930\,\mu\mathrm{W},$$
$$P_{HS} = -10.933\,06\,\mathrm{W},$$
$$P_{bath} = -(P_{cryo} + P_{HS}) = 10.933\,99\,\mathrm{W}.$$

Therefore, by adding a single shield in to block the immediate radiation from the room temperature apparatus causes a significant reduction in the cooling power necessary to run the cryostat at 4 K. As shown with this example, nearly all of the thermal radiation is pumped out by the heat shield which has significantly greater cooling capacity than the cryo head (40 W as opposed to 1 W).

To account for the presence of holes in the heat shield which the inner components have visibility to see, one could just add terms of the form, $P_i^{(hole)} = A_i \varepsilon_i \sigma T_i^4$, to each of the lines in Eq. 2.9.

As mentioned earlier, the view factor consideration was assumed to be unity between the heat shield, nozzle, and chamber. However, if including that the chamber actually may radiate at itself, along with the heat shield, the estimates change slightly. This portion of the work is only included here for completeness, but is insignificant in the design constraints used for the practical heat shielding of the nozzle.

Including the the energy exchange between the radiation shield, vessel, and cryo region we must use the angular view factors, $F_{i\to j}$ (where the subscripts indicate which object is emitting and receiving the radiation and two reversed view factors $F_{i\to j}$ and $F_{j\to i}$ are related by the reciprocity $A_i F_{i\to j} = A_j F_{j\to i}$ [69]). We assume that these objects are all perfectly concentric cylinders with areas A_1, A_2 and A_3, and radii r_1, r_2 and r_3 for the cryo, heat shield and containing vessel respectively. Concentric cylinder view factors are solved in [69], and the simplification of the geometry leads to the view factors reducing to the ratio of the radii,

$$F_{1\to 2} = F_{12} = 1,$$
$$F_{2\to 1} = F_{21} = r_1/r_2,$$
$$F_{2\to 2} = F_{22} = 1 - r_1/r_2,$$

where $r_1 < r_2$. To simplify notation, we will drop the arrows and use the convention that the first number indicates the source surface, and the second the impinged upon surface. The view factor F_{22} is understood as how much the outer object can see itself beyond the shadow of the inner object, and the inner object intuitively always can see the outer (therefore $F_{1\to 2=1}$), where in the reversed situation it is the sum that equals one ($F_{22}+F_{21}=1$). Counting up all of the sources of energy flux between the objects, every inward going emission/ reflection from a surface has one part that will hit the next internal surface governed by the fraction $F_{outer\to inner}$, and the rest impinges the source surface governed by the fraction $F_{outer\to outer}$. We have assumed that each of these objects outer surfaces are perfectly convex, therefore no radiation from outward going radiation can impinge the object emitting/reflecting it without an intermediate reflection from an external concave surface. The upshot of this point is that for every flow of energy there is an infinite sum of reflections that are, as before, reduced in magnitude by the reflection. However, each of those incident reflections are additionally split up and infinitely summed and reduced by the view factor coefficients. For example in Fig. 2.9, in accounting for the heat sources absorbed by the heat shield, the first emission of radiation from the container, P_3, can impinge on the outer surface of the heat shield with a view factor of F_{32}, reflect with a view factor of $F_{23}=1$, and then re-reflect off of the container with that new radiation splitting by another view factor which would become

$$T = a_2 P_3 \sum_{i=0}^{\infty} (\rho_2 F_{23} \rho_3 S)^i, \tag{2.10}$$

where the secondary bounces are described by an infinite sum, S, which accounts for bounces off of the outer surface splitting up to shine F_{33} amount of power on itself and F_{32} back on the inner surface,

$$\begin{aligned} S &= (F_{32} + F_{33}\rho_3(F_{32} + F_{33}\rho_3(F_{32} + F_{33}\rho_3(\dots \\ &= F_{32} \sum_{j=0}^{\infty} (F_{33}\rho_3)^j \\ &= \frac{F_{32}}{1 - F_{33}\rho_3} \end{aligned} \tag{2.11}$$

Inserting S into equation 2.10, the total sum, T, just becomes

$$T = a_2 P_3 \times \frac{F_{33}\rho_3 - 1}{F_{33}\rho_3 + F_{23}F_{32}\rho_2\rho_3 - 1}. \tag{2.12}$$

This only accounts for one of the sources which would replace the a_2P_3 term in P_{HS} from equation 2.9. For all of the conditions in the previous example, this effect changes that specific term from originally 10.9 W, to become 8.8 W, which is a sizeable effect and could be considered for all of the sources if one had an apparatus with significantly asymmetric view factors. However, in a practical sense, this effect is not so dramatic for our situation of thermally isolating our nozzle and is not carried out further here.

2.2.4 Cryogenic thermometry

The cryogenic nozzle is mounted to the cryostat with a copper adapter where the temperature sensing and control is attached (shown in Fig. 2.10). A resistive heater (Lakeshore Cryotronics HTR-50) is installed with a set screw into the copper mount, and clamped to the mount is a silicon diode temperature probe (Lakeshore Cryotronics DT-670 SD). There are a few choices of cryogenic sensor, but the silicon diode is the lowest cost high performance sensor at cryogenic temperatures. The sensor is placed with the shortest heat bridge between it and the heater to reduce thermal delay from the feedback system. The combination of sensor plus heater allows for both feedback controlled temperature stabilization. The temperature is controlled with a Stanford Research Systems (SRS) temperature controller unit, model CTC 100. The silicon diode is a bare chip which has very low thermal mass. This is beneficial, but the wiring to the sensor needs to be considered carefully so as to not to make the temperature sensing inaccurate since copper wires connected at one end to 300 K will directly heat the sensor, influencing the measurement to read an incorrect elevated temperature when the nozzle is likely cold. There are a few options made to make thermometry as accurate as possible.

First, the temperature probe is connected by a four-wire arrangement which allows for the current sensing mechanism of the temperature controller ECU to depend less on the wire resistances. Second, as was previously mentioned, the wires themselves being good thermal conductors con-

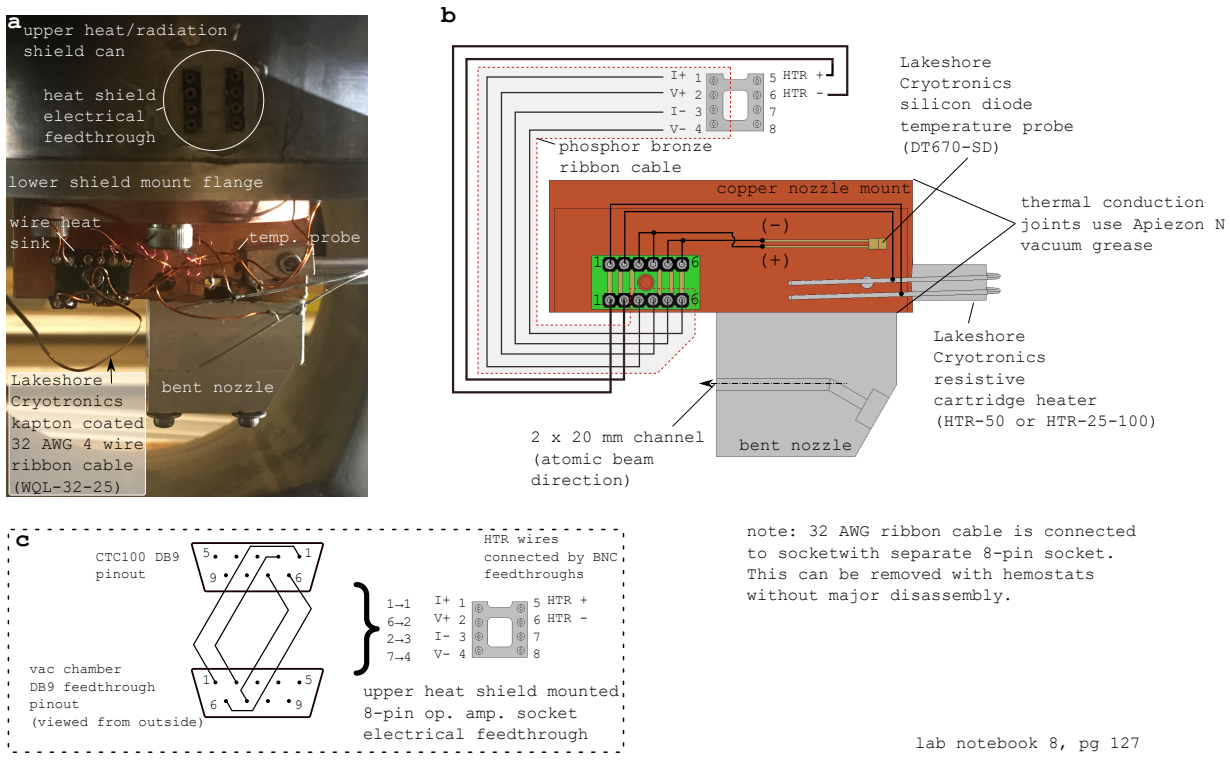

Figure 2.10: **a)** photograph of the nozzle assembly with the heat shield separated and the teflon tube removed. The wiring passes through a homemade thermal heat sink (described in the next figure). **b)** A diagram of the nozzle wiring from the heat shield electrical feed through (circled at the top of **a**). Cryogenic components purchased from Lakeshore Cryotronics. The 32 AWG four wire ribbon cable (Lakeshore, WQL-32-25) is narrow gauge and made of phosphor bronze to reduce the heat conducted to the temperature probe to remove systematics. This is also why the wiring is directly heat sunk to the cold head. A 50 ohm resistive heater is installed on the nozzle to heat the system for temperature stability control. A close bridge between the temperature sensor and the heater is needed to speed up the low frequency corner of the temperature stabilization loop. **c)** wiring diagram for the temperature controller connections to the heat shield electrical feed through.

tribute significant heat load directly to the silicon diode. The first step in limiting this is to use Phosphor-bronze wire, which has $1.6\,\mathrm{W\,m^{-1}\,K^{-1}}$ thermal conductivity at 4 K as compared to pure copper which has a thermal conductivity of $300\,\mathrm{W\,m^{-1}\,K^{-1}}$. The second step is to thermally heat sink the wires to the cryogenic nozzle as shown in Figs. 2.10 and 2.11. This means that the heat carried down the wires themselves will be extracted by the cryohead before it can reach the sensor and shift the measurements. The heat sink is made of a simple printed circuit board with 6 pins connected directly to 6 other pins with the copper intentionally deposited on the lower layer of the PCB. Simple through hole connectors are soldered to the pins for the temperature controller cable

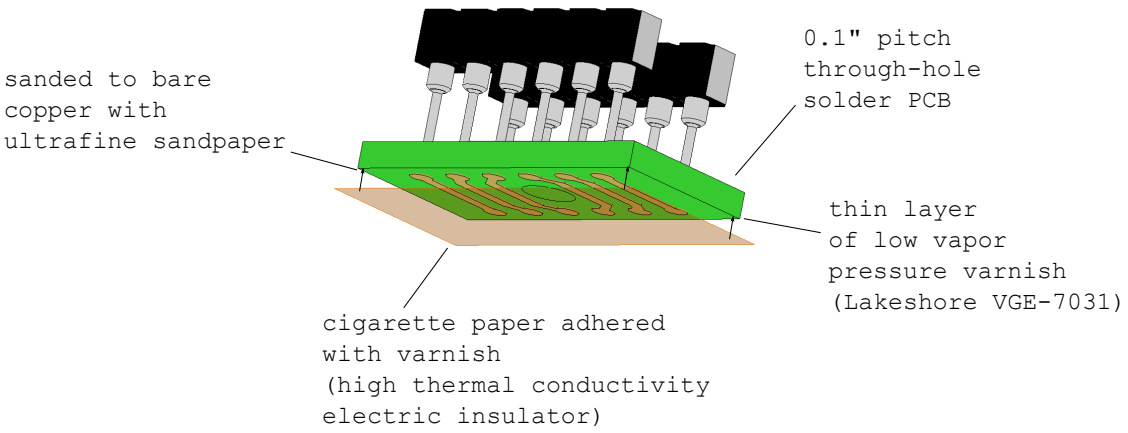

Figure 2.11: Closeup of the wire heat sink to the nozzle assembly. The wires are attached on the sensing end to the temperature controller which is at room temperature. Although phosphor bronze wire has high thermal resistance, a non-negligible heat load will still propagate down the wires and cause significant error in the temperature sensing because of the very low thermal mass of the silicon diode. The electrically insulating layer of varnish and cigarette paper adhered directly to the bare copper makes very good thermal contact with the cyrostat and therefore the wires directly connected to the sensor can be assumed to be in thermal equilibrium with the nozzle.

to connect to on the input, and the output to connect to the sensor. The lowest electrical insulation layer is sanded down so that bare copper is present on the bottom of the PCB. A very thin layer of varnish is painted over the copper, and a slip of cigarette paper cut to size is layed over the varnish. Cigarette paper is chosen because it is very thin and a decent thermal conductor while remaining an electrical insulator at all temperatures.

All of the mechanical connections between cryogenic components that must be in good thermal contact with the refrigeration system are coupled with a layer of Apiezon N vacuum grease. The grease is designed to be vacuum compatible at pressures from 1 ATM down to high vacuum, but also the N specific grease is designed to crystalize at low temperatures becoming highly thermally conductive whereas many other greases that do not solidify will lose their thermal conductivity at low temperatures.

2.2.5 Recombination

The recombination of H to molecular hydrogen needs to be considered in the design of the apparatus. The molecule is ≈4.5-4.8 eV lower in binding energy than two separate atoms [70, 71].

Because of this energy difference, the hydrogen recombination reaction is exothermic and must release the energy difference out of the system. However, because the energy is not released as radiation, the two-body recombination for the chemical reaction is ultimately suppressed from occurring if there is no third particle to absorb the energy from the atoms. This means that in order for atoms to recombine, they must interact with a third body, i.e. - a surface or third particle simultaneously. In the case of simultaneous three body recombination, it is highly suppressed in a rarefied gas in the molecular flow regime. This leaves surfaces as the only available way that atomic hydrogen may recombine. Surfaces catalyze hydrogen recombining into a molecule both by providing a third body to sink the binding energy difference and by giving a lower dimensional space for atoms to find each other, greatly increasing the interaction probabilities [72, 73].

Only a few surface compositions are ideal to mitigate surface recombination of atomic hydrogen [11, 72–75]. The best surface is a film of superfluid helium, which was used at MIT during the experiments using a dilution refrigerator [70]. The second best surface is a solid made from frozen H_2, which occurs naturally on the cryogenic nozzle below the freezing point of H_2 [76]. At room temperature however, it has previously been found that polytetrafluoroethylene (PTFE, Teflon) exhibits a large reduction in recombination losses, and this is why the ducting following the discharge region, shown in Fig. 2.4, is made from Teflon [11, 77].

Teflon has low thermal conductivity ($0.3\,\mathrm{W\,m^{-1}\,K^{-1}}$) which is reduced at low temperature [78]. This is the reason that Teflon is not used as the cryogenic beam formation nozzle which operates in the range of 5 K. Also, with a molecular and atomic hydrogen flow mixture entering the cryogenic nozzle, the surface of the nozzle will quickly form molecular hydrogen ice which becomes the new surface for recombination. Because of this, the choice of metal for the nozzle should be a material with a high thermal conductivity so that the gas heat load may be removed by the cryocooler. Initially our choice of nozzle material was copper. However, when testing atomic fluxes with an quadrupole mass spectrometer or residual gas analyzer (RGA) we noticed that aluminum performed with more hydrogen flux for the same nozzle geometry and operating conditions. In the case of copper, we saw that at the Teflon tube to copper nozzle interface, there was a significant

darkened and discolored surface quality as well as reduced flux as compared to aluminum. These observations are consistent with the findings in [11]. Further tests could be performed for different materials, though it is important to consider the low temperature thermal conductivity of the nozzle choice, and pure aluminum alloys perform very well at cryogenic temperatures, nearly as well as copper [79–81]. Pure aluminum remains untested as a nozzle in our lab and open for future analysis. Additionally, the work in [72] show that palladium and tungsten have an order of magnitude lower recombination coefficient for hydrogen at high temperatures. If at low temperatures the performance is similar, they may be a good option for the beam cooling material choice. These materials are relatively expensive compared to 6061 aluminum, but perhaps can be applied to the inner surfaces of the nozzle as a coating which should limit the saturation of the aluminum surface with H_2 and possibly lead to larger atomic H flux.

The only non teflon or cryogenic hydrogen facing surfaces before the nozzle occur in the microwave dissociation region. This means that the recombination losses in this region could be high and it would be advantageous to use a surface composition that is favorable for low recombination such as a Teflon coating on the quartz containment tube to increase atomic beam flux. An upgrade such as this would require testing since Teflon has yet to be shown to work at temperatures much greater than room temperature (typical microwave hydrogen plasmas range in temperatures up to 800 K [82, 83]), and any significant amount of coating eroding and chemical reactions would likely lead to contamination of the gas components that follow the molecular discharge region. Some research could be done to search for a material with low surface mobility and low adsorption probability for atomic hydrogen at high temperatures. Additionally, water-cooling or higher thermal conductivity glass/crystal could be used to reduce the discharge surface temperatures.

2.2.6 Gas delivery cleanliness

Contamination on the Teflon surfaces greatly increases recombination losses and has been observed in our lab to reduce the atomic flux by at least an order of magnitude in the worst cases. Cleanliness of the gas lines is a high priority for preserving the atomic flux and leak-free UHV

protocols should be followed for the hydrogen delivery side of the vacuum system, even though the gas pressures are well above low-vacuum in the forelines. The cleaning procedure that follows has been found to successfully refresh the surfaces of the Teflon hydrogen nozzle delivery tubes.

Teflon delivery tube cleaning protocol:

- Begin by cleaning the Teflon tube in separate baths of isopropanol and methanol in a ultrasonic cleaner two to four times.
- After sonicating the Teflon tubes in a warm to hot solvent bath for approximately 20 minutes for each bath, a thorough solvent rinse where isopropanol is run through the tube for an additional 20 minutes.
- Then dried by a clean dry air flow immediately before installation in the vacuum apparatus.

This same procedure should be done for the quartz microwave discharge tube and conductance limiting aperture, except with the additional step of scrubbing the inside with a cotton swab. This procedure has not shown a significant recovery of atomic flux in the long term, and replacing the quartz tube after many operation hours has been seen to recover the down stream atomic beam flux. We have the suspicion that chemical contamination leads to the atomic beam operation freezing when operated at cryogenic temperatures. After many hours, the quartz tube has been seen to have a large discolored region within the microwave cavity. When this becomes impossible to clean off of the quartz tube, it is a good idea to replace it. Typical conductance limiting aperture sizes that have worked well for our experiments have been between 400 and 600 microns, and this part should be replaced from time to time.

The nozzle is made of 6061 aluminum and is cooled with a closed cycle Gifford-McMahon cryostat (Sumitomo RDK-408D2 4K) and the temperature is measured with a silicon diode (Lakeshore Cryotronics DT-670) located on the outside surface of the nozzle. The nozzle geometry is optimized for thermalization for which a selection of configurations are discussed in Section 4.2. The cryostat reaches temperatures as low as $\approx$5 K – slightly greater than the absolute quoted minimum specification due to the thermal load of wires attached to a heater cartridge

within the nozzle. With the discharge on, the temperature of the nozzle rises by 0.5 - 1.5 K due to the heat load of the gas and additionally hydrogen recombination. With this heat load, there is a small thermal gradient between the inside nozzle surface and the temperature probe, which causes the temperature of the thermalized gas to be slightly higher than the measured temperature.

2.3 Detection of hydrogen

The detection of atomic hydrogen is most sensitively accomplished with spectroscopy. Laser spectrsocopy however is challenging to build from scratch for use in the initial development of an atomic beam, therefore some intermediate method is necessary. Several methods for initial confirmation for the production of atomic hydrogen in the ground state were attempted, including imaging recombination radiation, a thin film nickle-oxide, a bare MEMS thermopile pyroelectric sensor. We were able to confirm the production of hydrogen by observing an electronic signal from the thermopile resistor circuit when illuminated with the atomic hydrogen beam as well as observe a green optical emission from hydrogen recombination interacting with aluminum surfaces. These methods were able to confirm the generation of H_1, however they were deemed unsatisfactory for long term use. Since the work of [75] demonstrated the reliable usage of an RGA as a H_1 detector, we decided to also use this method. We purchased a model RGA100 quadrupole mass spectrum analyzer from Stanford Research Systems (SRS) for this purpose. Standard off the shelf RGA devices are inherently bad at detecting the low masses due to the "zero-blast" problem[‡]. This is due to the fact that Paul trap based detection at low mass requires turning down the trap voltages which are less effective at destabilizing the higher charge to mass ratio orbits through the trap without having very long quadrupole rails. This means that when set to detect at 1 amu for atomic hydrogen, a large background is present composed of many higher mass constituents. In order to have the greatest dynamic range for the RGA, we elected to have a Channel Electron Multiplier installed for detection of highly rarefied signals and to have sensitivity of small changes on a large background. RGA detectors are usually applied for sweeping mass spectroscopy scans,

[‡]See SRS RGA100 operating/user's manual.

so to use the RGA for a single mass detection requires a few extra steps. First an SMB cable must be connected to the Analog out port pictured in Fig. 2.12, which allows the analog current signal to be taken from the ECU's electrometer. The Serial output program "RGAComm" is used then to communicate with the RGA and send individual control commands. A list of the useful commands is listed in Fig. 2.12 as well. Unfortunately the RGA control, "ML", does not allow for values less than 2 to be selected, so the mass axis had to be recalibrated by changing the RGA setting "RI" from its original value of -8.59 to a new value of -16.91. The CEM preamplifier is based on an AD825 op-amp, and is 50 Ohm coupled to the RGA analog port.

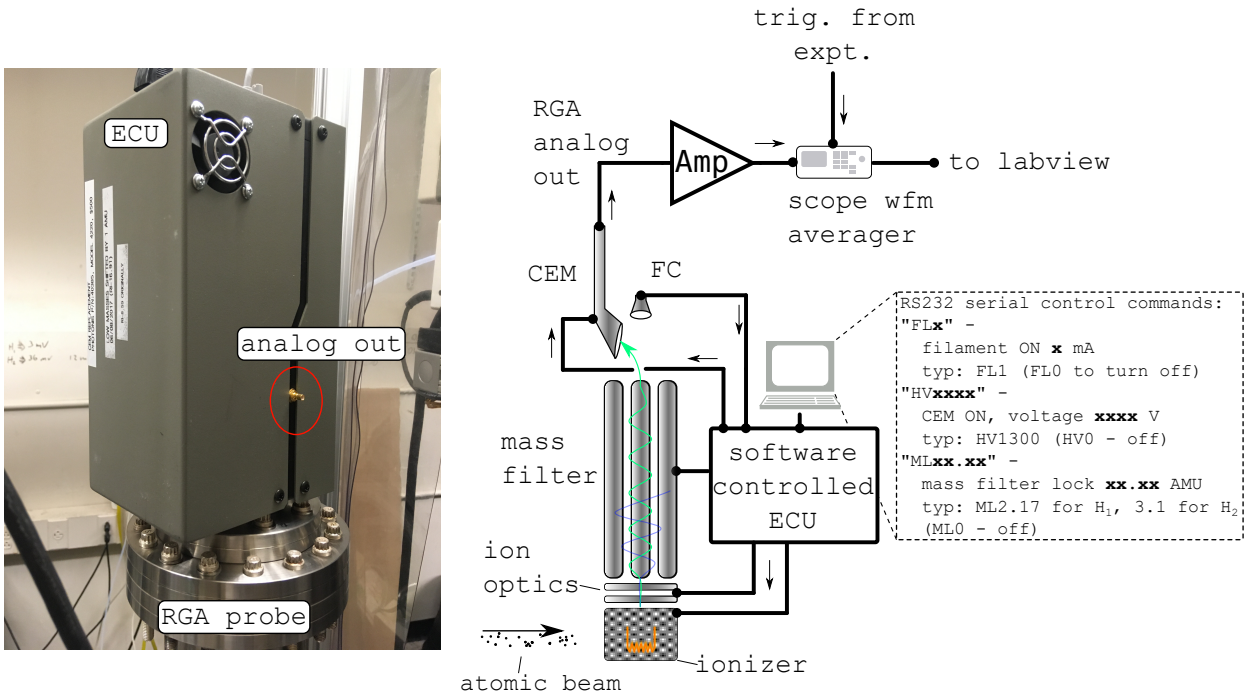

Figure 2.12: RGA setup for high sensitivity detection method for the ground state atomic hydrogen beam. RGA model is Stanford Research Systems (SRS) RGA100 which has the ability to scan from 1 to 100 amu, and has the Channel Electron Multiplier (CEM) option as well as an analog output for collecting signals directly off of the CEM. When the analog output method was used, the CEM current is detected and amplified with an op-amp circuit, averaged on an oscilloscope and recorded for further averaging with LabView. Turning on the CEM voltage bypasses the Faraday Cup (FC). SRS software serial output controls the mass filter, ionizer and CEM can be used to record mass scans from either CEM or FC. The waveform averager is a Tektronix 1032B digital oscilloscope, and is typically triggered off of the chopper encoder for velocity distribution measurements. Mass filter values are shifted up by approximately 1 AMU for low masses, therefore 2.17 is H_1, and 3.1 is H_2. Changing the mass RGA mass calibration can be found in the manual under the peak tuning section.

Chapter 3

Metastable atomic beam

In order to perform the metastable deceleration of a metastable hydrogen beam, we must also have the ability to excite our atomic beam to the metastable 2S state using two-photon excitation at a wavelength of 243 nm. The 1S-2S energy interval is now known with a small fractional uncertainty of 4.2×10^{-15} [6]. Two-photon excitation to the 2S state requires high power, narrow bandwidth radiation, and developing these sources has been actively pursued for many decades [84–86]. While 50 to 100 mW was routinely produced [87] prior to the work in [54], for experiments on hydrogen and other two-body atomic systems, there was significant motivation to power scale these lasers. For example, when performing 1S-2S spectroscopy, additional laser power would allow the beam to be transversely expanded to increase the interaction volume. For normal hydrogen, a larger interaction volume would decrease the time-of-fight broadening and increase the fraction of the atomic beam excited, reducing the statistical uncertainty [6]. Increasing the interaction volume is also pertinent for 1S-2S spectroscopy in antihydrogen [88, 89]. The excitation of this transition in antihydrogen took $\approx$ 300 seconds per data point [90] due to the relatively large trap volume as compared to the interaction volume. As discussed in Chapter 1, laser cooling hydrogen would require Lyman alpha radiation which is challenging to produce. To avoid some of the difficulties which are inherent to Lyman-α laser sources, Zehnle *et. al* proposed using the 1S-2S two-photon transition itself for laser cooling [91]. In contrast to single-photon cooling, this requires radiation at 243 nm, which can be produced and manipulated much more easily. A significant challenge is posed by the average power required. While cavity enhanced 243 nm lasers have previously reached $\approx$ 1 W [87], useful scattering rates for laser cooling would require average power at least an order of magnitude higher [41].

Our plan to generate a beam of metastable 2S atoms also requires high power 243 nm radiation to populate as many atoms as possible into the 2S state. To produce the power necessary for this, we use the high power UV source previous developed in [9, 10] coupled into the power enhance-

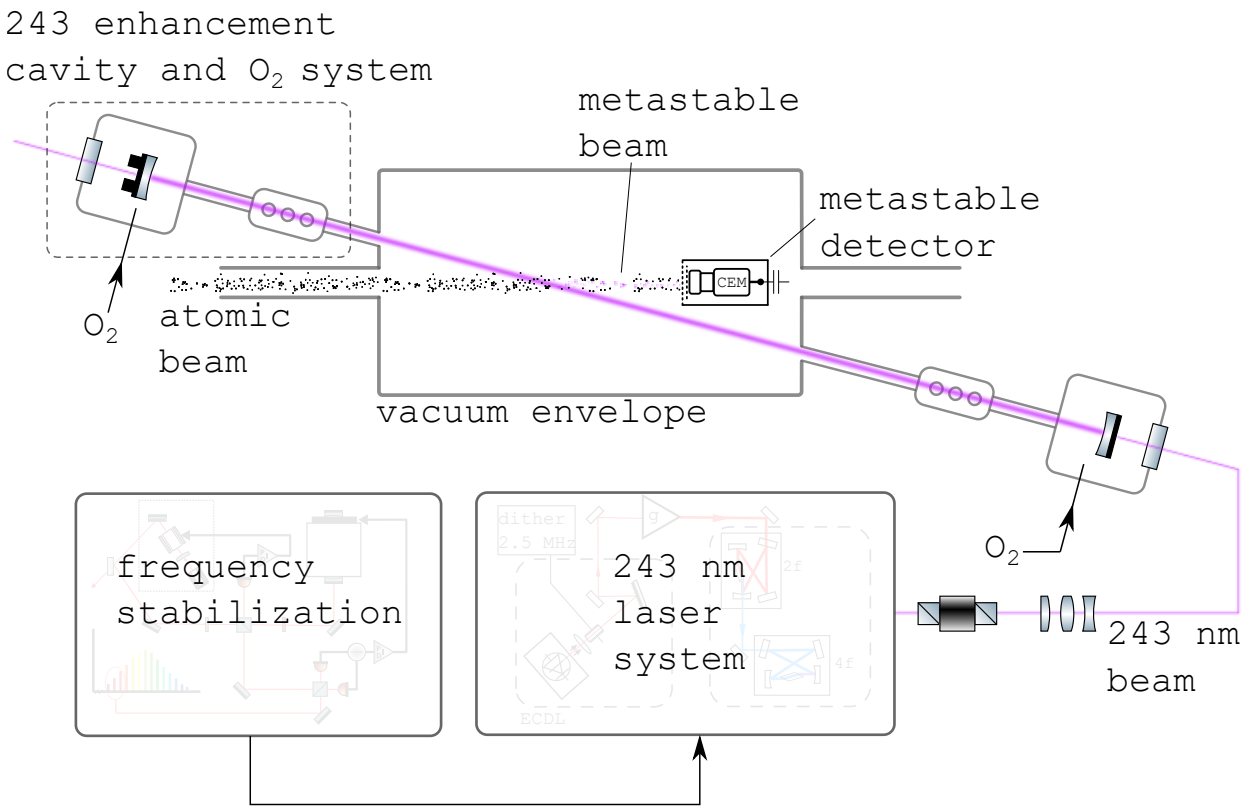

Figure 3.1: Generation of the metastable atomic hydrogen beam. Frequency stabilized 243 nm radiation is coupled through a faraday isolator and cavity mode matching lenses into an in vacuum enhancement cavity. The enhancement cavity mirrors are contained in an oxygen environment to prevent UV degradation and is separated from the high vacuum environment by three differential pumping stages. The atomic beam passes through a cavity enhanced UV beam to excite the 1S-2S transition. The metastable beam is detected in a channel electron multiplier (CEM) where metastables are quenched and Lyman-α (121 nm) photons are counted.

ment cavity described in [54]. The diagram in Fig. 3.1 outlines the process for making a beam of metastable hydrogen. Frequency stabilized 243 nm radiation is coupled through a Faraday isolator and cavity mode matching lenses into an in-vacuum enhancement cavity. The high power 243 nm radiation source is described in section 3.1, and its frequency stabilization is described in section 3.1.2. The enhancement cavity mirrors are contained in an oxygen environment to prevent UV degradation and are separated from the high vacuum environment by three differential pumping stages, more detail for this system is provided in two separate sections. The performance of the UV enhancement cavity as described in [54] is covered in section 3.2.1 and the updated version for the velocity distribution and deceleration experiments in section 3.2.2. The atomic beam passes

through a cavity enhanced UV beam to excite the 1S-2S transition, which is aligned at a 6° angle to increase the interaction time. The metastable hydrogen can be sensitively detected and differentiated from ground state hydrogen by aligning a channel electron multiplier (CEM) to the metastable beam, as described in section 3.3.

3.1 High power 243 nm source

There are a number of difficulties associated with the operation of an enhancement cavity in the deep ultraviolet and with high intracavity power. First, commercially available mirror coatings are only able to achieve reflectivity of about 99.5 %, and for a perfectly impedance matched cavity with no other losses, the maximum enhancement is limited to ≈ 100. Therefore, the only clear avenue to increasing the intracavity power is to first power scale the excitation laser. This was pursued in our previous work, where we demonstrated cw outputs of $\approx 600\,\mathrm{mW}$ at 243 nm [9]. Second, short wavelength optics are known to degrade when exposed to high power due to surface oxygen depletion [92] and hydrocarbon contamination [93]. In the UV [92], and extreme ultraviolet [94], degradation due to both effects has been mitigated by introducing O_2 at the location of the mirrors – albeit at a lower average power than what is required for two-photon laser cooling.

With this, we demonstrate cavity enhanced 243 nm power of $> 30\,\mathrm{W}$ utilizing a high power excitation laser. By flushing the cavity mirrors with O_2 and utilizing differential pumping, we could stably lock the cavity for more than one hour without degradation. As described in [41], this level of intracavity power should be sufficient for an initial demonstration of laser cooling.

3.1.1 243 nm laser

The 243 nm laser used for the excitation of our enhancement cavity was previously described in [9, 10], with more detail in [95, 96], and an abbreviated schematic is shown in Fig. 3.2. First, a 972 nm laser diode seed is amplified by a commercial tapered amplifier (TA) and a Yb-fiber amplifier. The Yb-fiber amplifier allowed for power scaling and operated at 972 nm where the system behaves effectively as a 3-level system [97]. After amplification, the 972 nm light is frequency

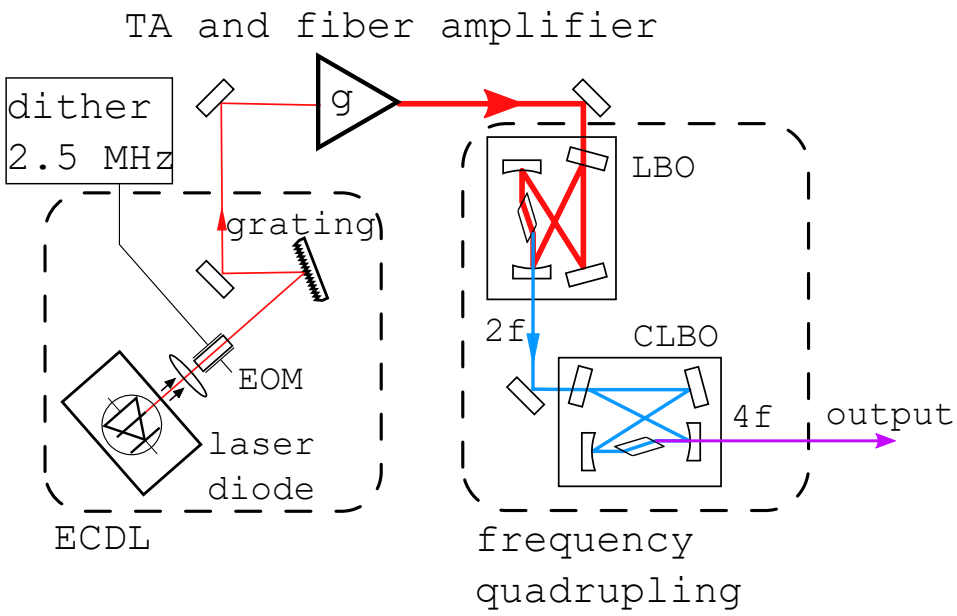

Figure 3.2: The master oscillator is an extended cavity diode laser (ECDL) at 972 nm and amplified as in [9,10]. An EOM within the cavity applies a 2.5 MHz dither for locking the three subsequent enhancement cavities. The IR light is frequency quadrupled with two bow-tie enhancement cavities – first from 972 nm to 486 nm using LBO with noncritical phase matching, then to 243 nm using CLBO with critical phase matching.

quadrupled to 243 nm using two successive resonant doubling stages. For the first doubling stage, we use an LBO crystal in a noncritical phase matching configuration which produces a symmetric 486 nm beam profile due to the absence of walk-off effects. For the second doubling stage, we use a CLBO crystal in a critical phase matching configuration, which produces an elliptic beam with an aspect ratio of roughly three-to-one. This source is able to consistently produce ≈ 650 mW of 243 nm power. With careful alignment, we have observed > 1 W of 243 nm power, although it is difficult to maintain the higher power over long term time scales without realignment of the system. We attribute this behavior to thermal instability since we have observed no degradation of the CLBO crystal – even under the highest power conditions.

The transverse beam profile of the 243 nm radiation source must be known for optimal mode-matching to the enhancement cavity. Since the walk-off in the last doubling cavity produces an elliptic profile, cylindrical lenses are necessary to reshape the beam. The output from the CLBO cavity is reshaped with two cylindrical lenses and one spherical lens, and the beam profile was

analyzed with a home made UV beam profiler based on fluorescence from a ceramic beam screen and a monochromatic camera which is shown in fig. 3.3. As is standard and well known, the spatial beam profile in multiple z-locations after the output of the laser allows for a reconstruction of the beam propagation parameters which are useful for calculating the coupling and mode matching overlap of the source beam and an enhancement cavity.

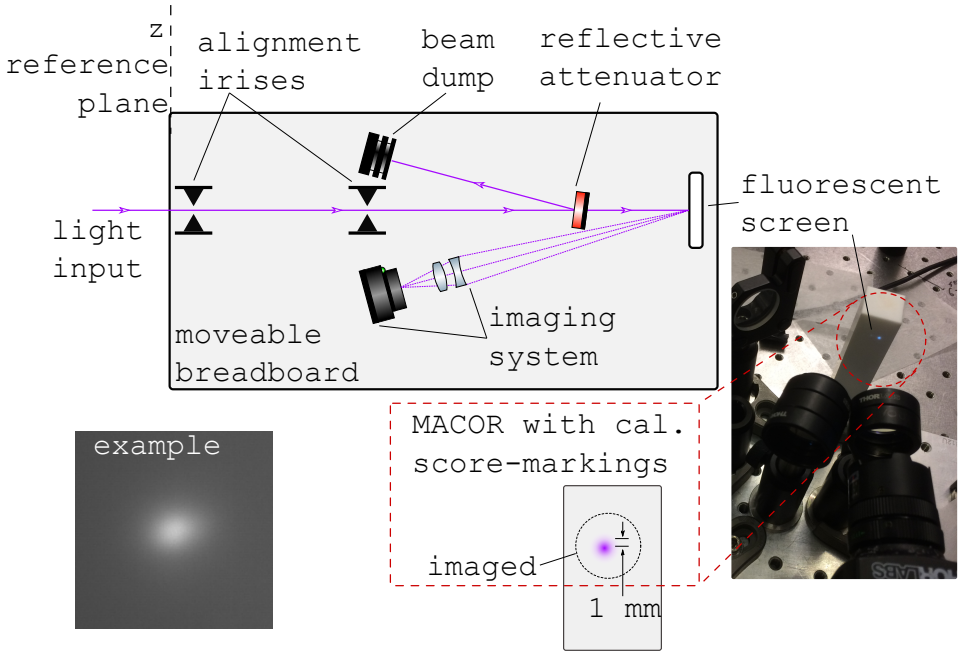

Figure 3.3: Diagram of beam profiling system used to analyze the transverse beam quality of the UV laser and cavity transmission. A moveable breadboard with a flat reference plane to measure z-distances was mounted with a UV fluorescent screen made of MACOR. A monochrome camera imaged the fluorescent spot, and the pixel spacing of the image was calibrated with a 1 mm spaced calibration scoremark on the MACOR surface. The UV power was attenuated to keep any nonlinearity of the beam spot to a minimum.

Figure 3.4 shows the beam profile in two different locations separated by 1.14 m after reshaping. As can be seen, the beam has a nearly symmetric, Gaussian intensity profile. As shown in Fig. 3.6, the mode-matching optics are followed by a polarizing beam splitter and $\lambda/4$ waveplate, which are used to isolate the cavity from the second doubling stage during the performance tests of the cavity, however linear polarization and a Faraday isolator were used for atomic excitation experiments (section 3.2.2). In general, transmission optics in the DUV suffer from high loss. Each

optic used for mode-matching and beam isolation have losses ranging from 1% to 8%. This results in a maximum stable power at the cavity input of 420 mW.

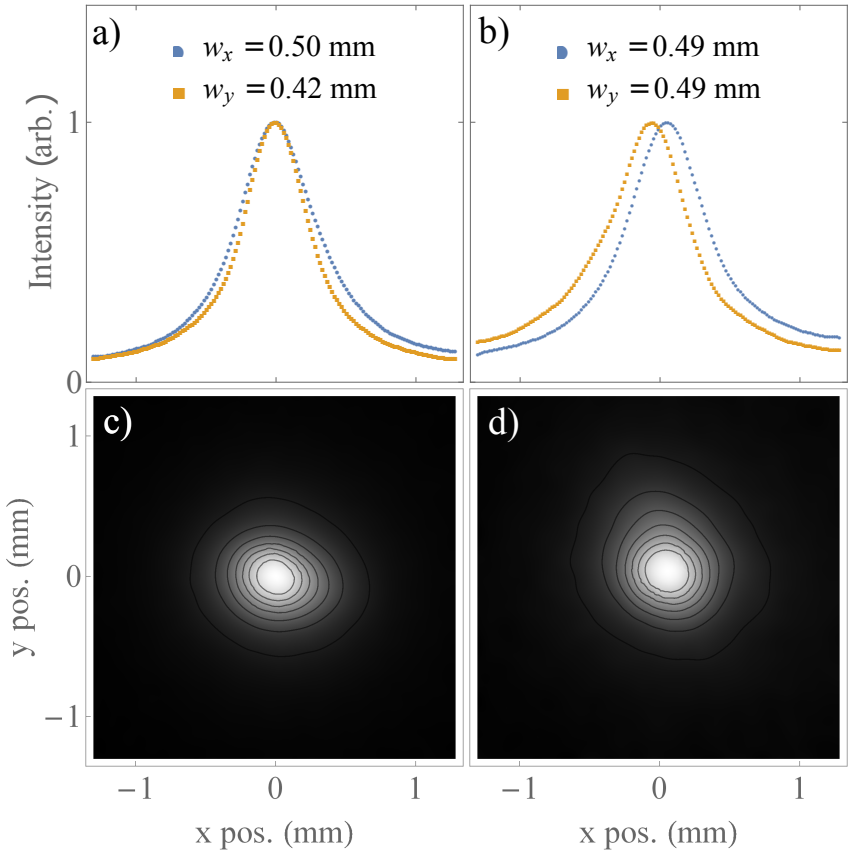

Figure 3.4: a) Profile of the laser output directly after the telescoping lenses, b) profiles of the laser output 114 cm after the lenses. c) Image corresponding to the profiles in a). d) Image corresponding to the profiles in b). The beam images are taken at a power of 386 mW. The w parameters correspond to the $1/e^2$ intensity radii of the Gaussian fits.

3.1.2 243 nm source frequency stabilization

Excitation of the narrow 1.3 Hz 1S-2S line requires a narrow-line frequency stabilized source. As shown in Fig. 3.5, we accomplish the frequency stabilization using a beatnote with a frequency comb, and reduce the free-running linewidth of the ECDL by locking it to a stable cavity because the free-running 972 nm ECDL was not capable of a coherent beatnote lock to the frequency comb without first reducing its noise. Using an electro optical modulator (EOM) we perform a PDH

lock [98] to an optical cavity (finesse, $\mathscr{F} > 3000$) with an Invar steel alloy hollow spacer with one of the highly reflecting mirrors mounted with an annular PZT. By tightly locking the ECDL using a fast modulator in the laser oscillator, the laser will follow the noise profile of the stabilization cavity, and also follow the change in frequency when the cavity length is adjusted by the PZT. To control the laser frequency, we use the comb to 972 nm laser beatnote to provide feedback to the cavity spacer's length. The frequency comb is self referenced for the carrier offset frequency, f_0. The repetition rate is stabilized to a beatnote with a 1550 nm Rio Lasers stable laser which is locked to an ultrastable 15 cm notch cavity made by Stable Laser Systems. The frequency comb's absolute frequency reference is estabilished by the lock modulation frequencies which are referenced to a 10 MHz signal from Rb atomic clock, (Model FS740 from Stanford Research Systems). More detail about the design of the frequency comb and its feedback locks are covered in [96].

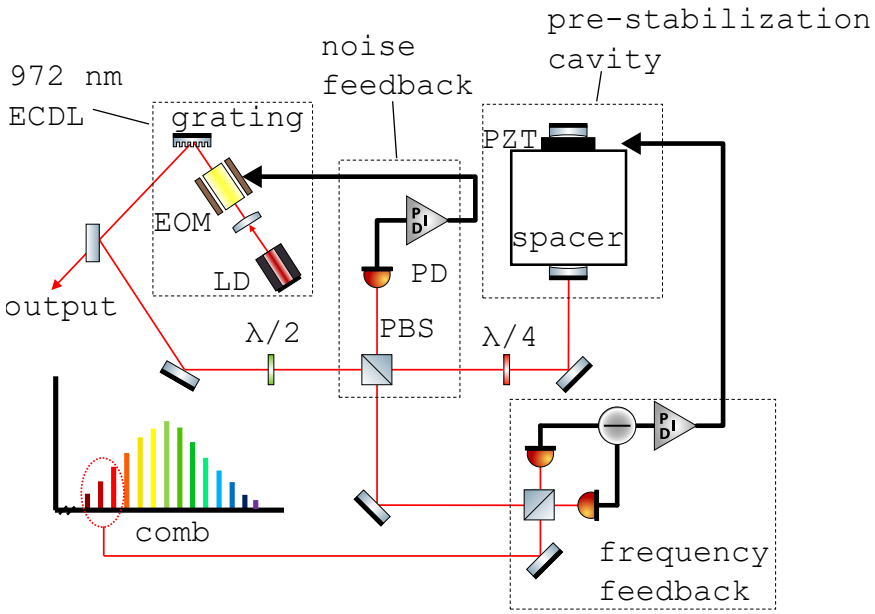

Figure 3.5: Frequency and noise stabilization of the 972 nm ECDL seed for the high power 243 nm laser source. The output from the ECDL is picked off and split between a beatnote with the frequency comb and a high finesse cavity. The portion of light to the high finesse cavity is PDH locked by dithering an EOM in the ECDL cavity, and the frequency feedback from the comb-972 beatnote is fed back onto the length of the high finesse cavity, giving the ability to frequency tune and stabilize the 972 nm laser.

3.2 UV enhancement cavity

3.2.1 UV cavity benchmark

For the performance tests of the enhancement cavity prior to the slowing work (found in [54]), the enhancement cavity is formed with a high reflector (HR) with a radius of curvature $R = 4\,\mathrm{m}$ and a flat input coupler (IC) spaced by 0.75 m (free spectral range, FSR = 200 MHz). The resonant TEM_{00} mode of the cavity has a focus at the input coupler with a calculated beam waist of $w_0 = 350\ \mu\mathrm{m}$. The calculated waist at the curved high reflector is $w_0 = 390\ \mu\mathrm{m}$ so that the best mode-matching is achieved with a nearly collimated input beam. By numerically propagating the beam defined by the profiles in Fig. 3.4 to the input coupler, we found that the overlap with the enhancement cavity TEM_{00} mode is $\approx 90\%$.

The dielectric cavity mirrors were designed for high power and high reflectivity using electron beam evaporation (LaserOptik GmbH). The mirrors have a SiO_2 top surface layer which according to [92] is helpful to reduce oxygen depletion of the coating. Since we expected combined absorption and scattering losses of 0.5% for both cavity optics, we chose the input coupler to have a 1.5% transmission so that the cavity is slightly overcoupled. Figure 3.7 shows the cavity transmission as the length is scanned. From the ratio of the resonance widths to the FSR, we estimate that the finesse is ≈ 300.

We carefully calibrated the transmission of the high reflector. As shown in Fig. 3.6, we monitor the transmission with a GaP photodiode to determine the intracavity power. When scanning over the resonance, the intracavity power reaches 38 W with an input power of 420 mW. This corresponds to a buildup of ≈ 92. As can be seen in Fig. 3.7, there is minimal excitation of higher-order cavity modes due to imperfect mode-matching and more than 80% of the power is within the TEM_{00} mode. When taking into account the buildup, finesse, reflected power, and mode-matching factor, we estimate that the total scattering and absorption loss of the cavity is $\approx 0.8\%$. This is slightly better than the 1% estimate from the mirror manufacturer.

The enhancement cavity is kept on resonance using a Pound-Drever-Hall (PDH) locking scheme [98]. For this, we generate sidebands on the fundamental radiation at 972 nm using an

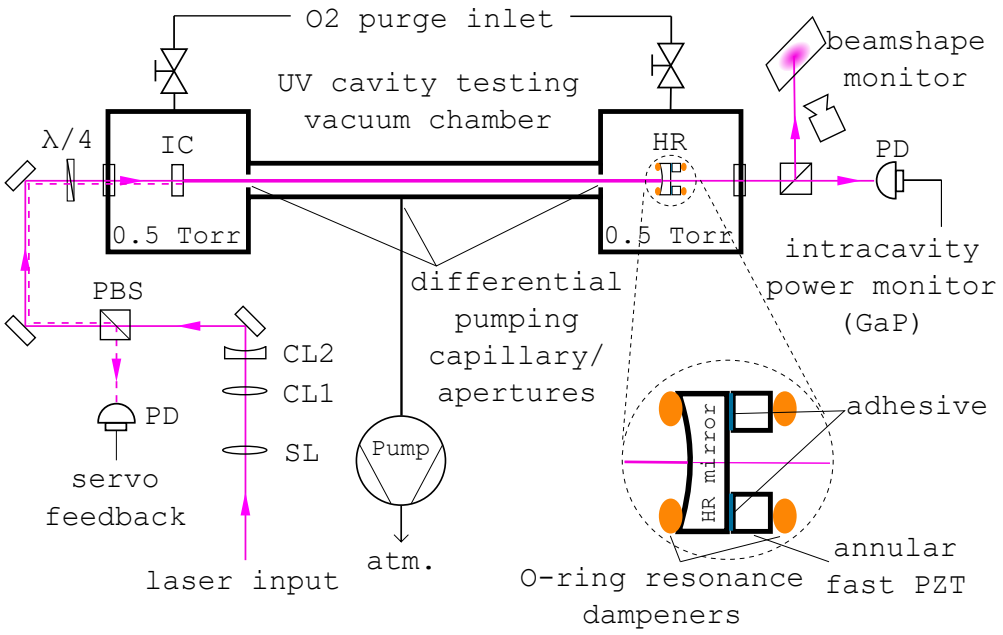

Figure 3.6: Diagram of enhancement cavity prior to the installation in the spectroscopy and slowing experiment. The input 243 nm beam is mode matched to the cavity using one spherical lens (SL) and two cylindrical lenses (CL1 and CL2). The reflection from the input coupler (IC) is optically isolated from the laser with a polarizing beam splitter (PBS) and quarter waveplate ($\lambda/4$). The transmission of the high reflector (HR) is monitored with a photodiode (PD) to determine the intracavity power. Only one stage of differential pumping was used for these tests.

electro-optic modulator (EOM) within the master oscillator. The sidebands are also imprinted on the quadrupled radiation which are used to generate a PDH error signal for the DUV enhancement cavity. As shown in Fig. 3.6, the cavity is locked to the laser utilizing a fast piezo-electric transducer (PZT). The fast PZT is annular so that we can measure the light transmitted through the high reflecting mirror. We use the mirror mounting procedure in [99] to damp low frequency resonances, which is crucial to maintain a stable lock. We estimate our locking bandwidth is $\sim$ 10 kHz and the measured amplitude noise is $< 3\%$. When locked, we measure a peak intracavity power of 33.7 W circulating with a build up 80.4 and an input of 420 mW. The PZT mounted cavity mirror is itself on an optical stage whose position is adjusted with a large throw PZT, which compensates for slow drifts.

When compared with the maximum buildup as the cavity is scanned over the resonance, the locked intracavity power is consistently 10 % lower (as indicated in Fig. 3.7a). The power decays to this steady state value within 40 ms after the lock is engaged. The behavior was similar for

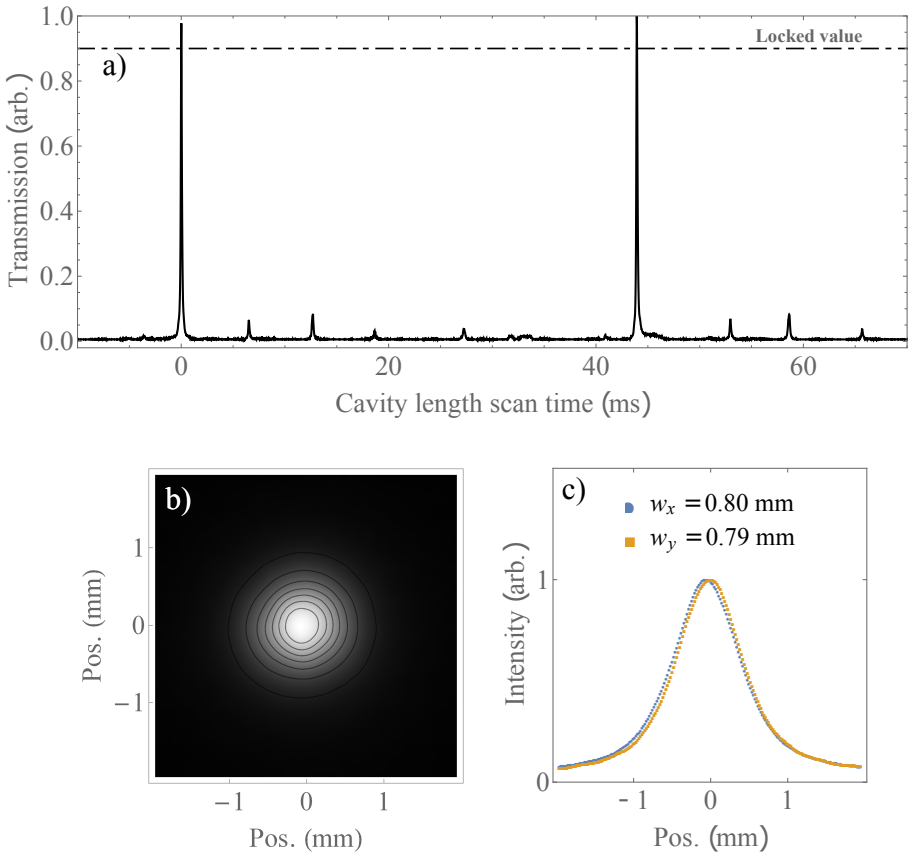

Figure 3.7: a) Cavity transmission as a function of frequency. The resonance width allows us to estimate the finesse to be ≈ 300 with $> 80\,\%$ of the power in the TEM_{00} mode. b) Image of cavity transmission with 31 W of intracavity power. The image was taken 65.5 cm after the output coupler with a build up of 75. c) Cavity transmission profile.

all intracavity powers above 10 W. Due to the time scale, we attribute this behavior to heating of the cavity mirror coatings. However, we monitored the transmitted beam profile simultaneously (as shown in Fig. 3.7b–c) and we observed that the beam shape was nearly Gaussian and that its profile did not change noticeably with power.

We designed the enhancement cavity to operate within a differentially pumped vacuum system with a continuous inlet of ultra high purity oxygen gas. We tested the pressure limits for our mirrors at high locked intracavity powers (10 to 30 W) and found that at oxygen pressures lower than 500 mTorr, the mirrors would quickly degrade over the course of a few minutes as evidenced by severely reduced buildup factors. Inspection of the mirror surfaces after operation without an O_2 background revealed contamination on the surface which could be cleaned off with organic

solvents. Therefore, instead of oxygen depletion, we believe the main cause of degradation is due to residual hydrocarbons within the vacuum chamber which are cracked when exposed to high power UV radiation and contaminate the mirror surfaces [93]. This supports the findings of [92], where they found a top surface layer of SiO_2 prevented degradation due to surface oxygen depletion. We observed that thorough cleaning of the vacuum chamber and optical components increased the run time before degradation. With 500 mTorr of O_2 at the mirror surfaces, the optical cavity could be locked with > 30 W of optical power for more than 1 hour without evidence of degradation of the locked intracavity power and buildup. Although 0.5 Torr of O_2 is required at the mirror surfaces, we later used three stages of differential pumping could reduce the pressure in an interaction region to $< 10^{-7}$ Torr for later experiments.

The linear dependence of the intracavity power as a function of input power is shown in Fig. 3.8. As the power of the laser is increased by increasing the Yb-fiber amplifier pump power, we observed that the vertical waist of the beam at the output of the final doubling stage increases slightly. We attribute this to a thermal variation in the CLBO crystal. To compensate for the change in beam shape, we readjusted the cylindrical lenses used to mode-match to the cavity as the laser power was varied. The data in Fig. 3.8 was collected after optimizing the cavity mode-matching at each input power.

With the intracavity power achieved in this work, we are able to estimate a corresponding two-photon cooling rate. When the $2S_{1/2}$ state is fully mixed with the $2P_{3/2}$ state, the on-resonance scattering rate for the 1S-2S transition is 2.8×10^{-7} Hz W^{-2} cm^4 I_{UV}^2 [41]. For a reasonably sized beam waist of 180 µm, 30 W of cw 243 nm radiation leads to a 1 kHz scattering rate. This scattering rate is modest by typical laser cooling standards, but when coupled with the high recoil velocity of hydrogen (3.3 m s^{-1}) fairly rapid cooling cycles are possible. For instance, the slow velocity tail (< 100 m s^{-1}) of a collimated source of cryogenic hydrogen [11] could be cooled to the recoil velocity in 30 ms. We estimate that 3×10^{12} atoms in the interaction region would lead to a negligible round trip optical loss due to two-photon absorption of $< 0.02\%$, leaving the finesse nearly unaffected.

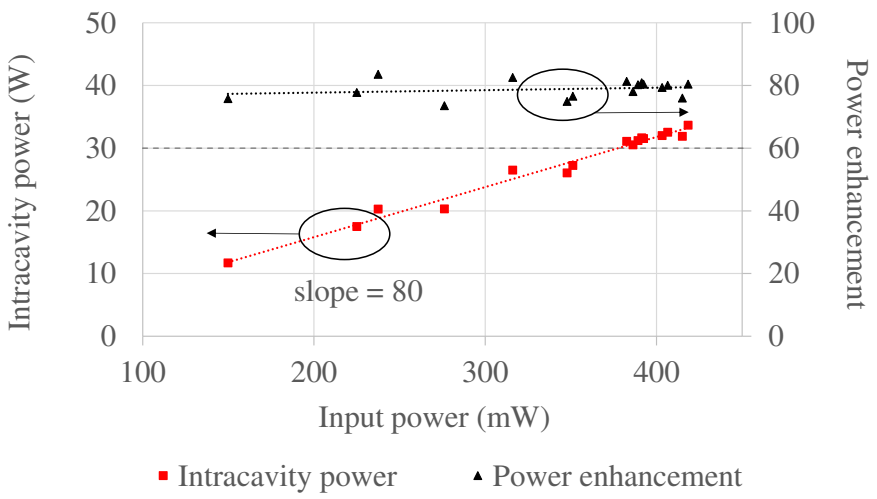

Figure 3.8: Measured power enhancement factor and locked intracavity power as a function of input power. The maximum intracavity power is 33.7 W with an input power of 420 mW. The maximum measured build-up factor was 84 and remained fairly constant over the range of input powers.

In addition to laser cooling for hydrogen and anti-hydrogen, this system could have applications in the spectroscopy of other two-body systems. Notably, our system could be used for 1S-2S spectroscopy of muonium – a bound state of an electron and an antimuon. In [100], the spatial confinement of muonium was demonstrated and the possibility of using cw radiation to measure the 1S-2S transition was extensively discussed. When using cw radiation, systematics related to the finite pulse length (including residual first-order Doppler shift, laser chirp, and AC Stark shifts) would be eliminated. The estimates presented in [100], assumed 4 W of intracavity radiation which would result in a transit-time broadened linewidth of ≈ 1 MHz. With the increased DUV radiation demonstrated here, larger radiation beams could be used which would allow the recovered measurement linewidth to be reduced by a factor of ≈ 3 if all other parameters are held constant. Due to the difference in reduced mass, excitation of the 1S-2S transition in muonium requires radiation at 244.2 nm. We confirmed that the system could be tuned to this wavelength and observed nearly identical performance of the enhancement cavity at the two wavelengths.

In the ideal case benchmark tests, we demonstrated > 30 W of power within a resonant enhancement cavity at 243 nm which should enable a two-photon cooling scheme for atomic hydrogen but more importantly be useful for significant population of the metastable atomic beam. At these high DUV intensities, a local pressure of O_2 is required to prevent mirror degradation. Therefore, implementing the build-up cavity in deceleration and spectroscopy experiments requires additional stages of differential pumping to achieve a high-vacuum hydrogen beam line.

3.2.2 UV cavity updated

The optimal cavity performance was measured in [54]. This system then needed to be coupled to the spectroscopy and slowing apparatus with some changes to accommodate the high vacuum requirements with the O_2 flow. As was previously mentioned, the transmission optics suffer from high losses which means that to have high build up powers in the cavity, there cannot be a transmission obstruction between the input coupler and high reflector of the enhancement cavity. Therefore the differential pumping stages that reduce the pressure from 0.5 Torr to the high vacuum mark must open to pass the optical beam. A background on gas flow in a vacuum system is included in Appendix A. The design of the spectroscopy apparatus from the previous experiment required that each mirror's differential pumping apparatus to be separated by approximately 1 m making a minimum aperture opening constraint on the conductance limiting apertures in the differential pumping manifolds. Due to this minimum aperture size of approximately 2 mm, there was a requirement to have at least three differential pumping stages between the 0.5 Torr region. A design for a three stage differential pumping manifold and its integration into the spectroscopy chamber is shown in Fig. 3.9. A calculation for the pressure stepdown capable of this differential pumping manifold is also included in Appendix A, Fig. A.1.

The new optical path length for the enhancement cavity is approximately 1.8 meters, and both the input coupler and the output coupler are 1 m radius of curvature. This leads to a minimum spot size on the order of 180 microns. The optical beam is overlapped with the atomic beam at a steep

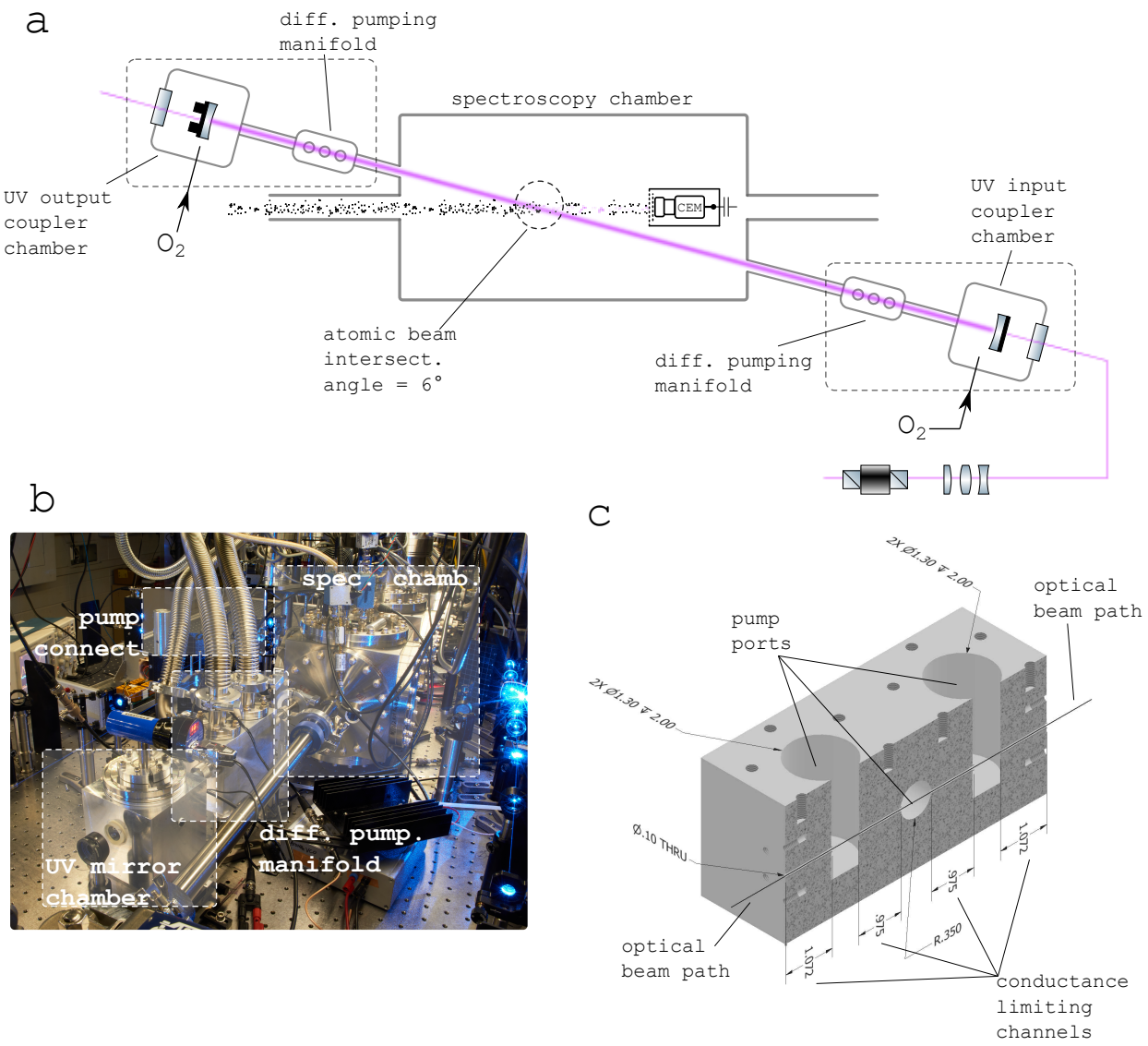

Figure 3.9: a) schematic of differential pumping apparatus to couple the high power UV enhancement cavity which requires 0.5 Torr of O_2 continuously flushing the mirrors. b) overlayed photograph of the input coupler side of the system. c) cutaway of the differential pumping manifold which is monolithic and made of 6061 aluminum.

angle of 6° in order to increase the transit time of the atoms and improve the optical excitation of the 1S-2S transition.

3.3 Metastable beam detection

It is important for the slowing experiment as well as future experiments precision measurement to be able to detect metastable 2S hydrogen specifically. The Lyman-α (121 nm) fluorescence

emitted by a 2S atom decaying to the 1S state when quenched makes it a strong signal for the presence of metastable atoms. Metastable 2S hydrogen has a lifetime of approximately 122 ms however, when the atom is in the presence of a electric field, the 2S state partially mixes with the short-lived 2P state (1.6 ns) which decays back to the ground state [101, 102]. The lifetime of a metastable 2S hydrogen stark mixed with the nearby 2P states in a constant uniform electric field, E, is described by the Lamb-Bethe expression [101, 102]

$$\frac{1}{\tau'_{2S}} = \gamma_P E^2 \left(\frac{d_{ab}^2}{\hbar^2 \left[\omega_{ab}^2 + (\gamma_P/2)^2 \right]} + \frac{d_{ac}^2}{\hbar^2 \left[\omega_{ac}^2 + (\gamma_P/2)^2 \right]} \right), \tag{3.1}$$

where a, b, c are $n = 2$ manifold states $2S_{1/2}$, $2P_{1/2}$, $2P_{3/2}$ respectively, the dipole matrix elements are $d_{ab} = \langle a|ez|b\rangle = d_{ac} = \langle a|ez|c\rangle \approx -3ea_0$, and $\gamma_P \equiv 1/\tau_{2P}$ is the natural linewidth of the 2P states. In equation 3.1, $\omega_{ab/ac}$ are the energy spacings between the levels ab/ac respectively, e is the charge of an electron, and a_0 is the Bohr radius. In this case we ignore the 2-photon decay from the 2S to 1S with a decay rate of approximately $8.2\,\mathrm{s}^{-1}$. All of the quantities in equation 3.1 can be analytically determined with high accuracy. The decay rate γ_P can be determined from the spontaneous emission rate relationship

$$\gamma_P = \frac{\omega_{2P1S}^3 \, d_{2P1S}^2}{3\pi\varepsilon_0 \hbar c^3}, \tag{3.2}$$

where ω_{2P1S}^3 and d_{2P1S} are the energy spacing and dipole matrix elements for the 2P to 1S states respectively and the rest are fundamental constants. The 2P to 1S dipole matrix element is $d_{2P1S} \approx 0.74ea_0$, and $\omega_{2P1S} = 2\pi \times 2.466 \times 10^{15}\ \mathrm{s}^{-1}$. The 2P decay rate is then $\gamma_P = 6.3 \times 10^8\ \mathrm{s}^{-1}$ which leads to the well known 2P lifetime of 1.6 ns. Since ω_{ac} is about ten times greater than the Lamb shift, ω_{ab}, we can ignore the second term in equation 3.1, which gives the 2S lifetime's inverse quadratic dependence on a static electric field

$$\tau'_{2S} = \frac{1}{\gamma_P E^2} \left(\frac{\hbar^2 \left[\omega_{ab}^2 + (\gamma_P/2)^2 \right]}{d_{ab}^2} \right) \approx \frac{1.21}{E^2} \mathrm{s} \times \mathrm{m}^2/\mathrm{V}^2. \tag{3.3}$$

The expressions used in equations 3.1 assume small polarizing fields as compared to the binding energy of the atoms. The lifetime of 2S atoms in a static electric field will then be $\tau_{quench} \approx (1/\tau_{2S}^{(natural)}) + 1/\tau'_{2S})^{-1}$. At zero field, the atoms will decay to the 1S state through two-photon emission with a rate of $8.2\,\mathrm{s}^{-1}$, but a field of $350\,\mathrm{V\,m}^{-1}$ would lead to 10 µs lifetimes. Electric fields on this level are very easy to apply as a 5 V difference across a separation of 1.5 cm is equivalent to a $350\,\mathrm{V\,m}^{-1}$ electric field. A typical cryogenic atom travelling 300 m/s would have a 99.3% chance of decaying in the time it takes to cross the across this 1.5 cm gap. For reference, a plot of the 2S lifetime as a function of electric field is plotted in Fig. 3.10. Due to the 2S lifetime's inherent sensitivity to electric fields presented here, it is necessary to shield the 2S atoms from electric fields in a Faraday cage once they are excited in the beam. We surround all of the regions after 1S-2S excitation with a graphite coated Faraday cage for all of the experiments carried out on the metastable atoms to extend the lifetime of the atoms as long as possible.

The Lyman-α radiation emitted after a 2S atom is quenched is most easily detected with a photo multiplier tube (PMT) or channel electron multiplier (CEM). Our metastable detection method uses a CEM to count metastable fluorescence which is shown in Fig. 3.11. There must be a near zero field in the regions outside of the metastable detector, therefore the detector is enclosed entirely inside of a grounded box with a mesh grid inlet. An electron repeller grid sits directly after the grounded grid to reject background photo electrons that are present in the 1S-2S excitation chamber. Metastable atoms are quenched in this region. The CEM is biased to approximately 2.7 kV, and the electron current pulses for each 121 nm emission are counted through a high pass filter. Output pulses are between 20 mV and 200 mV, and approximately 20 ns in duration. For pseudo-analog measurements such as the metastable velocity distribution measurement in Chapter 4, a pulse discriminator and standardizer circuit is necessary.

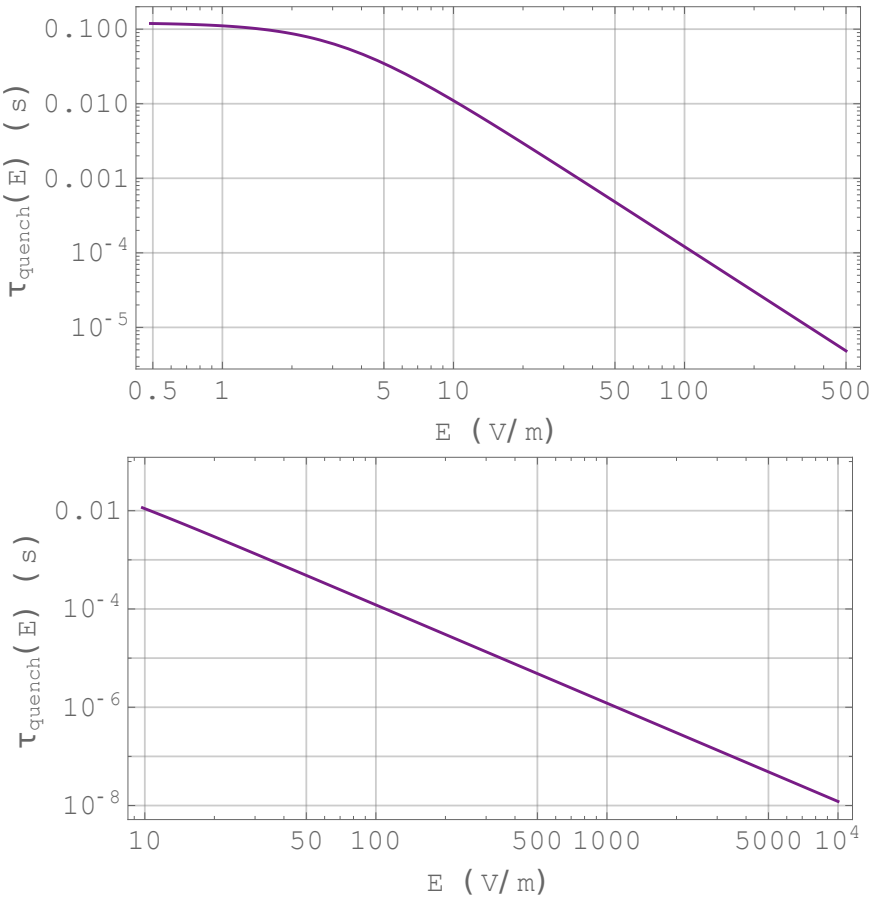

Figure 3.10: Lifetime of the 2S atom in a static electric field for quenching and detection of metastable flux.

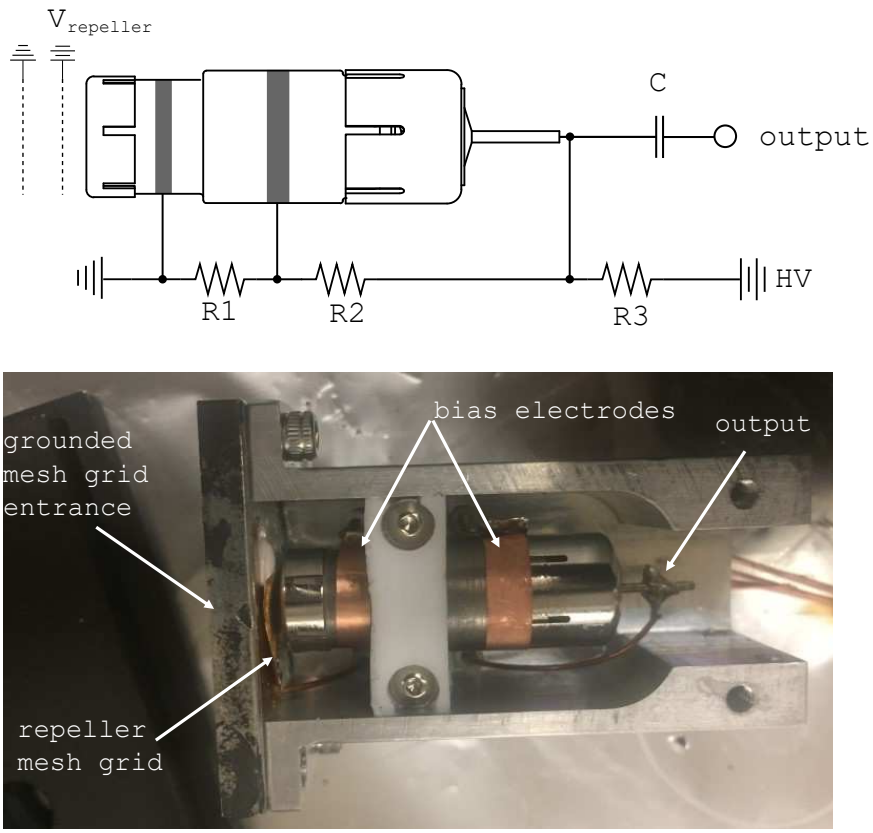

Figure 3.11: Metastable atom detector based on a Burle Magnum 5901 channel electron multiplier (CEM). The CEM is housed in a grounded box, with a photo-electron repeller grid entrance. Lyman-α photocurrent pulses are counted through a high pass filter at the output of the CEM. Large resistors in a voltage divider circuit bias the lead-glass amplification region. $R1 = 20$ kΩ, $R2 = 2$ MΩ, $R3 = 24$ MΩ

Chapter 4

Velocity characterization and nozzle study

Previously, Walraven and Silvera performed time-of-flight measurements using an atomic beam chopper and a residual gas analyzer (RGA) to detect ground state atomic hydrogen [11]. A similar implementation using a tuning fork chopper and hexapole magnetic lenses to perform velocity selection has been performed within the ASACUSA collaboration [103, 104]. These techniques are advantageous in that the methods are simple and direct, and the data are easily interpreted. However, while these techniques are sensitive to atomic hydrogen, they do not distinguish between ground state and 2S hydrogen – the signal for many 2S-nL experiments.

This chapter covers the characterization of the ground state and metastable velocity distributions [12]. We perform these measurements by directly chopping the atomic beam and doing time-of-flight (TOF) measurements of the atomic beam. The atomic beam chopper used for these experiments is shown in Fig. 4.2. We also study how nozzle geometry affects the beam's velocity distribution and present a nozzle design that produces a near Maxwellian velocity distribution. The dependence of the velocity distribution on nozzle geometry highlights the uncertainty if in situ measurements are not performed, and provides insight into the formation and thermalization of the atomic beam. A layout of the apparatus for determining the velocity distribution of the atomic beam is shown in Fig. 4.1

Design of the chopper went through a few iterations that worked suboptimally before landing on the design in Fig. 4.2. Placing a rapidly spinning device in vacuum presents a few challenges. An in vacuum motor would need a way of sinking the heat to the exterior of the vacuum chamber, which would be solved with a metallic thermal bridge or water cooling. In all of our designs we elected to avoid this kind of complication. Our first design used a homemade in vacuum 90-degree gearbox based on a 1:3 ring and pinion gear run in reverse for a rotational velocity step-up of three. Because this is in vacuum, there needs to be either no lubricants, otherwise very serious contamination would be unavoidable, other than high vacuum grease. The mechanical

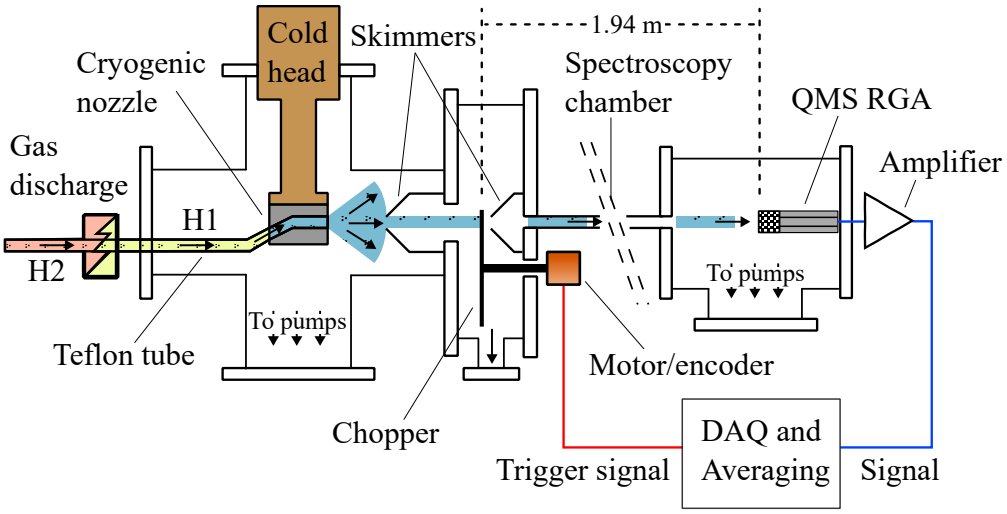

Figure 4.1: Experimental setup for ground state detection. The atomic beam is generated by passing H_2 gas through a microwave discharge, then cooling the gas with a closed-loop helium cryocooler (Sumitomo RDK-408D2 4K). The nozzle and second 4.9 mm skimmer, which are separated by 450 mm, define the atomic beam divergence to ∼10 mrad. The atomic beam is modulated by a mechanical chopper, and neutral atoms are detected with a residual gas analyzer (RGA). Reproduced from Cooper, S. F. *et al. Rev. Sci. Instrum.* **91** 013201 (2020), with the permission of AIP Publishing.

design of this concept without lubrication caused rapid wear, vibrations and resonances were very large even at low speeds, and the gearbox concept failed very quickly. With this chopper we were limited to a chop rate of a few RPM. A redesign using an offset chopper blade mounted to an 8-inch con-flat flange allowed for direct drive of the chopper blade allowing for rotation frequencies above 21 Hz. The rotational feedthrough used to drive the chopper blade for UHV is magnetically coupled (PN:MD16NDX000Z). One known characteristic of magnetically coupled rotation feedthroughs is that the alignment of the magnetic poles may hop if too much torque is attempted to transmit through the shaft. This can be avoided as long as the ramp speed of the drive says below the breakaway torque of 0.18 Nm, which will keep the clocking angle of the chopper should known. For alignment of the chopper blade opening to the atomic beam, we use a marking on the exterior shaft of the rotary feedthrough. This opening spans roughly over a 22° range of angle. If automating the electronic control of the chopper blade, it is best to program in a slow ramp rate of so that the magnetic poles do not need to transmit too great of a torque and the poles jump resulting in a shift of the angle alignment.

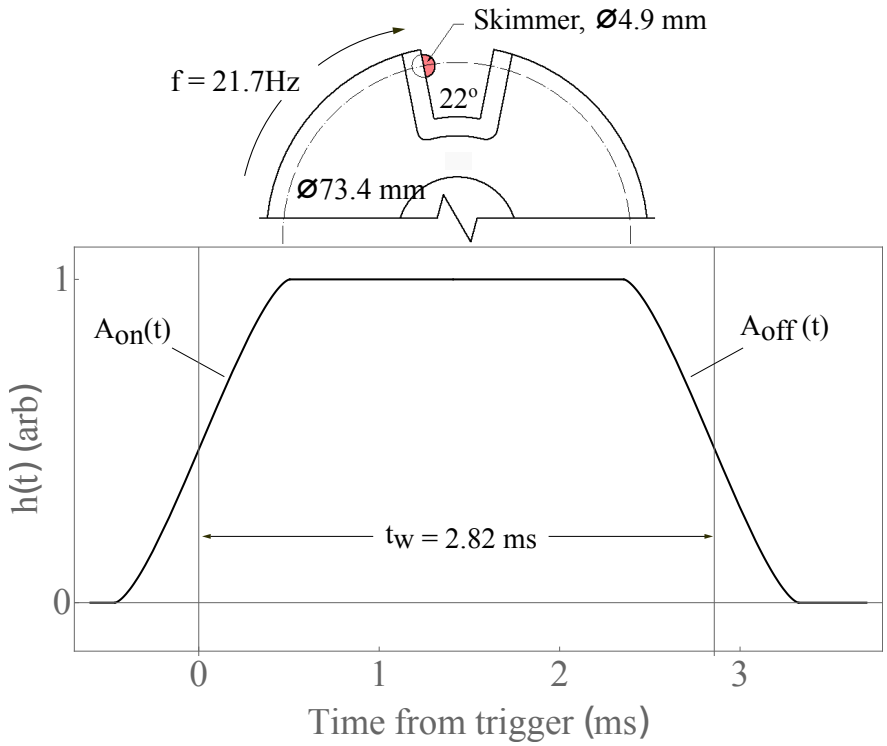

Figure 4.2: The chopper and transfer function, $h(t)$. The separation between the leading and falling edges of $h(t)$ is determined by the angle of the chopper opening and the rotational frequency, $\theta/(2\pi f) = 2.82$ ms. The duration of $A_{on/off} = 0.97$ ms and the duty cycle is ≈6%. Reproduced from Cooper, S. F. *et al. Rev. Sci. Instrum.* **91** 013201 (2020), with the permission of AIP Publishing.

The resolution of a TOF measurement is improved by going to longer beamlines and narrower chopping windows, with the limit being an ideal delta function. However, there would be no detectable signal at a delta-function wide chopper hole, and the maximum resolution for a TOF measurement is constrained by the geometry of the chopper and the velocity distribution of the atoms at a given temperature. Because the pulses of atoms disperse throughout the distance following the chopping window, there is a maximum distance before the low speed portion of a pulse overlaps the next pulse's high speed region.

4.1 Model

The measured signal time-of-flight (TOF) signal, $S(t)$, is related to the TOF distribution, $P_t(t)$, through the convolution

$$S(t) = h(t) * P_t(t), \tag{4.1}$$

where $h(t)$ is a kernel describing the chopper opening function. The velocity distribution, $P_v(v)$, is related to $P_t(t)$ through

$$P_t(t) = P_v\left(\frac{\Delta x}{t}\right)\frac{\Delta x}{t^2} \tag{4.2}$$

where Δx is the distance from the chopper to the detector. Therefore, to find the velocity distribution, $P_v(v)$, one can deconvolve $S(t)$ with $h(t)$ to find $P_t(t)$, and then use Eq. 4.2. Unfortunately, numeric deconvolution algorithms produce non-unique solutions, which also contain method dependent oscillations. Therefore, it is more straightforward to perform the reverse operation – to assume a velocity distribution and then compare the modeled $S(t)$ with the measured data.

Regardless of which procedure is used, it is crucial that the chopper transfer function $h(t)$ be known precisely. For our system, $h(t)$ is shown in Fig. 4.2. The overall width of $h(t)$ is set by the size of the chopper opening, R, the rotation frequency of the chopper, f, and the radius of the opening from the chopper rotation axis, R_c. Although estimating the leading and falling edges of $h(t)$ as linear would give a reasonable approximation to the chopper transfer function, the actual leading and falling curves, $A_{on/off}(t)$, can also easily be found with a straightforward integral given by

$$A_{on}(t) = \int_{-\mathrm{R}}^{x(\mathrm{t})} 2\sqrt{\mathrm{R}^2 - \mathrm{x}'^2}\, d\mathrm{x}' \tag{4.3}$$

$$A_{off}(t) = 1 - A_{on}(t - t_w), \tag{4.4}$$

where $x(t) = 2\pi f R_c t$ is the position of the chopper blade over the orifice and t_w is the time between the leading and falling edges of the chopper. The resulting transfer function is the analytic piecewise function in Fig. 4.2, where $t = 0$ is the time at which the rotary encoder triggers the signal scan.

4.1.1 Ground state time-of-flight detection

In order to perform time-of-flight detection, the atomic beam is chopped, and the ground-state hydrogen is detected with the RGA, which is 1940 mm away from the chopper within a separate detection chamber. The chopper is a singly segmented chopper blade (6% duty cycle) driven by a DC motor, which is schematically shown in Fig. 4.1 and the dimensions of the chopper as well as kernel parameters are shown in Fig. 4.2. A rotary position encoder provides a trigger pulse every revolution to synchronize the opening time of the chopper blade with a trigger rate of 21.6 Hz.

The RGA is a quadrupole mass spectrometer type which is locked to the mass 1 peak (as described in section 4.1.1) and uses a channel electron multiplier (CEM) to amplify the ion signal. There is a significant background signal due to residual gases present in the detection chamber at the base pressure of $\sim 5 \times 10^{-8}$ Torr. This background, along with the noise inherent to the RGA mass peak-lock function, limits the signal-to-noise ratio of a single trace. Therefore, traces are averaged 128 times on an oscilloscope, then transferred to a computer where consecutive traces are averaged. A typical run consist of 500 x 128 averaged trigger events collected over a few hours. A sample waveform recovered through this procedure is shown in Fig. 4.3. The red points show the data smoothed using the procedure described in [11].

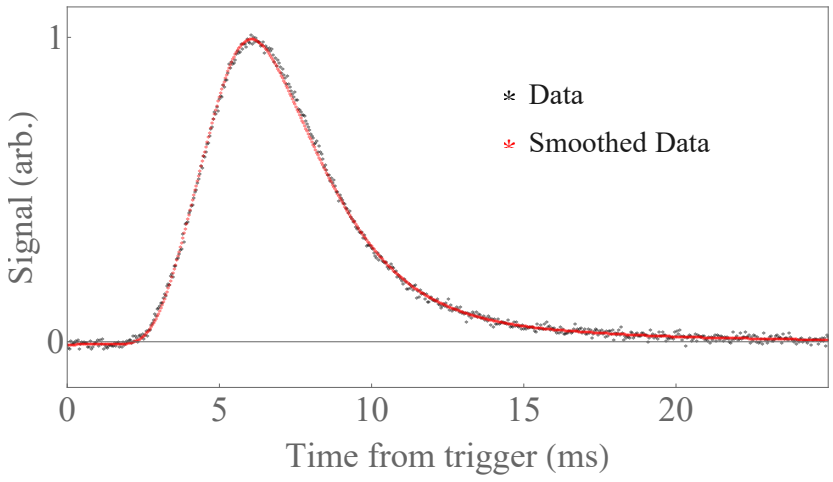

Figure 4.3: Averaged raw RGA data. The temperature of the nozzle as measured with the silicon diode is 5 K. The data shown in red is further smoothed using the Gaussian convolution method in [11]. Reproduced from Cooper, S. F. *et al. Rev. Sci. Instrum.* **91** 013201 (2020), with the permission of AIP Publishing.

4.2 Nozzle Study

For the ground state atoms in a beam, the expected flux distribution for a Maxwellian is $P(v) \propto v^3 e^{-\beta v^2}$ [105], where $\beta = m_{h_1}/(2k_B T)$. However, since the probability of a neutral atom being ionized within the RGA is proportional to the time spent within the ionizer – and therefore inversely proportional to the velocity – the detected velocity distribution is modeled as

$$P(v) = \alpha v^2 e^{-\beta v^2}. \tag{4.5}$$

Due to day to day drifts in the atomic beam flux, RGA mass filter, and RGA CEM sensitivity, the normalization factor α must be a fit parameter. The temperature is also treated as a fit parameter allowing for the possibility that the measured temperature of the nozzle as measured with the silicon diode may not precisely agree with the actual temperature of the beam which we have observed to be the case.

The first nozzle is the straight design shown in Fig. 4.4a. A similar nozzle geometry was used in [11, 103, 104], which provided the main impetus for this test. As is seen by the presence of signal at short times in Fig. 4.4b, a simple Maxwellian distribution inadequately reproduces the experimental results. The clear line of sight from the teflon tube to the detector led us to believe that the distribution may be made of multiple temperatures. Therefore, we adapted our model to include the sum of multiple Maxwellians at separate temperatures. A least squares fit found good agreement with two velocity distributions at 70 K and 7 K (Fig. 4.4b), with their relative amplitudes (0.29 and 0.71 respectively). The presence of the 70 K Maxwellian is reasonable given that the Teflon tube connecting the discharge to the cryogenic nozzle has a temperature gradient and certain atomic trajectories will avoid contact with the cold aluminum nozzle. The velocity distribution that corresponds to the modeled $S(t)$ is displayed in Fig. 4.4c.

The second nozzle investigated is shown in Fig. 4.5a. It has a through-hole which allows for a spectroscopy laser beam to propagate along the axis of the atomic beam similar to those used in references [6, 29, 106, 107]. The nozzle opening is only 1.5 mm in diameter which produced

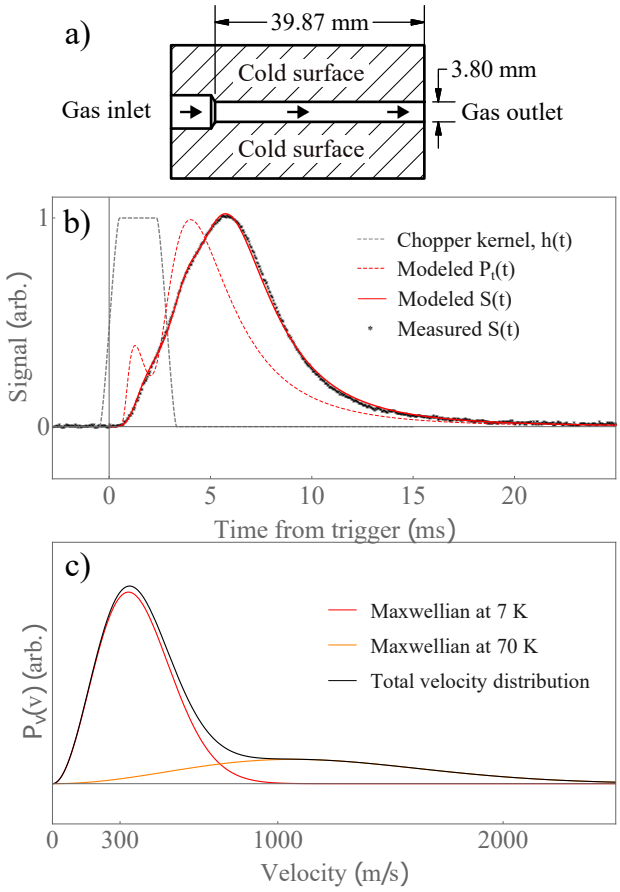

Figure 4.4: a) Straight nozzle similar to that used in [11]. b) The solid red curve is the convolution of the dashed red and grey curves as per Section 4.1. The dashed red curve is the sum of two Maxwellians at 70 and 7 K with 0.29 and 0.71 fractional weights respectively, compared to data smoothed per Section 4.1.1. c) The corresponding velocity distribution. Reproduced from Cooper, S. F. *et al. Rev. Sci. Instrum.* **91** 013201 (2020), with the permission of AIP Publishing.

lower flux. In addition, the nozzle geometry produces less peaking in the forward direction than one with a tubular shape. Due to the long propagation distance in our apparatus, these features contribute to the reduced signal-to-noise shown in Fig. 4.5b-c. For this nozzle design, flux detected downstream at the RGA is likely affected by atomic collisions since there is limited direct line of sight between the inner surfaces of the nozzle and the RGA. Figure 4.5b shows the expected delay distributions for a Maxwellian at the measured temperature. Even with the reduced SNR, it is clear that this model does not reproduce the measured time of flight. However, as is shown in Fig. 4.5c, by replacing the v^2 prefactor in the modeled velocity distribution with v^4, much better agreement is possible. This apparent lack of slow atoms could be the result of the "Zacharias

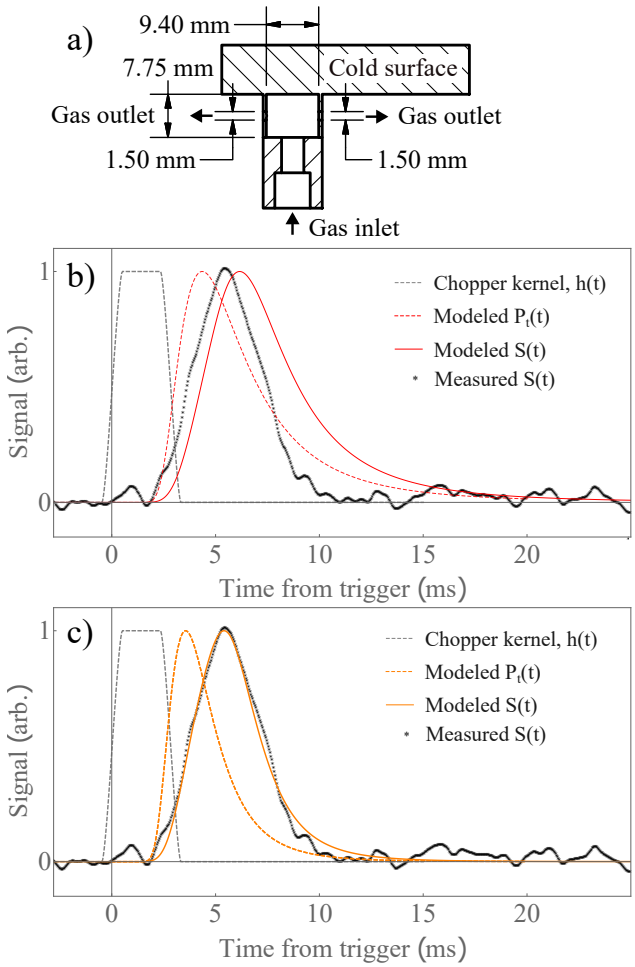

Figure 4.5: a) Through-hole nozzle design. b) Time-of-flight data, smoothed per Section 4.1.1. The red curves correspond to Maxwellian velocity distributions with v^2 prefactors at the measured temperature of 6K. c) Same data as in b, except compared to a Maxwellian distribution with a v^4 prefactor at the measured temperature. Although the SNR limits the conclusions that can be drawn from this data, it is likely that the velocity distribution is strongly influenced by collisions in the nozzle. Reproduced from Cooper, S. F. *et al. Rev. Sci. Instrum.* **91** 013201 (2020), with the permission of AIP Publishing.

effect"– a phenomena where slow atoms are collisionally expelled from the beam by faster atoms [105, 108–111].

The final nozzle investigated has an angled channel and is shown in Fig. 4.6a. Based on simple design considerations, this nozzle design was anticipated to perform well since it has a relatively high conductance and the detector has a line of sight to cryogenic surfaces of the nozzle. We expect this to have good thermalization, unlike the previous nozzle where on axis atoms must exit the nozzle by colliding with another atom or H_2 molecule. The time-of-flight data for the angled

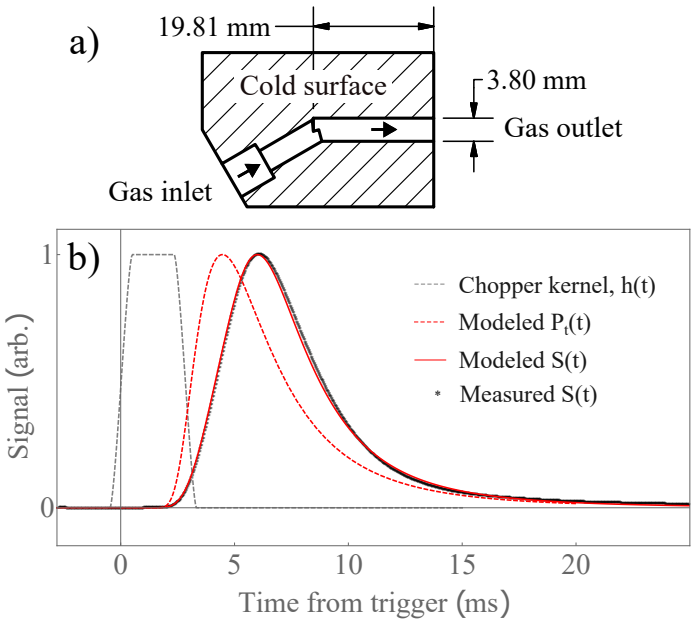

Figure 4.6: a) Bent nozzle design. b) Ground state detection model and data at 5 K (as measured with the silicon diode) for the bent nozzle design. Data smoothed per Section 4.1.1. The solid red curve comes from numerically convolving the red dashed 6.5 K Maxwellian with the grey dashed kernel following Section 4.1. The close fit demonstrates that the design is effective for thermalizing the atomic beam to the cryogenic nozzle. Reproduced from Cooper, S. F. *et al. Rev. Sci. Instrum.* **91** 013201 (2020), with the permission of AIP Publishing.

nozzle is shown in Fig. 4.6b. The model accurately reproduces the data assuming a Maxwellian velocity distribution with temperature of 6.5 K, whereas the temperature measured with the silicon diode is 5 K. We believe this discrepancy can be explained by heating from recombination as discussed in Chapter 2. Overall, the agreement between the data and model demonstrates that this nozzle design produces excellent beam thermalization. We also tried several variations of this basic design, and did not find significant variation in the results with modest changes in the bend angle or length of channel. This design is simple to manufacture, has relatively high conductance without sacrificing quality of thermalization, and therefore is an ideal choice for cryogenic atomic beam generation.

The time-of-flight data presented here provides a clear indication of the variability that arises from different cryogenic nozzle designs. Such data can be used as a first estimate of possible velocity dependent systematic effects in precision spectroscopy of hydrogen. Since atomic motion can both create systematic effects and complicate lineshape models, this study could have a

direct influence on experimental uncertainty in future hydrogen measurements. Our study of different nozzle geometries indicates that generating a well-thermalized cryogenic hydrogen beam is relatively straightforward as long as the pressure within the nozzle is low enough to be within the molecular flow regime, and with the requirement that the majority of the atomic trajectories contact a cryogenic surface before exiting the nozzle. This is precisely what the "angled" nozzle geometry accomplishes. The straight nozzle tested does not require that all atomic trajectories contact the nozzle surface and incomplete thermalization is seen in the data. In the case of the through-hole nozzle tested, we believe much of the on-axis flux of the beam is generated by collisions within the nozzle, which leads to the attenuation of low velocities.

4.3 Metastable atomic beam velocity characterization

For the measurements shown here, we use the apparatus design in Fig. 4.7 we operate the enhancement cavity at 6 W intracavity power. The atoms intersect the UV radiation at the beam waist of 150 µm and at an oblique angle of 5° so that the interaction length is ≈ 1.7 mm. The entrance to the CEM sits 290 mm after the atom-laser interaction region which in turn is 1130 mm after the chopper. The CEM operates in pulse counting mode which is AC coupled to the data acquisition electronics. Therefore, to generate the time-of-flight data, the signal is sent to a latch circuit to standardize the pulse height before being low-pass filtered to produce a pseudo-analog signal that can be averaged. A circuit diagram for the latch circuit is included in Fig. 4.8. The velocity distribution for the metastable atoms is expected to differ significantly from the ground state hydrogen velocity distribution due to the laser-atom excitation to the 2S state depending on the interaction time and atomic trajectory. For the 2S-8D measurement we performed in [8], the spectroscopy signal observed was the remaining atoms in the 2S state after resonantly quenching the 2S population through the short lived 8D state. Therefore, for systematic analyses, in situ characterization of the 2S velocity distribution is important.

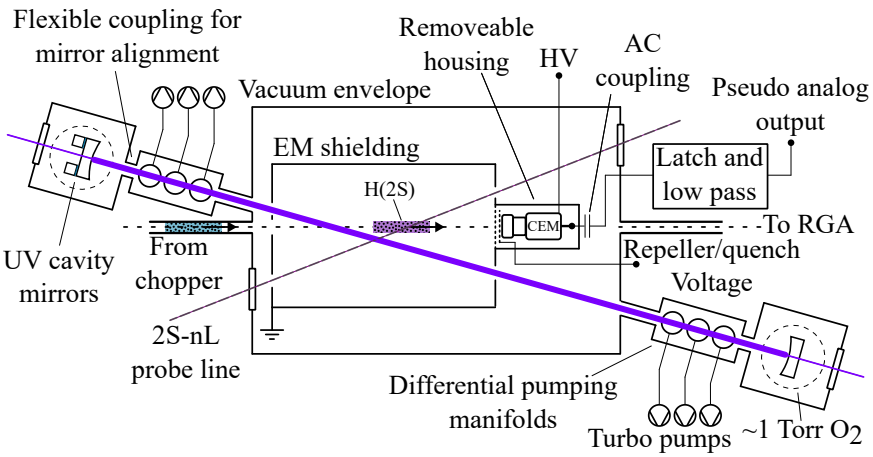

Figure 4.7: Spectroscopy chamber used to measure the time-of-flight of the metastable atomic hydrogen beam. The beam passes through a cavity enhanced UV beam to excite the 1S-2S transition. The metastable beam then travels into a channel electron multiplier (CEM) where metastables are quenched and Lyman-α (121 nm) photons are counted. A latch circuit standardizes the pulse heights, and the pulses are low passed to generate a psuedo-analog waveform. Reproduced from Cooper, S. F. *et al. Rev. Sci. Instrum.* **91** 013201 (2020), with the permission of AIP Publishing.

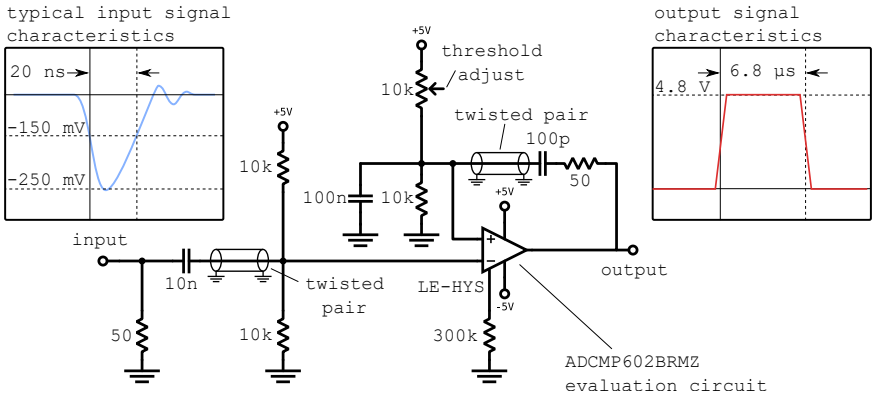

Figure 4.8: Electronic diagram of the latch circuit used for the metastable velocity distribution measurement based on a ADCMP602BRMZ evaluation module from Analog Devices. The comparator input is biased to 2.5 V by a voltage divider on the inverting input. A voltage divider held below 2.5 V by the threshold amount sets the pulse height which will trigger the latch circuit output to go high for the hold time. This threshold voltage is changed by adjusting the voltage divider at the non-inverting input of the comparator. The hold time is adjusted with the feed back loop capacitor, currently 100 pF. Once the heights and duration of each input pulse is standardized to the same shape output (4.8 V, 6.8 microsecond), the signal can be low-passed to form a pseudo-analog transformation of the pulse vs time density.

4.4 Metastable velocity analysis

Figure 4.9 shows TOF data of the metastable beam taken at three temperatures, 293 K, 10 K and 5 K (as measured with the silicon diode). As discussed earlier in the nozzle geometry analysis, the best choice for nozzle is the bent nozzle design as it most closely reproduces a pure Maxwellian.

As shown by the fits in Fig. 4.9a-4.9b, is apparent that the 2S velocity distribution deviates strongly from the ground state distributions shown earlier which follows a v^3 distribution. The metastable TOF signals at least have a v^4 prefactor in the distribution. However, reducing the power from $v^4 \rightarrow v^3$ and introducing an exponential factor with a cutoff velocity, v_{cut}, with a model described by

$$P(v) = \alpha v^3 e^{-\beta v^2} e^{-\frac{v_{cut}}{v}} \tag{4.6}$$

captures more of the velocity distribution behavior for the metastable beam as seen in Fig. 4.9b. This velocity distribution function was previously used in [112]. A comparison between these two velocity distributions that generate the 5-6 K data is shown in Fig. 4.10.

As is seen in by the velocity distributions, the data is shifted to higher velocities than a pure Maxwellian, and the best fits to the time-of-flight data have a prefactor of v^4 instead of the expected v^3. Further, there is additional loss of the slowest atoms on the tail of the 10 and 5 K data. Naively, one would expect the distributions to be shifted towards slower velocities due to the increased interaction time with the 243 nm radiation. However, this ignores ionization of the 2S state by the 243 nm radiation and the velocity dependence of the detector.

The velocity dependence of the CEM detector can easily be understood. As depicted in the previous chapter by Fig. 3.11, the input to the CEM detector has a grounded grid followed 1 mm later by a grid biased to ≈ -1 V. These grids serve to reduce the background by repelling stray photo-electrons present in the 1S-2S excitation chamber. The secondary purpose of the applied voltage, as described in section **??** also quenches metastables through mixing the 2S state with the 2P state which results in Lyman-α radiation which is detected by the CEM. The rate at which atoms are quenched depends on the time the atom spends in the DC field, and therefore slower atoms quench further away from the channeltron face and the collected solid angle for slower atoms is therefore smaller.

The metastable atom results indicate that the detected velocity distribution is affected by the laser interaction and method of detection, and the in situ velocity characterization performed here was useful for the precision measurement of the 2S-8D line performed afterward.

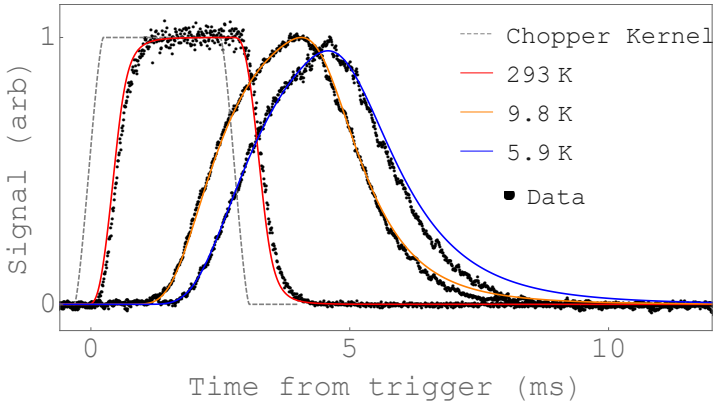

(a) v^4 model

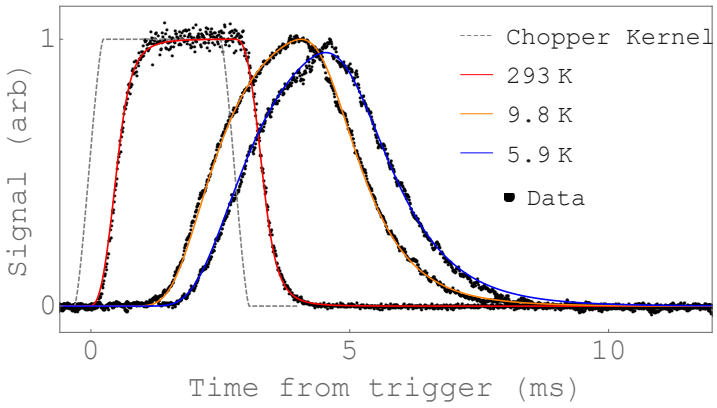

(b) $v^3 e^{-\frac{v_{cut}}{v}}$ model

Figure 4.9: Time-of-flight measurements of metastable atoms at 293 K, 10 K, and 5 K as measured by the silicon diode. (a) Data compared to a simple v^4 model fit which demonstrates that our excitation and detection methods have a large effect on the velocity distributions. The angled nozzle was used for this collection. For the comparison with the forward convolution model, slightly different temperatures were used as indicated in the figure. The v^4 model already deviates significantly from the v^3 in the neutral beam, and even does not capture perfectly the velocity distribution for the metastables directly. (b) Fit by the model in equation 4.6. With this velocity distribution it can be seen that a much better fit to the measured time of flight data is made.

Up to this point we have described the generation, detection, and velocity characterization of a beam of metastable 2S hydrogen atoms by optically exciting the 1S-2S two-photon transition with build up cavity enhanced 243 nm light [12]. A precision measurement of the 2S-8D interval was completed following the development of the beam where the measured velocity distribution is displayed in Fig. 4.10 was of importance. The second order Doppler shift and other residual velocity related systematic effects contribute uncertainty to this measurement, as for all of the

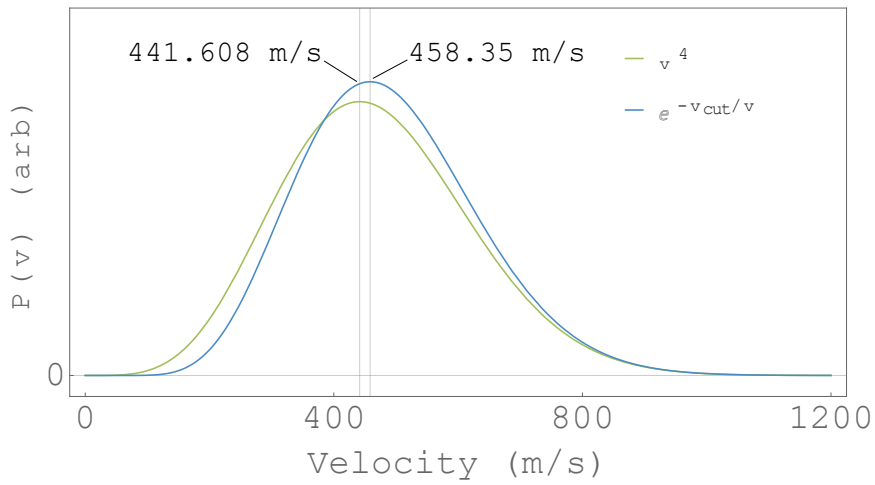

Figure 4.10: Velocity distributions for the TOF data in Fig. 4.9 at 5.9 K. The analytic function for the velocity distribution is not known at this time, however, the measured velocity distribution sets a constraint on the shape on which it can appear. Two best fit distributions are shown in the figure along with their fit parameters and respective errors. The difference between these two velocity distrbution's most probable velocities would contribute approximately 60 Hz of difference when accounting for the second order Doppler shift in [8] at 4.9 K.

precision hydrogen measurements. Future high precision measurements of hydrogen would benefit from slower samples of hydrogen. The possibility of trapping hydrogen samples will also likely benefit from optical control.

Chapter 5

Optical deceleration of atomic hydrogen

This chapter describes the experimental demonstration of metastable atomic hydrogen beam deceleration with an all-optical method using the optical dipole force. While the use of dipole forces [113–115] for deceleration have been demonstrated previously for other species, we have applied a novel technique by also decelerating the lattice to directly manipulate the motion of our atomic hydrogen beam. In this experiment, we achieved accelerations of order $1 \times 10^9\,\mathrm{m\,s^{-1}}$.

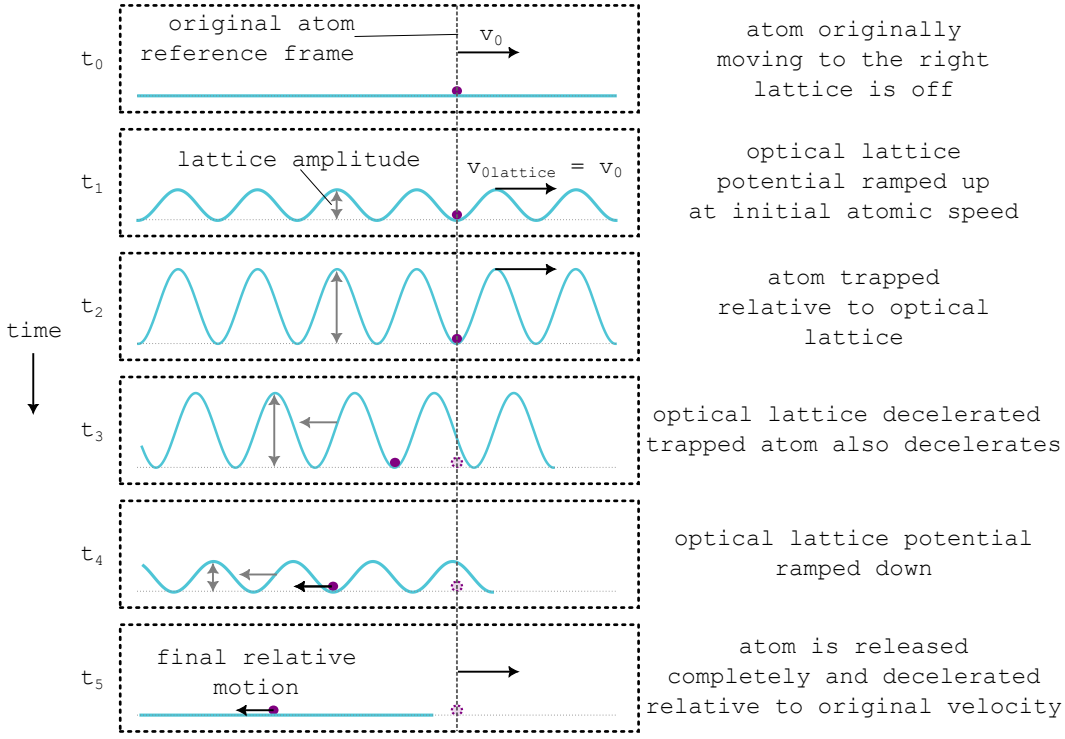

Figure 5.1: Concept of optical atomic hydrogen deceleration method. Initially at t_0, the metastable atom is traveling to the right at a speed v_0 and the optical lattice is initially off. At a later time, t_1, the moving lattice is turned on with an initial velocity $v_{0lattice} = v_0$. Once the lattice is fully on at t_2, the atom is trapped within one of the potential well minima. The lattice is then decelerated at t_3, causing the trapped atom to experience this deceleration. Once the deceleration is complete, the optical lattice is ramped off at t_4. Finally, the lattice is fully shut off and the atom is left with a reduced velocity with respect to the original reference frame. This method requires atoms to be first in the metastable atomic beam, which is described in earlier chapters.

The basic idea of our deceleration method, described in Fig. 5.1 uses an optical lattice originally moving at the speed of atoms in the metastable atomic beam which temporarily traps atoms within the optical lattice potential wells. The lattice is then decelerated causing atoms that are trapped in the lattice sites to be decelerated by a commensurate amount.

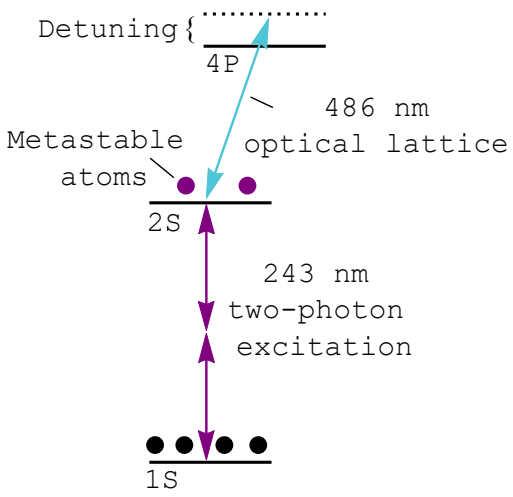

Figure 5.2: Relevant energy levels and wavelengths for deceleration scheme. As described in previous chapters, the metastable atomic beam is generated by excitation to the 2S state with a two-photon 243 nm transition where the 2S atoms have a lifetime of ≈122 ms. After 1S-2S excitation, the metastable beam intersects a moving optical lattice made of 486 nm light which is detuned near the 2S-4P resonance. Due to the spatially varying optical stark effect, 2S atoms will experience a force due to the 486 nm light. If the optical lattice motion is controlled (ie. by electro and acousto-optical modulators), the atom's motion will also be manipulated. A more detailed energy level diagram including fine and hyperfine structure is in Ch1, Fig. 1.7.

A motionally controllable optical lattice with sufficient trap depth is required to accomplish the proposed deceleration scheme. The first stage of this process was to determine the laser intensity requirements for the trap depths which was studied using a numerical model and Monte Carlo (MC) simulations. The optical addressing scheme we used is described in Fig. 5.2 where we use a 486 nm lattice beam detuned from the 2S-4P transition to generate the decelerating potential. Simulations allowed us to verify the required laser power and focus sizes, as well as frequency detunings required to successfully apply sufficient optical forces without significant spontaneous emission losses the 2S atoms.

This chapter covers the deceleration experiment and simulations. Included in the following sections of this chapter are the basics for modeling this interaction and simulation of the atomic trajectories in the time varying optical potential as well as the experimental construction of the experimental apparatus used to demonstrate the slowing.

5.1 Decelerator model

5.1.1 An intuitive picture for the optical dipole force

A neutral atom experiences the optical dipole force (ODF) under illumination of an optical radiation field as a consequence of the electric polarizability of the atom. To first develop an intuitive picture we can relate the superposition an atom's wavefunctions to the motion of classical spatial charge distributions. A classical charge distribution made up of polarizable bound charge with initial net zero dipole moment, $\vec{p}_0 = 0$, will respond to an applied oscillating electric field

$$\vec{E}(\vec{r},t) = \hat{\varepsilon} E_0(\vec{r}) \cos(\omega_l t), \tag{5.1}$$

with the charges separating along the $\hat{\varepsilon}$ direction – inducing a dipole moment in the system, $\vec{p}$. The magnitude of $\vec{p}$ depends on system's polarizability, which in essence is how tightly or loosely bound the charges are. For an interesting approache to the estimation of the polarizability of a classically modeled hydrogen charge distribution, see [116]. Since the induced dipole is subjected to an external electric field there will be a resulting interaction energy due to the potential established by the electric field interacting with the induced electric dipole, $V(\vec{r},t) = -\vec{p} \cdot \vec{E}(\vec{r},t)$. Should the strength of the electric field that is applied vary spatially, $V = f(\vec{r})$, it will lead to a force, $\vec{F} = -\nabla V$, which will accelerate the charge distribution's center of mass towards the lowest interaction potential.

Quantum mechanically, an atom in a perturbing electric field will become a superposition of individual electronic wavefunctions which are spread out over spatial coordinates. The wave functions themselves do not move, unlike a classical charge distribution, which can undergo a continu-

ous redistribution of charge. However, because the atom can exist as a simultaneous superposition of more than one wavefunction with time dependent relative phases, the motion of charge occurs in the redistribution of the probability distribution. For example, radiation tuned near a transition between ground and excited states, $|g\rangle$ and $|e\rangle$ respectively, will cause the atom to be in a superposition

$$|\psi\rangle = a|g\rangle + be^{i\phi(t)}|e\rangle, \tag{5.2}$$

which will have a relative phase evolving in time, $\phi(t)$, related to the transition energy spacing and laser detuning. For now, ϕ is simply phase which will evolve in time and the amplitudes a and b are just required for proper normalization. The electrons spatial probability distribution, $P(\vec{r}) = \langle\psi|\psi\rangle$, is not stationary and will evolve with time redistributing the electron probability as shown in Fig. 5.3. A dipole moment is generated in the atom due to the displacement of electron

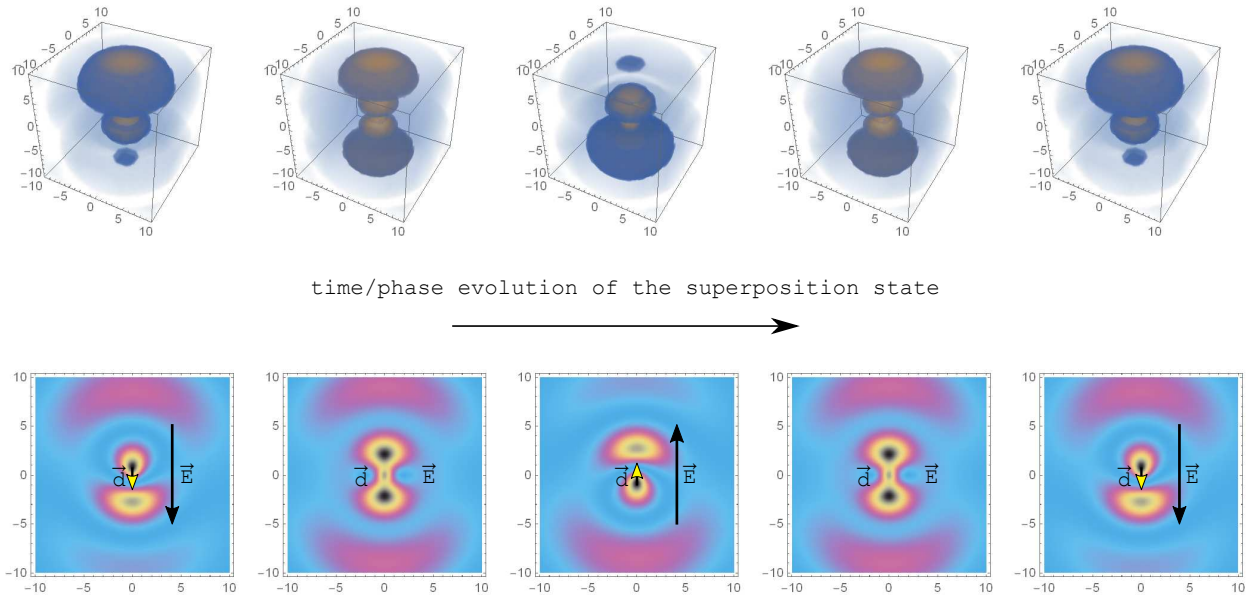

Figure 5.3: The phase evolution of $\langle\psi|\psi\rangle$ in an oscillating electric field. Black is the greatest electron probability, and blue is the lowest. Therefore, the dipole moment of the atom will point away from the highest electron density.

probability asymmetric about the origin, which is indicated by the arrows labeled $\vec{d}$ in Fig. 5.3.

The induced dipole moment once again can interact with the local electric field, and if the field is spatially varying, the atom will experience a force on its center of mass.

5.1.2 The Rabi problem: ac Stark shift of the two level atom

To quantitatively determine the magnitude and direction of the force described above, I will give an outline of the ac Stark shift problem for a two level atom in a classical electric field going along with the very helpful treatment of this problem found in [117]. Since this problem and its nuances are found in many sources and textbooks and other literature, I will keep the discussion brief.

When light interacts with the atom in the way discussed previously, the system's general wavefunctions would then be the sum of a complete set of basis states,

$$\psi = \sum_{k=1}^{\infty} c_k \left|\phi_k\right\rangle \tag{5.3}$$

where the c_k are amplitudes to the eigen functions $\left|\phi_k\right\rangle$ of the total Hamiltonian H, and obey the Schrödinger equation. The total Hamiltonian, will be the combination of the bare atomic Hamiltonian, H_0 and the dipole interaction Hamiltonian as

$$H(t) = H_0 + H'(t), \tag{5.4}$$

where the Hamiltonian of a dipole interacting with an oscillating electric field is defined as

$$H'(t) = -\vec{d}\cdot\vec{E}(t). \tag{5.5}$$

In eq. 5.5, $\vec{d}$, is the atomic dipole which is assumed to be interacting with a classical electric field, $\vec{E}(t) = \hat{\varepsilon}E_0\cos(\omega_l t)$ oscillating at ω_l (a good approximation for the coherent high intensity optical lattice of this experiment). If we assume the wavefunction is composed only of two levels ($\sum_k \left|\phi_k\right\rangle \rightarrow \left|g\right\rangle + \left|e\right\rangle$ and $\psi = c_g\left|g\right\rangle + c_e\left|e\right\rangle$), then we may take the ground and excited states with

energies of 0 and $\hbar\omega_0$ respectively. The Hamiltonian can then be written as

$$H_0 + H'(t) = \begin{pmatrix} 0 & 0 \\ 0 & \hbar\omega_0 \end{pmatrix} + \begin{pmatrix} 0 & \frac{\hbar\Omega}{2} e^{i\omega_l t} \\ \frac{\hbar\Omega}{2} e^{-i\omega_l t} & 0 \end{pmatrix}, \tag{5.6}$$

Where the Rabi frequency, Ω, has been introduced and is defined by

$$\Omega \equiv -\frac{eE_0}{\hbar} \langle e|\vec{r}|g\rangle . \tag{5.7}$$

In general, the $\langle e|\vec{r}|g\rangle$, or dipole matrix elements are not easily calculated and tend to be measured in many systems. For Hydrogen, however, the electronic wavefunctions are analytically known and solved for in many introductory quantum mechanics texts, and therefore we have the ability to easily calculate any of these.

In the steps between eq. 5.5 and eq. 5.7 there are a few implicit assumptions or approximations being made. First, of course is that the laser field is a plane wave oscillating field with a frequency nearly resonant with the atomic resonance allowing us to accurately treat the problem as only a two atomic level system. We define a detuning

$$\delta \equiv \omega_l - \omega_0, \tag{5.8}$$

such that δ is positive when $\omega_l > \omega_0$, or in other words when the laser is blue detuned. Secondly, moving away from the dipole interaction operator in eq. 5.5, the dipole approximation is applied, which assumes that the laser wavelength has negligible variation across the spatial extent of the atom. This is in essence assuming that the atom is a point dipole, which is usually a good assumption since optical wavelengths are on the order of a few hundred nanometers, and the Bohr radius is of order 0.5 Å. Also, we achieved the complex exponentials in the matrix by applying the rotating wave approximation (RWA) keeping the slowly oscillating terms and throwing away terms which would oscillate of order $2\omega_l$. As noted in sec. 5.1.2 of [117], it is good to point out that both the RWA and the two-level atom approximation are of the same level of accuracy as they are

essentially approximating away fast evolving effects from far detuned components of the atomic and laser interaction.

The next step to getting rid of the explicit time dependence in eq. 5.6 is to observe the interaction from a reference frame that rotates along with the phase evolution of the laser at a frequency ω_l. We do this by redefining the coefficients which describe the amplitudes, c_k, containing a relative phase that rotates at the rate of the laser by

$$\tilde{c}_e = c_e e^{i\omega_l t}. \tag{5.9}$$

This causes the Hamiltonian to be transformed from H to $\tilde{H}$ in a convenient way, removing the explicit time dependence from eq. 5.6 so that

$$\tilde{H} = \tilde{H}_0 + \tilde{H}' = \begin{pmatrix} 0 & 0 \\ 0 & -\hbar\delta \end{pmatrix} + \begin{pmatrix} 0 & \frac{\hbar\Omega}{2} \\ \frac{\hbar\Omega}{2} & 0 \end{pmatrix}. \tag{5.10}$$

Equation 5.10 is now simple to diagonalize, which gives us the energy eigenvalues

$$E_\pm = -\frac{\hbar\delta}{2} \pm \frac{\hbar\Omega'}{2}, \tag{5.11}$$

where the generalized Rabi frequency is introduced and defined by $\Omega' \equiv \sqrt{|\Omega|^2+\delta^2}$. The eigenstates that are paired with the eigenenergies in eq. 5.11 are

$$\begin{aligned} |\phi_+\rangle &= \sin(\theta)\,|g\rangle + \cos(\theta)\,|e\rangle\,, \\ |\phi_-\rangle &= \cos(\theta)\,|g\rangle - \sin(\theta)\,|e\rangle\,, \end{aligned} \tag{5.12}$$

where θ is called the Stückelberg angle and defined by

$$\cos(2\theta) = -\frac{\delta}{\Omega'}. \tag{5.13}$$

The eigenstates in eq. 5.12 are commonly referred to as the "dressed states" where they are a basis for the two level atom "dressed" in the laser light of the interaction which show that the effect of the light is to generate new states composed as a mixture of the bare Hamiltonian states with a mixing strength given by the Stückelberg angle, or a ratio of the laser intensity (wrapped up in Ω) and the detuning, δ. Though this is a diversion from the topic of calculating the force due to the ac Stark shift, it relates back to the previous section. We see here that the dressed states are superpositions of the ground and excited states which the laser couples together when near a resonance. We know that both $|g\rangle$ and $|e\rangle$ will individually follow the time evolution governed by the Schrödinger equation so that there is a relative phase between the two. This gives justification to the statements made in Sec. 5.1.1 and the superposition wavefunction image supported by eq. 5.2.

We can also see now by looking at the eigenenergies in eq. 5.11 that the atomic energy levels experience a shift due to the laser light mixing the two states. This is called the ac Stark shift which is an important systematic effect to characterize and or extrapolate out of spectroscopic data such as was done in [8]. Figure 5.4 shows a plot of $E_{\pm}$ as a function of detuning.

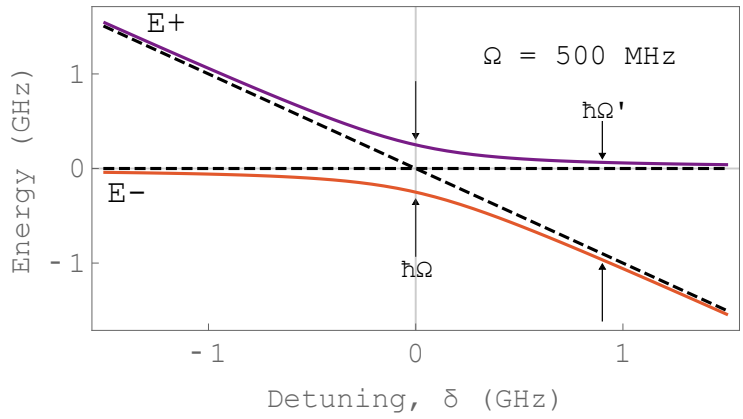

Figure 5.4: Plot of the dressed states energies as the detuning is swept from -1.5 GHz to 1.5 GHz showing the avoided level crossing at $\delta = 0$.

Returning to the purpose of this section however, we'll remember that the energy shifts plotted as a function of detuning is less important than thinking about the level shift as a function of Ω

which contains the laser intensity. To begin, we can solve for the ground and excited states in terms of $|\phi_{\pm}\rangle$ which gives

$$\begin{aligned} |g\rangle &= \sin(\theta)\,|\phi_{+}\rangle + \cos(\theta)\,|\phi_{-}\rangle\,, \\ |e\rangle &= \cos(\theta)\,|\phi_{+}\rangle - \sin(\theta)\,|\phi_{-}\rangle\,, \end{aligned} \tag{5.14}$$

allowing us to associate the $|g\rangle \approx |\phi_{-}\rangle$ for large red detunings ($\theta \to 0$ for $\delta < 0$ and $\delta >> \Omega$), whereas $|g\rangle \approx |\phi_{+}\rangle$ for large blue detunings ($\theta \to \pi/2$ for $\delta > 0$ and $\delta >> \Omega$), and the excited state mostly becomes associate to the opposite dressed state. In the case of large detunings, meaning $\delta >> \Omega$, we can Taylor expand the generalized Rabi frequency giving

$$\Omega' = \sqrt{|\Omega|^2+\delta^2} \approx \left(1 + \frac{|\Omega|^2}{4\delta}\right). \tag{5.15}$$

Now if we look at plugging eq. 5.15 into eq. 5.11

$$\begin{aligned} \Delta E_{+} &= \frac{\hbar\Omega^2}{4\delta} \\ \Delta E_{-} &= -\frac{\hbar\Omega^2}{4\delta}, \end{aligned} \tag{5.16}$$

we notice that $E_{\pm}$ has the opposite dependence on the sign of the detuning δ. Explicitly, since Ω is proportional to laser intensity, we see that large **red** detunings lead to **high** Ω i.e. **high intensity seeking** ground state atoms, whereas a large **blue** detuning leads to **low** Ω i.e. **low intensity seeking** ground state atoms. Figure 5.5 shows the energy shift (eq. 5.11) due to this effect on a ground state atom mapped over both a gaussian laser beam, and a $\cos(kz)$ lattice profile.

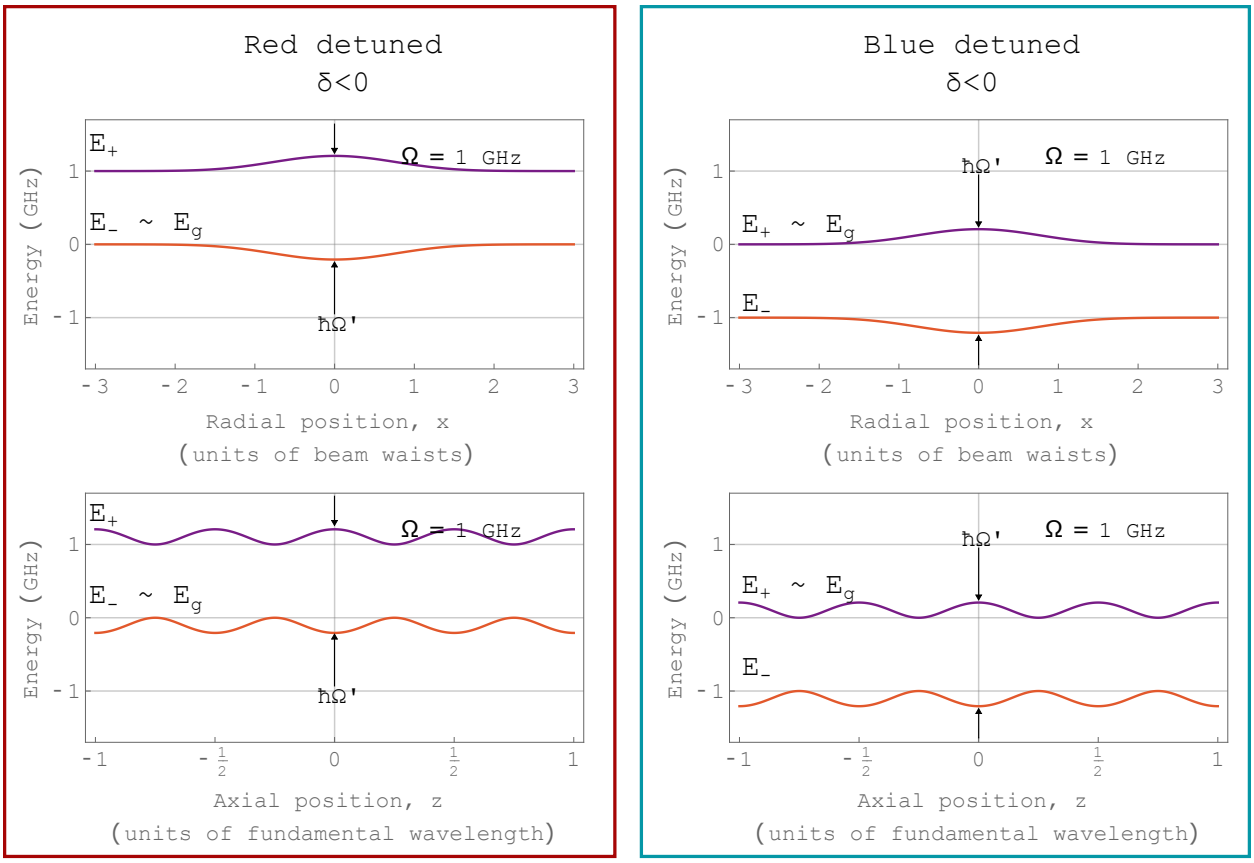

Figure 5.5: Plots of eq. 5.11 mapped over a gaussian beam waist and a $\cos(kz)$ lattice profile. One thing to make note of is that $|g\rangle$ is a superposition of $|\pm\rangle$ depending on the detuning and so the force on a ground state prepared atom flips sign with the sign of the detuning. The excited state is doing the opposite of the ground state.

So far we have covered the mechanical force exerted on a two level atom in a classical electric field. This can be expanded to include more atomic resonances. In our experiment the "ground" state $|g\rangle$ is actually the metastable $|2S\rangle$ state, and the excited state is chosen to be the $|4P\rangle$ manifold which contains some fine and hyperfine structure. The lifetime of the $|4P\rangle$ state is very short ($\tau \approx 15$ ns) so it is obviously a problem for the deceleration if the atoms spend much overlap with the $|4P\rangle$ excited state as it will decay to the $|1S\rangle$ state with a Lyman-α photon emission. Depending on the intensities and detunings the off resonant excitation to the $|4P\rangle$ state may become non-negligible. Therefore, the upper state population needs to be understood as well. This will be taken into account in a later section. First, we'll briefly cover the force treatment with fine and hyperfine structure taken into account. From this point forward, the method does differ significantly

though the expressions get messier and the process requires more book keeping which we do in the computer software Mathematica, and I will omit many of the the steps from this chapter.

The Hamiltonian we'll consider now will include fine and hyperfine structure of the $|2S\rangle$ and $|4P\rangle$ states, however, we will drop the $|2S, F=0\rangle$ level in our analysis because the two-photon excitation selectively populates only the $F=1$ states. The $|2P\rangle$ levels are obviously left out as they are far off the 1S-2S resonance, have very short lifetimes, and more importantly are two-photon dipole forbidden. To start, we will compare the Stark shift for each of the three $|2S, m_F\rangle$ levels and we will assume linearly polarized light which limits the transitions to $\Delta m_F = 0$. This means in total each of the $|2S, F=1\rangle$ magnetic sublevels will have a dipole matrix element with each $|4P, F\rangle$ sublevel of the same m_F. In other words, each $|2S\rangle$ sublevel (for which there are three: $m_F = -1, 0, 1$) will have four possible transitions to the $|4P_{1/2}, F=0,1\rangle$, and $|4P_{3/2}, F=1,2\rangle$. This makes in total a set of three 5×5 matrices. If we approximate the hyperfine splitting, $\mathcal{O}(1\,\text{GHz})$, to be negligible between the $|4P, F\rangle$ states which is a good approximation should earlier approximations hold, then we can write out a Hamiltonian matrix

$$\tilde{H} = \tilde{H}_0 + \tilde{H}' = \begin{pmatrix} 0 & 0 & 0 & 0 & 0 \\ 0 & -\hbar\delta_{1/2} & 0 & 0 & 0 \\ 0 & 0 & -\hbar\delta_{1/2} & 0 & 0 \\ 0 & 0 & 0 & -\hbar\delta_{3/2} & 0 \\ 0 & 0 & 0 & 0 & -\hbar\delta_{3/2} \end{pmatrix} + \frac{\hbar}{2}\begin{pmatrix} 0 & \Omega_{10} & \Omega_{11} & \Omega_{21} & \Omega_{22} \\ \Omega_{10} & 0 & 0 & 0 & 0 \\ \Omega_{11} & 0 & 0 & 0 & 0 \\ \Omega_{21} & 0 & 0 & 0 & 0 \\ \Omega_{22} & 0 & 0 & 0 & 0 \end{pmatrix}, \tag{5.17}$$

where the detunings, δ_J, are defined by their respective $|4P_J\rangle$ level, where positive detunings are blue detuned above the $|4P_{3/2}\rangle$ level, and there is only a constant offset of the $|4P\rangle$ fine structure splitting between the detunings ($\omega_{FSS} = 2\pi 1.371\,\text{GHz}$). We will define $\delta \equiv \delta_{3/2}$ and $\delta_{1/2} \equiv \delta + \omega_{FSS}$. The Ω's in eq. 5.17 are defined by $\Omega_{J-1/2,F}$ couplings to whichever 2S magnetic sublevel is being calculated for. We perform the diagonalization of eq. 5.17 for the ac Stark shift of each $|2S, m_F\rangle$ sublevel and find that the shift is the same for each as expected (though many of the Rabi frequencies are different). Since the Stark shifts are the same we may choose any of of the 2S

levels which is allowed as we assume the 1S-2S excitation is done with linearly polarized light and each of the $|2S, F = 1, m_F\rangle$ levels is equally populated.

The ac Stark shift of the 2S state which depends on the laser intensity and detuning can be found analytically using Mathematica to diagonalize this matrix. We use the eigenvalue which corresponds to the correct ac Stark shift and we fit the analytic shift found in Mathematica with the physically motivated expression

$$V = \frac{\hbar}{2}\left[c_1(-(\delta+\omega_{FSS})+\Omega'_{1/2})+c_2(-\delta+\Omega'_{3/2})\right], \tag{5.18}$$

where the factors $\Omega'_{1/2} = \sqrt{(\delta+\omega_{FSS})^2+\Omega_{1/2}^2}$ and $\Omega'_{3/2} = \sqrt{\delta^2+\Omega_{3/2}^2}$ are generalized Rabi frequencies for the 2S-4P$_{1/2}$ and 2S-4P$_{3/2}$ dipole interactions respectively, each of which depend on the laser detuning and intensity. The fit coefficients, c_i, in eq. 5.18 describe the relative contributions to the 2S lattice potential due to the resolved 4P$_J$ fine structure. Moving to a simpler function to represent the dipole potential on the atom speeds up the computation time without significant loss of accuracy. The total RMS relative error between the diagonalized analytic output and the fit function sampled over electric fields of $0-0.3\,\mathrm{MV\,m^{-1}}$ and detunings of $0-30\,\mathrm{GHz}$ is approximately 0.5%. Looking at eq. 5.18 we can roughly see that while taking into account more detailed atomic structure, the potential the atom sees is still

$$V(r,z,t) \propto \Omega(r,z,t) \propto E_0(r,z,t) \propto \sqrt{I(r,z,t)}. \tag{5.19}$$

The Rabi frequency in terms of laser intensity is given by

$$\Omega_{eg}(r,z,t) = \frac{e}{\hbar}\langle e|\vec{r}|g\rangle\sqrt{\frac{2}{c\varepsilon_0}I(r,z,t)}, \tag{5.20}$$

where $\langle e|\vec{r}|g\rangle$ is in units of distance (of order, a_0, the Bohr radius), e the elementary charge, and the $2/c\varepsilon_0$ factor is to convert the expression to be in terms of intensity units. This now gives us the opportunity to calculate the mechanical force through the potential given a spatially and time

varying intensity $I(r,z,t)$. Filling in this part of the Rabi frequency is discussed in section 5.1.4. Moving forwared from here we are implicitly assuming the adiabatic approximate, which states that the atomic phase is adiabatically in equilibrium instantly for all of the changes in the potential. This allows us to generate classical atomic trajectories in the dipole potential we calculated in this section.

5.1.3 Off resonant coupling of 2S to 4P transition and spontaneous emission

As was previously mentioned, the $|4\mathrm{P}\rangle$ state is very short lived leading to an issue of accidental quenching of the metastable atoms through spontaneous emission by off-resonant excitation. In this section we seek to quantify the expected losses so that this can be programmed into a numerical Monte Carlo simulation. As we found in the previous analysis, the stark shift is equal for each of the three $|2\mathrm{S}, m_F = -1,0,1\rangle$ states. Therefore, the 2S-4P excitation is the same for all three. We can conveniently choose to compute the equations of motion for the state populations of just $|2\mathrm{S}, m_F = 0\rangle$ which happens to have only two nonzero Rabi frequencies, so that 3×3 matrices may be used instead of 5×5. The choice of the three states used here are

$$
\begin{aligned}
|g\rangle = |2\mathrm{S}, m_F = 0\rangle &= \begin{pmatrix} 1 \\ 0 \\ 0 \end{pmatrix} \\
|1\rangle = |4\mathrm{P}, F = 1, m_F = 0\rangle &= \begin{pmatrix} 0 \\ 1 \\ 0 \end{pmatrix} \\
|2\rangle = |4\mathrm{P}, F = 2, m_F = 2\rangle &= \begin{pmatrix} 0 \\ 0 \\ 1 \end{pmatrix}.
\end{aligned}
\tag{5.21}
$$

Since spontaneous emission cannot be included into the Hamiltonian treatments already introduced, we must find the equations of motion of the atomic level populations by solving the Lindblad Master Equation

$$i\hbar\partial_t\rho = [H,\rho] + \mathscr{L}(\rho) \tag{5.22}$$

where we've introduced the density matrix whose elements are constructed in terms of the wavefunction probability amplitudes by $\rho_{jk} = c_j c_k^*$ as

$$\rho = \begin{pmatrix} \rho_{gg} & \rho_{g1} & \rho_{g2} \\ \rho_{1g} & \rho_{11} & \rho_{12} \\ \rho_{2g} & \rho_{21} & \rho_{22} \end{pmatrix}, \tag{5.23}$$

and the Hamiltonian is given by

$$H = \begin{pmatrix} 0 & 0 & 0 \\ 0 & -\hbar\delta_{1/2} & 0 \\ 0 & 0 & -\hbar\delta_{3/2} \end{pmatrix} + \frac{\hbar}{2}\begin{pmatrix} 0 & \Omega_{10} & \Omega_{22} \\ \Omega_{10} & 0 & 0 \\ \Omega_{22} & 0 & 0 \end{pmatrix}. \tag{5.24}$$

The second term in eq. 5.22 is called the Lindblad superoperator, $\mathscr{L}(\rho)$, which allows the accounting of spontaneous emission and is defined as [118]

$$\mathscr{L}(\rho) = \sum_m \left(C_m \rho C_m^\dagger - \frac{1}{2}\left\{ C_m^\dagger C_m, \rho \right\} \right), \tag{5.25}$$

where $C_m = \sqrt{\gamma_m}|f\rangle\langle m|$. Since there are only two decay channels, $|1\rangle \to |g\rangle$ and $|2\rangle \to |g\rangle$, we may easily sum over $m = 1,2$ giving the C_m matricies as

$$C_1 = \begin{pmatrix} 0 & \sqrt{\gamma} & 0 \\ 0 & 0 & 0 \\ 0 & 0 & 0 \end{pmatrix}, \qquad C_2 = \begin{pmatrix} 0 & 0 & \sqrt{\gamma} \\ 0 & 0 & 0 \\ 0 & 0 & 0 \end{pmatrix}. \tag{5.26}$$

from eq. 5.25, we find that the Lindbladian is

$$\mathscr{L}(\rho) = \begin{pmatrix} \frac{\gamma}{2}(\rho_{11}+\rho_{22}) & -\frac{\gamma}{2}\rho_{g1} & \frac{\gamma}{2}\rho_{g2} \\ \frac{\gamma}{2}\rho_{1g} & -\gamma\rho_{11} & -\gamma\rho_{12} \\ \frac{\gamma}{2}\rho_{2g} & -\gamma\rho_{21} & -\gamma\rho_{22} \end{pmatrix}. \tag{5.27}$$

Inserting eq. 5.27 back into eq. 5.22 gives us 9 coupled differential equations for the elements of the density matrix. We also must impose the physical constraint that $\rho_{gg}+\rho_{11}+\rho_{22}=1$ which is to say that the population is conserved over the course of the interaction. In general this could be difficult to solve, but we will make a significant simplification of these differential equations by assuming that the system is in static equilibrium at each time step (therefore setting the left hand side derivatives all to zero). This is a good approximation since the rate at which the population dynamics will stabilize is on the order of $1/\Omega'$ which for a far detuned lattice is very quick compared to our motional dynamics. Since the decay rate from the $|4\mathrm{P}\rangle$ is very rapid, and we approximate the excitation to be in steady-state, we assume the most pessimistic loss metric which is that any fraction of the metastable atoms excited to $|4\mathrm{P}\rangle$ are completely lost to spontaneous emission. In other words, the probability an atom will be lost is the product of the decay rate, the duration of excitation, and the probability the atom is in any of the excited $|4\mathrm{P}\rangle$ states, and determine that the overall loss of the metastable atoms is

$$P_{lost} = \Delta t\,\gamma_{4P}\,(\rho_{11}+\rho_{22}) = \Delta t\,\gamma_{4P}\left(1-\rho_{gg}\right). \tag{5.28}$$

5.1.4 Time varying laser intensity

The standing wave laser intensity can be expressed as

$$I(r,z,t) = I_0\left(1+R+2\sqrt{R}\cos\left(\Phi(z,t)\right)\right)e^{-(r/w_0)^2}. \tag{5.29}$$

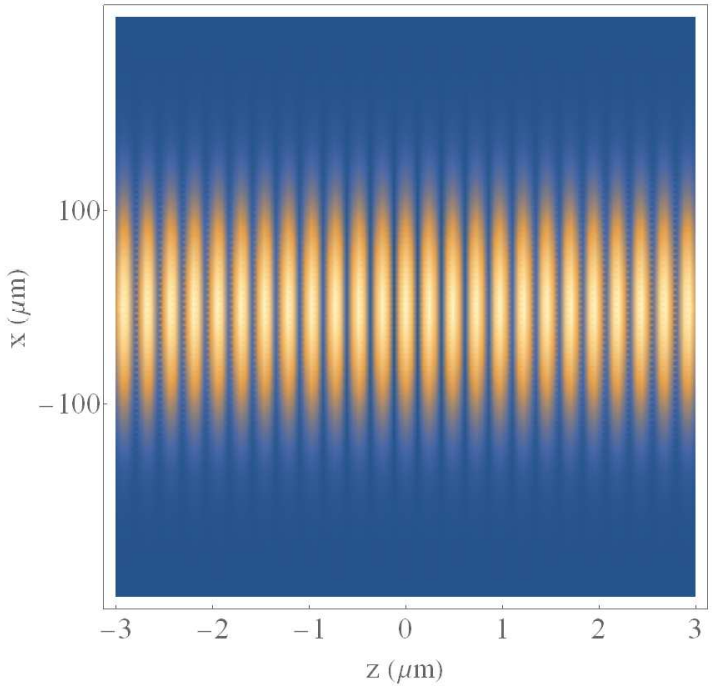

Figure 5.6: Intensity map of a standing wave laser (assuming no spatial divergence in this case). A blue detuned laser will caus atoms to be pushed toward the blue regions. Notice the spatial scales are very different in the z and x directions. Although it appears that atoms will quickly traverse along the x direction out of regions of optical dipole force, in actuality the atoms will oscillate back and forth in the z direction many times before they have the opportunity to traverse the same distance in the x direction.

In this case, the divergence along the z direction of the beam has been neglected and I_0 is the forward going laser intensity but can be easily included by changing w_0 to a z-dependent $w(z)$ radial beam wast factor in the exponential. The wave has the phase

$$\Phi(z,t) = 2kz - \omega_\Delta t + \Phi_c \cos(2\pi f_c t), \tag{5.30}$$

where ω_Δ is the DC frequency difference of the forward and backward going beams, and ϕ_c and f_c are an applied phase modulation to the backward going beam which leads to an additional frequency chirp on the order $\approx f_c \phi_c$. Figure 5.6 shows the axial and radial spread of the standing wave intensity profile

The generation of these signals is accomplished with an AOM and EOM respectively and will be described later in the text. The contrast ratio of the standing wave fringes is degraded by any

power imbalance in the forward and back going beams, however, even a 50% power imbalance will still lead to a contrast ratio of $2.8 : 0.08$. This is contained in the power imbalance factor, R, which has to be considered since the standing wave is generated by retroreflecting through a double passed AOM and EOM which have non-negligible optical loss. The final exponential factor is the transverse intensity profile due to the Gaussian beam envelope of the standing wave ignoring beam divergence ($w(z) = w_0 = \text{const.}$).

For atoms initially travelling at a speed near the of the lattice speed, they will be trapped in the wells generated by the nodes or antinodes, up to a capture range determined by the interference contrast ratio, laser intensity, and detuning. As depicted in Fig. 5.7, the capture velocity range, $\Delta v_T(R, \delta, I_0)$, of the lattice can be determined from the peak to trough potential giving,

$$\Delta v_T(R, \delta, I_0) = \frac{a_0 e \beta_{ge}}{\hbar} \sqrt{\frac{4\hbar}{m_e c \varepsilon_0}} \sqrt{\frac{1}{2} \frac{\sqrt{R} I_0}{\delta}}. \tag{5.31}$$

The factor of $1/2$ in front of I_0 is to compensate for the radial dependence of intensity. For a reasonable 486 nm laser beam with minimum waist of 100 µm and 500 mW forward power, double passed power efficiency of $R = 0.7$, and a detuning of 1.5 GHz, the trap depth is approximately $15\,\mathrm{m\,s^{-1}}$. These estimates are conservative as significantly greater trap depths are achievable with more laser power (we show over 4 W CW in [10]). As shown in Fig. 5.7, the most probable velocity of our metastable H2S beam resides right below $500\,\mathrm{m\,s^{-1}}$ which leads to about 9 percent of the metastable flux that may be captured and slowed. At the velocity range that we can address with our acousto optical modulator near $300\,\mathrm{m\,s^{-1}}$ there is about 4 percent.

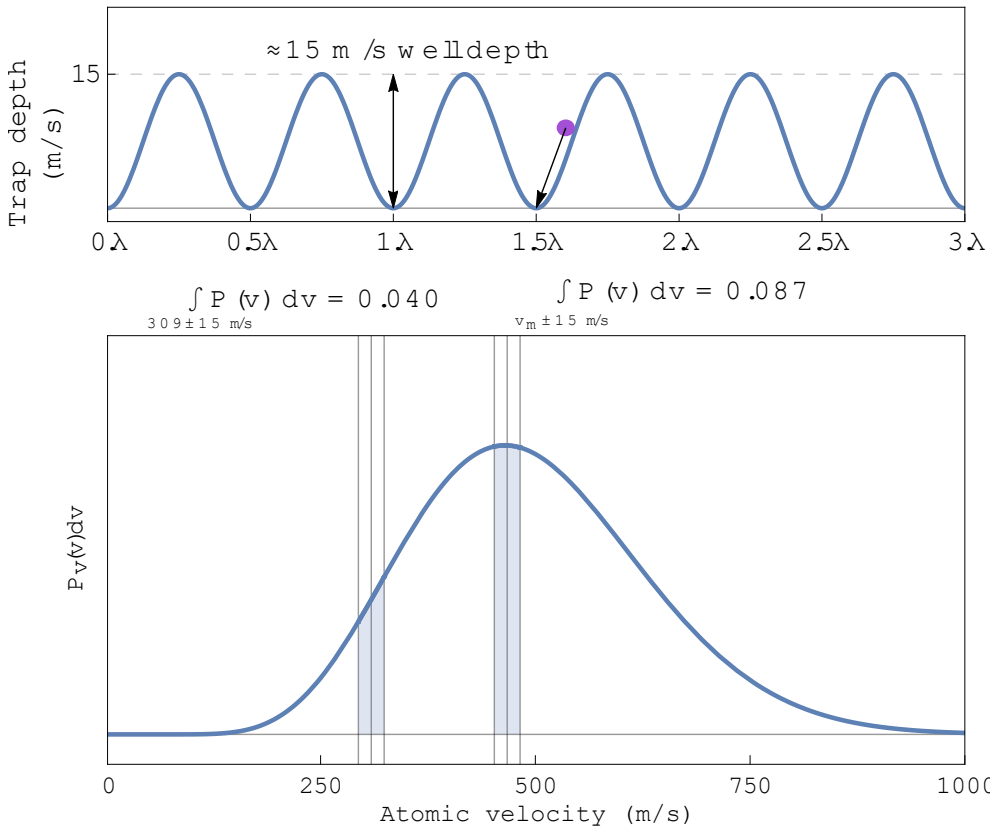

Figure 5.7: A 1-D cartoon along the laser axis of the optical lattice potential wells. For a reasonable beam size, available power at 486 nm and detuning, the lattice would have $\approx$15 m s^{-1} deep wells. The $\pm$15 m s^{-1} range around the most probable velocity, v_m in the atomic flux velocity distribution that was measured for our $\approx$5 K metastable H2S beam of hydrogen in [12] contains approximately 9 percent of the available metastable flux. At the velocity range that we can address with our acousto optical modulator near 300 m s^{-1}, there is about 4 percent.

The speed of the lattice can be calculated by determining the phase velocity of the standing wave profile,

$$v_P(t) = \frac{\omega(t)}{k(z)} = \frac{\partial_t \Phi(z,t)}{\partial_z \Phi(z,t)} = \frac{1}{2}(\lambda f_\Delta + \lambda f_c \Phi_c \cos(2\pi f_c t) \tag{5.32}$$

Which can be rewritten conveniently in terms of velocities as,

$$v_P(t) = v_l - v_c \sin(2\pi f_c t) \tag{5.33}$$

Where we've introduced the central lattice velocity $v_l = 1/2\lambda f_\Delta$ and the chirped velocity range $v_c = 1/2\lambda f_c \phi_c$. As shown by the measured lattice velocities in Fig. 5.9, the standing wave will accelerate from a peak velocity of $v_l + v_c$, and finish at a minimum velocity of $v_l - v_c$. Atoms within the capture range of the potential wells will be required to also decelerate following the lattice speeds, from $v_i \approx v_l + v_c \rightarrow v_f \approx v_l - v_c$ as long as the lattice is shut off in during the times where it must accelerate back to $v_l + v_c$. Experimentally, this can easily be accomplished by shuttering off the lattice beams with a Pockels cell before the laser-atom interaction region. A measured set of optical pulses is also shown in Fig. 5.9 and Fig. 5.10.

The explicit spatial and temporal dependence of the optical trap potential is contained in the intensity dependence of the Rabi frequencies of Eqn. 5.18. Our control of the modulated lattice is generated by three electro-optical components. We model the lattice intensity, I, as

$$I(\vec{r},t) = I_0(1+\eta^2+2\eta\cos(\Phi(z,t)))e^{-(r/w_0)^2}e^{-((t-t_0)/t_w)^6}, \tag{5.34}$$

where I_0 is the measured peak laser intensity, Φ is the axial phase of the standing wave interference pattern, and η^2 is the ratio of the forward going and backward going power for the retroreflected double-passed 486 nm beam. The gaussian beam factor has width of w_0, and the temporal shutter function is described by the super-gaussian centered at t_0 and having a duration of t_w. We neglect beam divergence since the Rayleigh range of our interaction region is greater than the atomic beam distribution. The contrast ratio of the standing wave fringes is degraded by any power imbalance in the forward and back going beams which needs to be considered since the standing wave is generated by retroreflecting a double passed AOM and EOM, each having non-negligible optical loss.

The phase in Eqn. 5.34 is

$$\Phi(z,t) = 2kz - \omega_\Delta t + \Phi_c \cos(2\pi f_c t), \tag{5.35}$$

where ω_Δ is the center AOM-set frequency difference of the forward and backward going beams, and Φ_c and f_c are an applied phase modulation to the backward going beam. The speed of the lattice can be calculated by determining the phase velocity of the standing wave profile which in terms of velocities is written as

$$v_P(t) = v_l - v_c \sin(2\pi f_c t), \tag{5.36}$$

where we've introduced the central lattice velocity $v_l = 1/2\lambda f_\Delta \approx 290\,\mathrm{m\,s^{-1}}$, and the chirped velocity range $v_c = 1/2\lambda f_c \Phi_c \approx 10\,\mathrm{m\,s^{-1}}$.

Pulsing the light off also has another benefit of decreasing the fraction of metastable atoms lost through spontaneous emission from the 4P energy level. Although the beams are detuned from the 2S-4P resonance, a small amount of population may still be off resonantly coupled to the 4P state, therefore a short pulse duration allows for reduced spontaneous emission.

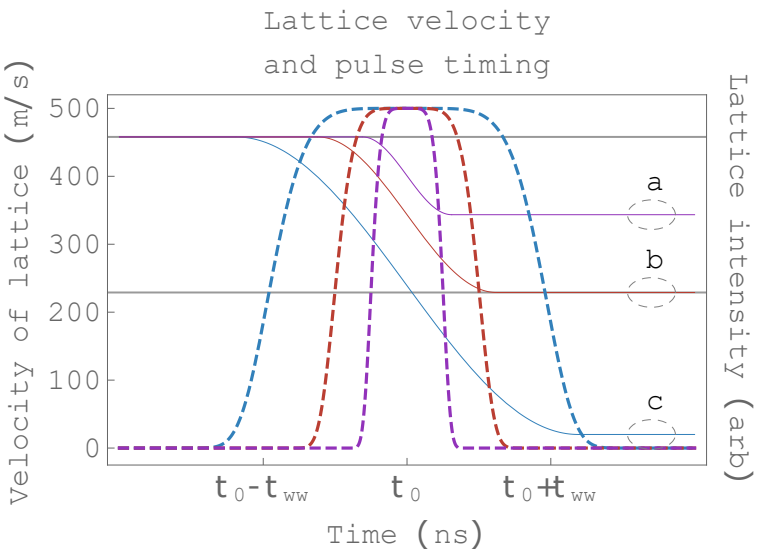

Figure 5.8: Timing diagram of three separate slowing amounts. The horizontal axis is only showing the pulse width of the largest pulse in blue dashes which has the greatest slowing amount. Because the potential depth is fixed by the laser intensity, there is a maximum acceleration that one can apply to the lattice before atoms are no longer trapped within individual lattice wells. This is why the solid curves all have the same maximum slope at t_0, and the pulse must be extended to compensate for greater deceleration amounts.

5.1.5 Deceleration simulations

We perform semi-classical numerical modeling of atomic motion in an optical lattice with the assumption that the motion of the optical lattice is slow compared to the evolution of the atom and the localization of the atomic wavefunctions is small compared to the lattice spacing. These simulations aided us in determining the required optical power and optical control requirements to accomplish a first proof-of-principle demonstration of decelerating hydrogen. Additionally, these simulations were also used to understand the spatial profile of the atomic beam.

In our semi-classical trajectory simulation, we numerically integrate the classical equations of motion

$$\begin{aligned} \vec{r}(t=0) &= \vec{r}_i \\ \dot{\vec{r}}(t=0) &= \vec{v}_i \\ \ddot{\vec{r}}(t) &= -\frac{\nabla V}{m_H}. \end{aligned} \tag{5.37}$$

Where $\vec{r}_i$ and $\vec{v}_i$ are initial conditions defined by the atomic beam, and $V = V\left(\vec{r}, I(\vec{r},t)\right)$ is the potential formed by the AC stark interaction from sec. 5.1.2, and where $I(\vec{r},t)$ is the time varied intensity as described in sec. 5.1.4. The probability that the atom is still present for detection after interaction with the optical lattice is also estimated by simulating the spontaneous emission for each atomic trajectory due to off resonant excitation to the 4P described in sec. 5.1.3. Our Monte Carlo (MC) simulation selects a set, S_n, of n initial conditions $S_n = \left\{(\vec{r}_1,\vec{v}_1),(\vec{r}_2,\vec{v}_2),\ldots,(\vec{r}_n,\vec{v}_n)\right\}$ and tracks the position, velocity, and acceleration, as well as left over 2S population over time for the S_ith initial conditions which simulate the metastable atomic beam's spatial and velocity distributions determined in the previous chapters. The model for the optical potential included the spatial extent of the focused Gaussian laser beam which could be aligned at various angles to the initial atomic trajectories. Full 3D simulations of the trajectory allowed for analysis of final position and velocity for varied laser field alignment geometries.

Example simulations for a single atom trajectories with initial velocities of $300\,\mathrm{m\,s^{-1}}$ and $1200\,\mathrm{m\,s^{-1}}$ with lattice conditions set to also start at the atomic initial speeds and decelerate by

$20\,\mathrm{m\,s^{-1}}$, $200\,\mathrm{m\,s^{-1}}$, and $1180\,\mathrm{m\,s^{-1}}$ over the course of the optical pulse is shown in Fig. 5.9 and Fig. 5.10.

Typical MC simulations ran over one to five million trajectories spread evenly over the radial and axial directions with respect to the laser beam within 1-2 beam waists ($w_0 = 180\,\mu\mathrm{m}$), and with varied input angles and velocities within $\pm 100\,\mathrm{m\,s^{-1}}$ of $300\,\mathrm{m\,s^{-1}}$. Some simulations were also run over larger spatial and velocity ranges to probe various parameter spaces, however the majority of the simulations were run within the trap depth ($\approx 15-30\,\mathrm{m\,s^{-1}}$) of $300\,\mathrm{m\,s^{-1}}$. A depiction of a group of initial atomic velocities initialized near the trapping velocity range of the atomic lattice is shown in Fig. 5.9 and Fig. 5.10. Shown in this Fig. 5.9 is only the axial, z-component, of the atomic position in the initial reference frame of the optical lattice velocity of $300\,\mathrm{m\,s^{-1}}$. This means that a trajectory with zero slope in the zt plane is moving at $300\,\mathrm{m\,s^{-1}}$, and negative slopes represent the effect of the lattice decelerating the atoms. Over the duration of the optical pulse, if the atom is captured by the optical lattice, it will oscillate within the potential wells, and when the potential decelerates, the atom will experience a deceleration defined by the change in the lattice speed. If atoms are not captured, they will escape over the top of the potential wells and be relatively unaffected.

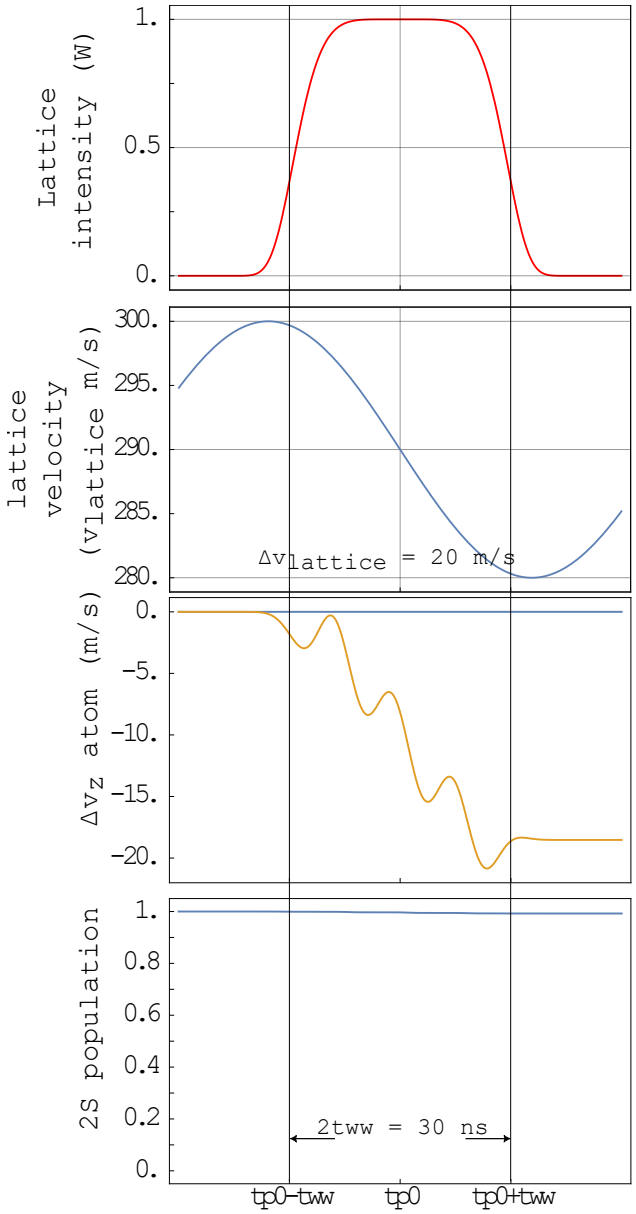

Figure 5.9: Individual motional and population tracking of an atom trajectory through the pulse and lattice phase modulation given in the upper two plots.

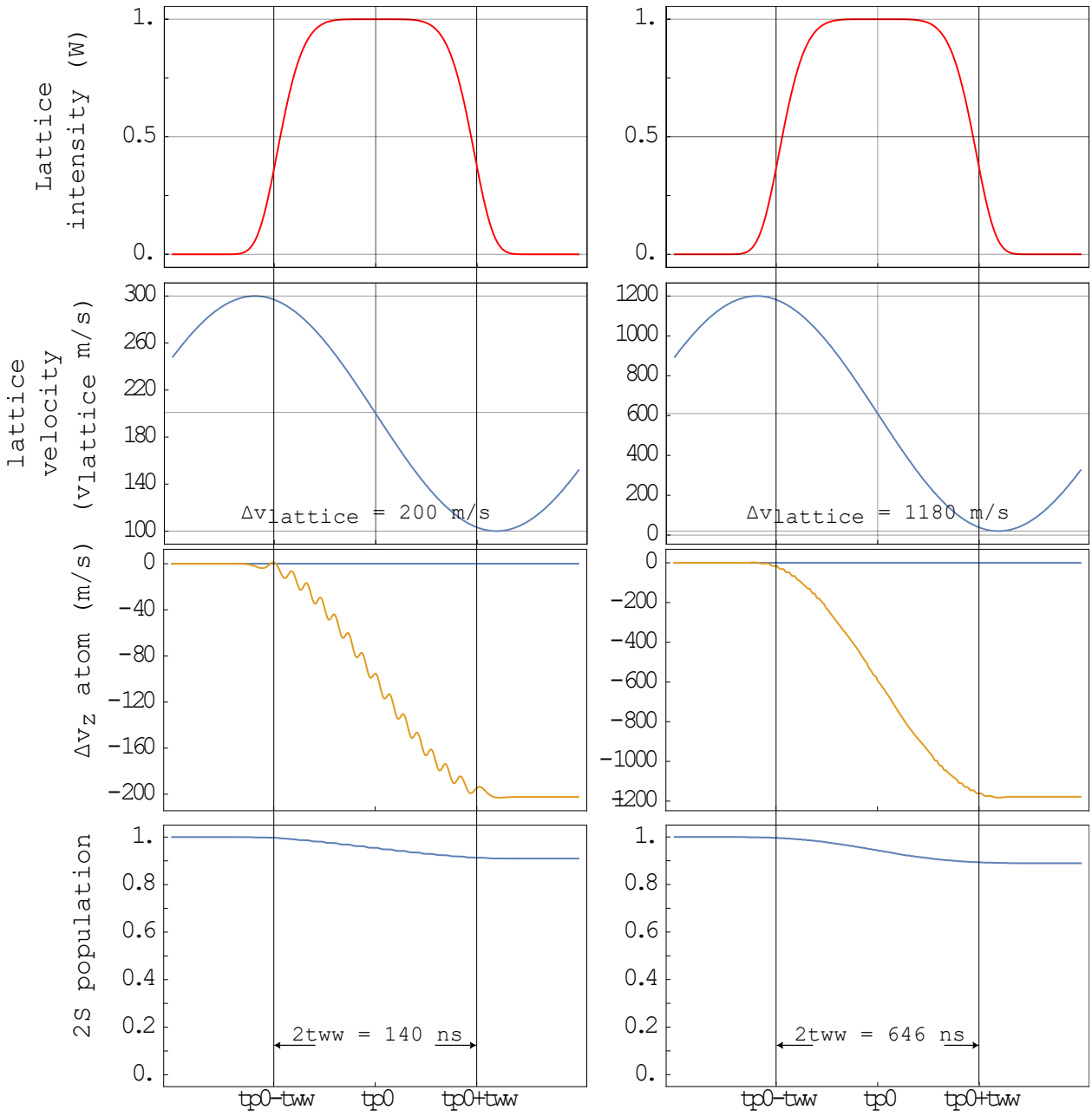

Figure 5.10: Individual motional and population tracking of an atom trajectory through the pulses and lattice phase modulations given in the top plots. A change in velocity of 200 m/s (left) and 1180 m/s (right). Although the orange trajectory plots look like the trap oscillation amplitude and frequency are different, they are approximately the same (not exactly since this is particle initial condition dependent and these trajectories were selected randomly). Notice, that because the pulse length is longer, more of the atomic population is lost in the lowest panels, from left to right.

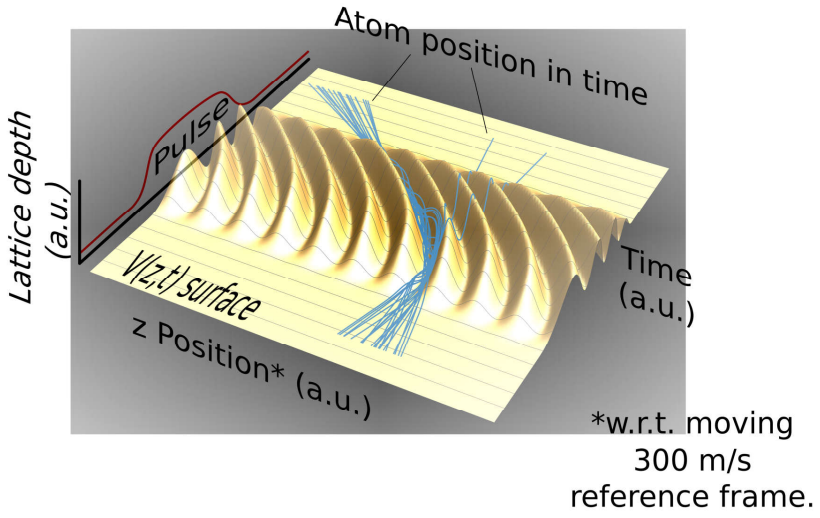

Figure 5.11: MC simulation results depicting atomic trajectories (blue tracks) in a pulsed and decelerating lattice ($V(z,t)$ surface) versus time over the course of a laser pulse along the z-direction. The axial, z, position is with respect to the initial velocity of the lattice at $300\,\mathrm{m\,s^{-1}}$, and a projection of the laser intensity pulse over time is plotted in the red 2D plot. In this simulation, atoms are initialized with random velocities near $300\,\mathrm{m\,s^{-1}}$ within the capture range of the lattice. Therefore, they have small slopes in the zt plane. After a deceleration cycle is run, the atoms are released from the lattice with reduced velocities, and therefore have negative slopes in the zt plane. Notice that some trajectories that are not initially trapped within the optical well escape and slowing is not accomplished on these atoms.

It is interesting to look at the effect of the deceleration procedure on the velocity distribution of the atoms. In the case of ideal experimental conditions where we may center the initial lattice velocity on the peak of the distribution, and be able to program any deceleration amounts to the system, then we should be able to collect a large group of atoms in the optical lattice, and move them down to any speeds. Figure 5.12 shows this effect when 4.2 W of laser power is available. The simulations in fig. 5.12 use a blue detuning of 8 GHz and a spot size of 80 µm with various timing and deceleration amounts, as shown. Two things are apparent in this simulation which is that the overall beam flux is reduced for the longer the pulse duration is which can be seen by the reduction in the velocity distribution overall height. This is because of the longer 2S-4P excitation time which is captured in the simulation. Despite the overall quenching increase for longer pulse durations, we do not see a significant amount of quenching for the atoms that are decelerated. This is expected due to the blue detuning of the lattice causing the atoms to be pushed towards the low

intensity regions of the lattice where they will experience reduced 2S-4P excitation. One can notice that although in fig. 5.12b, the remaining unslowed velocity distribution appears to be relatively Maxwellian in fig. 5.12, there is a region of initial atomic velocities which are sped up by a small amount. This is expected for atoms which the lattice does not trap.

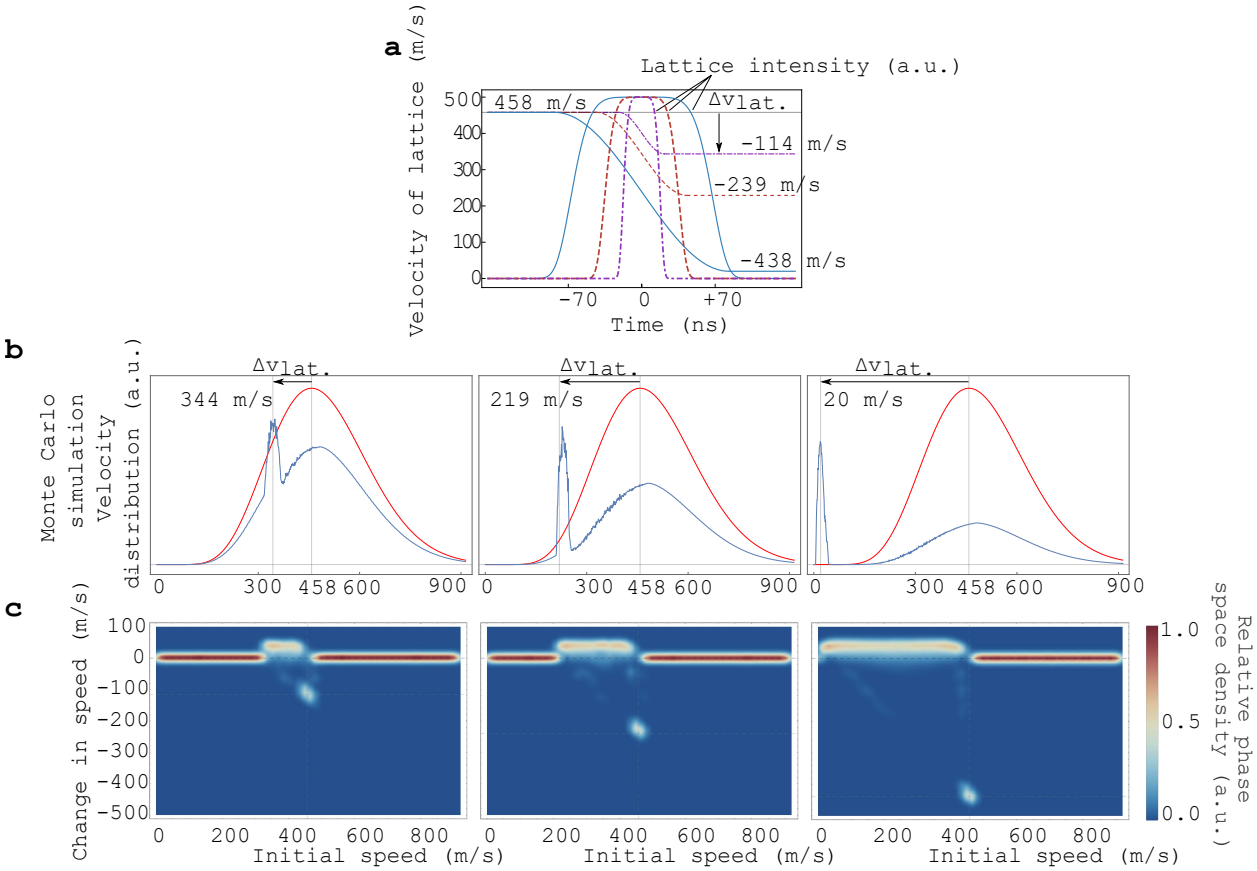

Figure 5.12: Simulations run for the metastable atomic velocity distribution measured by time-of-flight in earlier measurements. This simulation used a laser power of 4.2 W, and 80 µm spot size, and 8 GHz detuning. **a)** Reiteration of the timing diagram for the conditions operated in this simulation. The greater slowing amounts require longer pulses since there is a maximum acceleration set by the trap frequency. **b)**. Changes in the velocity distribution for the three deceleration amounts in part **a)**. We notice the unslowed portion of the velocity distribution is reduced for longer pulse times, yet the slowed atomic signal is not. This is expected since the slowed atoms are trapped in a blue detuned lattice with minimal coupling of the 2S-4P transition, whereas the unslowed portion of the atomic beam sample a significant amount of the high intensity parts of the lattice. **c)** The effect of the deceleration pulse on flat velocity space given an even starting distribution of atomic initial velocities. Notice that some group of unslowed atoms are actually sped up by the laser interaction.

A useful configuration of the optical slower is to place the lattice beam at a 45° angle where the atoms that are slowed receive a small tangential kick out of the original metastable beam that is proportional to the amount of slowing imparted, deflecting atoms at an angle into a background free region.

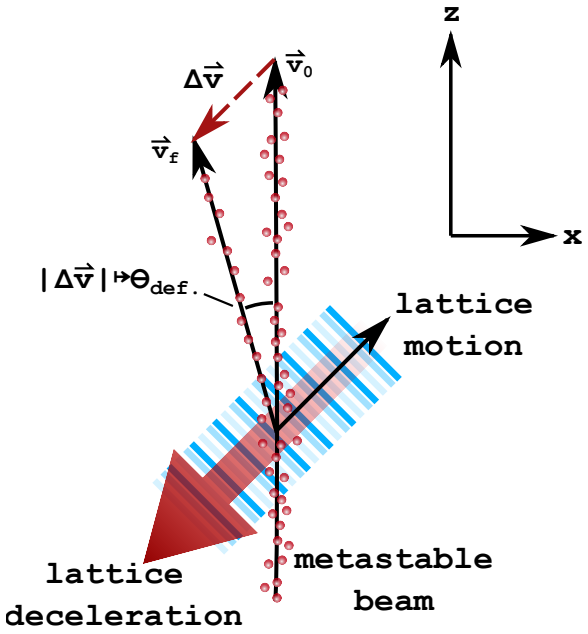

Figure 5.13: Schematic of proof of principle experiment for angled deceleration lattice. By placing the decelerating lattice at an angle to the atomic beam, the atoms will receive a kick along the axis of the lattice, causing a small deflection into the x-direction equal to the deceleration along the z direction. This has the effect of geometrically mapping the slowed amount into angle of deflection. Atoms deflected out of the original metastable beam can be distinguished easily in this case by an off axis channeltron detector.

As is easy to see based on the lattice intensity pattern's spatial aspect ratio in fig. 5.6, it is a good approximation that the optical lattice only exerts a force along its propagation direction. This means the 45° angle between the metastable beam and optical lattice the lattice will provide a velocity kick of equal magnitude to the x and z-directions of the beam. Atoms with initial velocity of $\vec{v}_i = (0,0,300)\ \mathrm{m\,s^{-1}}$ have a final velocity of $\vec{v}_f = (20,0,280)\ \mathrm{m\,s^{-1}}$, which is a change from $|\vec{v}_i| = 300\ \mathrm{m\,s^{-1}}$ to $|\vec{v}_f| = 280.7\ \mathrm{m\,s^{-1}}$ (approximately a deceleration of $20\,\mathrm{m\,s^{-1}}$) that is visible to the off-axis detector. A stationary detector placed ≈3.9° off axis would geometrically be

constrained to only see atoms that are initially travelling near the lattice initial velocity and slowed approximately $20\,\mathrm{m\,s^{-1}}$.

As discussed in sec. 5.1.4, we have the ability to easily control the lattice velocity timing and amplitudes through electro optical modulators. With the model presented previously, we can program a simulation with the experimental optical control (values discussed in later sections of this chapter) allowing for Monte Carlo prediction of the expected detection signals for apparatus set up with the 45° intersection. Figure 5.14 shows the results of one MC simulation for the angled lattice configuration mentioned above, where the lattice is set to apply a kick of $\sqrt{2}\times 20\,\mathrm{m\,s^{-1}}$ along the laser axis, or $20\,\mathrm{m\,s^{-1}}$ along the atomic beam axis. As is seen by the linear trend, the final angle at which the atoms exit the slowing region are directly proportional to the change in speed the atoms experience.

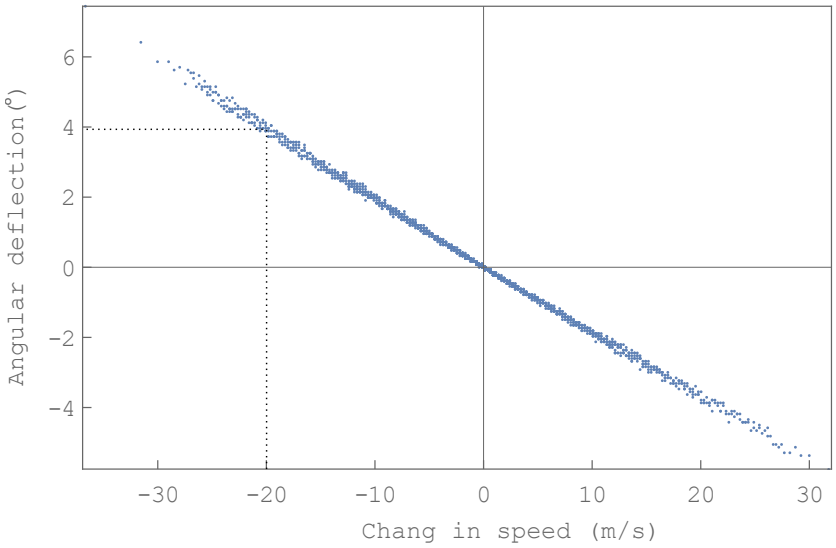

Figure 5.14: Monte Carlo simulation of many initial atomic trajectories in a $20\,\mathrm{m\,s^{-1}}$ decelerating lattice placed at an angle to the atomic beam. The angle of departure from the deceleration region is mapped to the change in speed of the atoms which means a single detector off axis at $\approx 4°$ will observe atoms that experienced a change in speed of $-20\,\mathrm{m\,s^{-1}}$, even if other final changes in speed are caused over the deceleration cycle.

As can be seen from the range of output angles in fig. 5.14, there will be a distributions of metastable atoms spread out over the horizontal detection plane which we place at 27.5 cm after the slowing interaction region.

In order to predict the experimental detector signals from MC simulations, we run our simulation repeatedly over a range of initial atomic trajectory conditions based on the characterization of our metastable beam (chapters 2, 3). For the simulation's range of initial positions, we assume that the atomic beam is spatially uniform in the y-direction (radially away from the 486 laser's beam width). We allow the laser beam to vary as a Gaussian beam to capture the effect of the laser spatial intensity profile. We use uniform sampling along the z-direction, however, we delete any trajectory which would not collide within three beam widths of the 486 laser pulse to reduce the overall MC simulation time. Simulating trajectories further away is unphysical since only one pulse is simulated however, the experiment is conducted with a continuous pulse train. In choosing the atomic beam density in the x-direction, we choose to simulate trajectories with initial horizontal position, $x = 0$, convolved with a supergaussian estimation of the atomic beam profile, as shown in fig. 5.15. This convolution greatly reduces the number of trajectories required to simulate in the MC, greatly reducing computation time and memory/storage requirements. The validity of the convolution assumes that the slice of initial trajectories along the $x = 0$ plane will behave nearly identically to all of the horizontal, x, positions over the atomic beam. This is a decent approximation since the metastable atomic beam width is mainly determined by the atomic beam skimmers ($\approx$1 cm ground state atomic beam width) rather than the 243 nm two-photon excitation (Rayleigh range $\approx$212 cm), and the 486 nm laser's intensity is roughly constant over the atomic beam width (Rayleigh range $\approx$3 cm) at the deceleration interaction position. For a single x-positional beam simulation, the resulting detector plane intensity (including off resonant quenching) is plotted in fig. 5.15, as well as the result of the signal after applying a numerical convolution over this intensity.

The metastable beam intensity can be iterated over lattice conditions which we can run experimentally using the electro optics. Shown in fig. 5.16 is the atomic beam intensity at the detection

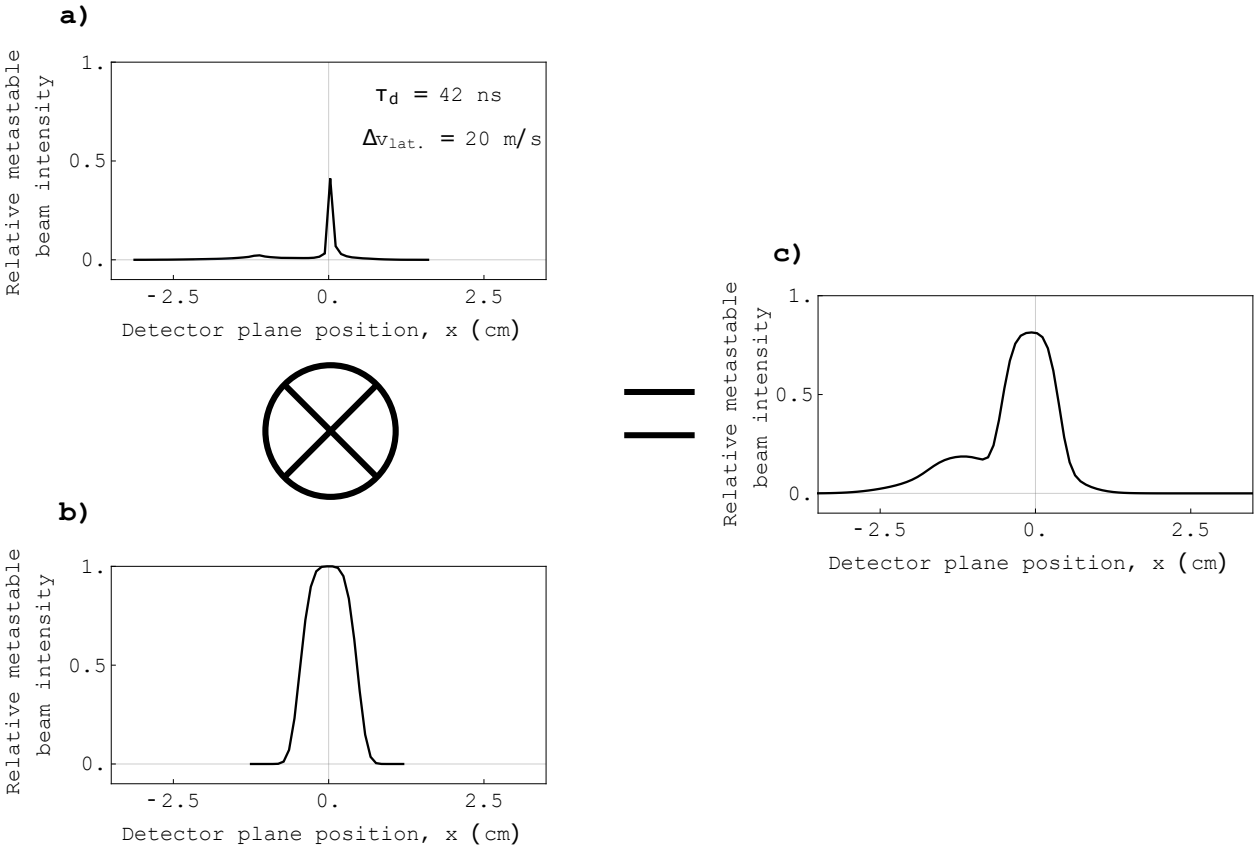

Figure 5.15: Depiction of the numerical convolution performed for the atomic beam width used to calculate experimental signal expectations. The initial x-position of 0 cm is used and the interaction with the laser determines the final position at the detection plane of $z = 27.5$ cm. The simulated deflection of the centerline of the atomic beam (**a**) is convolved with the estimated atomic beam width (**b**), giving the overall spatial distribution of metastable hydrogen in the detection plane **c**. This simulation is given for a pulse delay of $\tau = 42$ ns, and a change in lattice velocity of $\Delta v_{lat.} = 20\,\mathrm{m\,s^{-1}}$. Normalization is defined based on the initial metastable beam intensity with the laser turned off. The centerline intensity lying below 1 means that there is off resonant excitation and quenching of a fraction of the atoms.

plane swept over a range of lattice acceleration amplitudes. The lattice velocity as shown in the left column of fig. 5.16, and the intensity on the right.

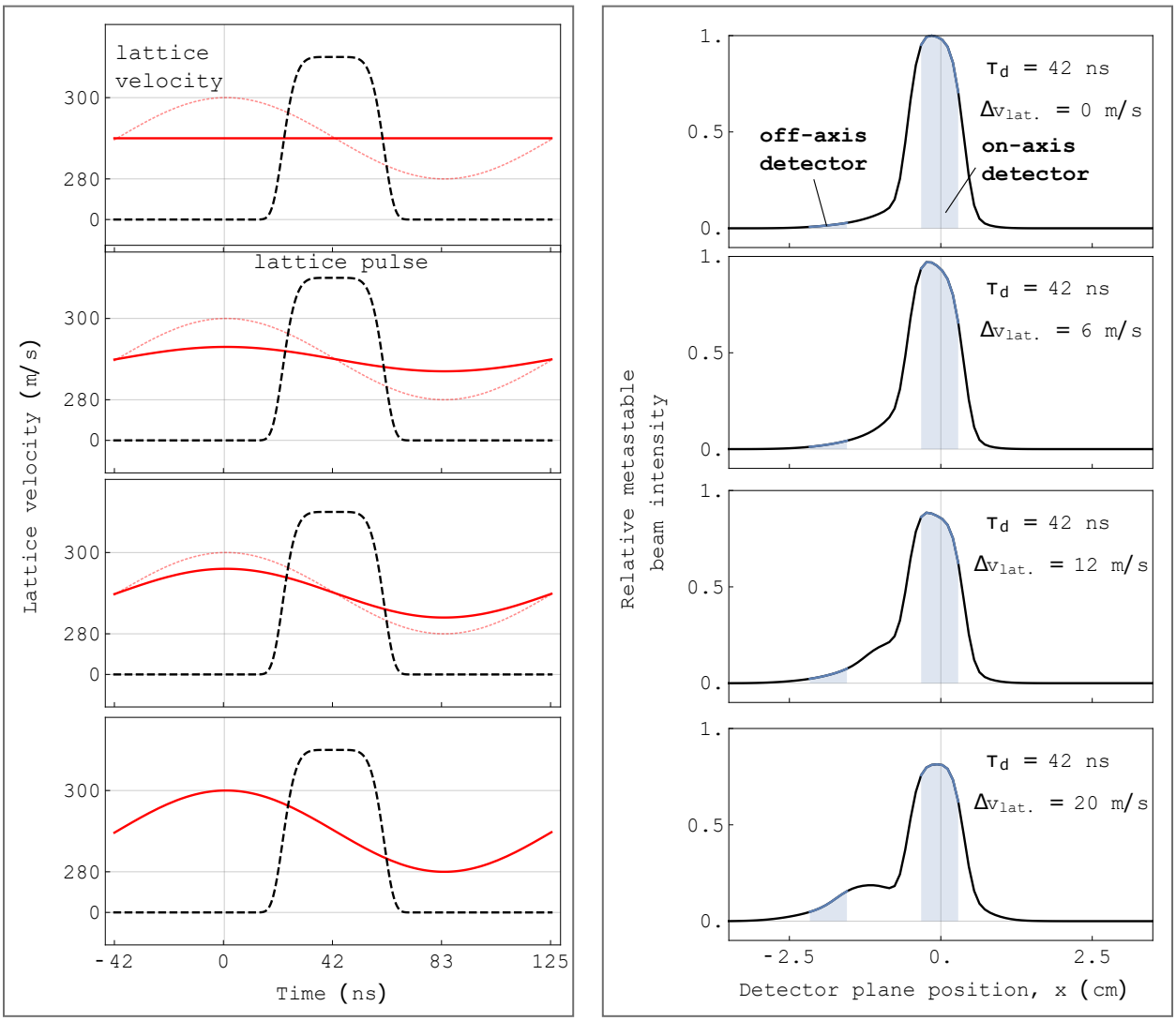

Figure 5.16: Simulated metastable atomic beam intensity profile under varied lattice acceleration amplitude with fixed pulse to lattice velocity timing. The lattice pulse amplitude and lattice acceleration are shown on the left column with the corresponding metastable atomic beam intensity shown on the right column. The increase in lattice acceleration pushes more atoms toward the off-axis detector, which as shown in fig. 5.14, also means more atoms are decelerated.

We can also easily vary the relative timing of the pulses with respect to the lattice acceleration as shown in the left column of fig. 5.17. For a range of these parameters, we can simulate atomic trajectories to collect the atomic beam intensity at the metastable atom detector plane which are

placed at $z = 27.5$ cm (based on fig. 5.13. As can be seen by the right columns in figs. 5.16 and 5.17 the portion of the beam intensity integrated by each detector will vary based on the lattice control parameters. The simulations were run for the experimentally reasonable conditions of $\approx$1 W of 486 nm laser power focused to a spot size of 80 µm and a detuning of 1.5 GHz and 1.2 GHz. As we can see in fig. 5.16, if we fix the lattice pulse on the decelerating part of the EOM cycle and vary the amplitude of the lattice acceleration we would expect an increase in atoms pushed towards the off-axis detector. We can also vary the pulse to lattice acceleration timing with a constant lattice acceleration amplitude and observe a modulation of the beam intensity profile, fig. 5.17.

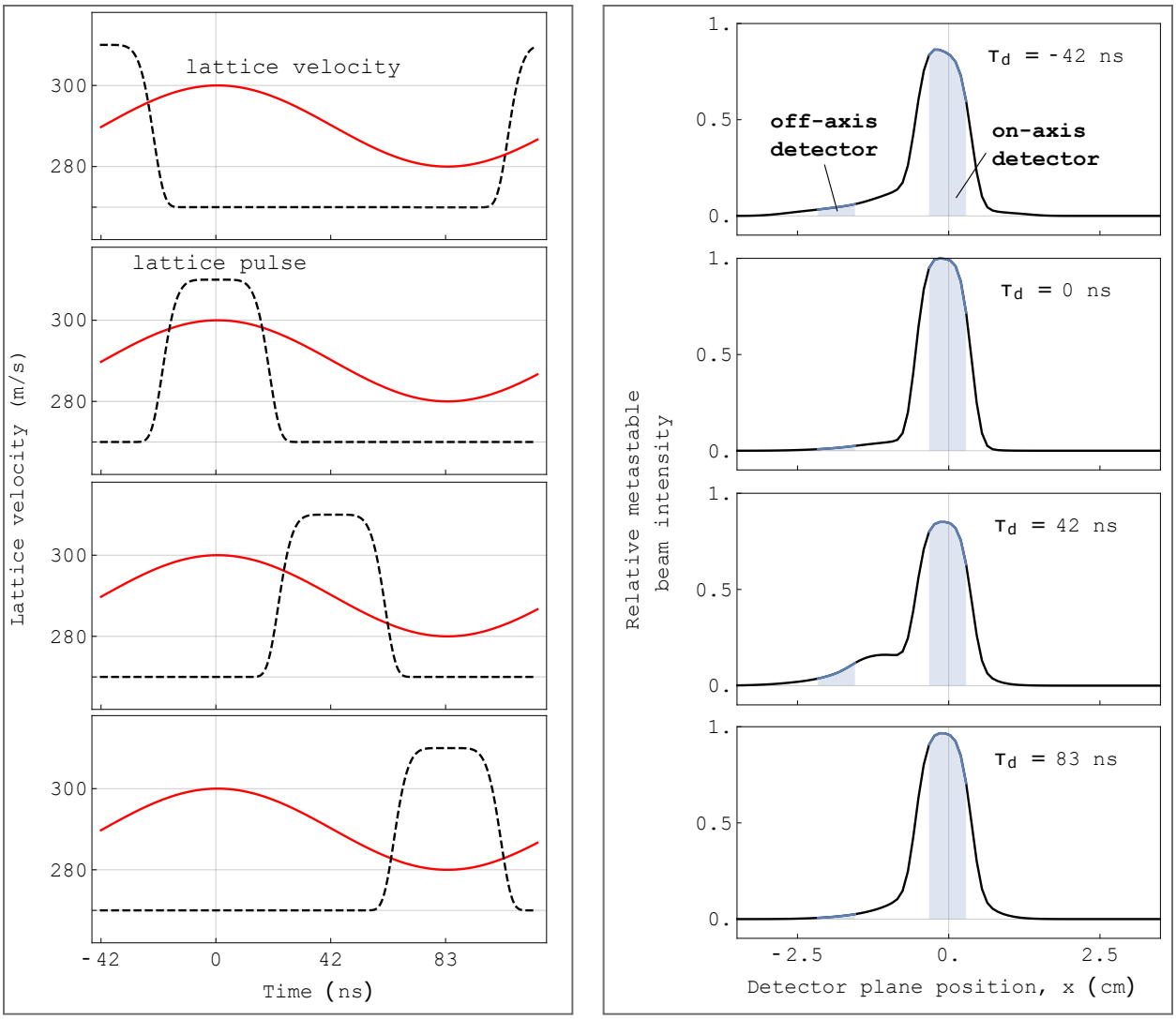

Figure 5.17: Simulated metastable atomic beam intensity profile under varied pulse to lattice velocity timing with fixed lattice acceleration amplitude. Notice that at $t_d = 0$ ns there is a small deflected number of atoms asymmetrically toward the deceleration direction. This is likely due to the fact the lattice is moving near the atomic reference frame due to the constant lattice central velocity (set by a double passed AOM).

In the experiment, we normalize the off-axis detector signal with respect to the on-axis detector signal to minimize noise and experimental fluctuations. If we compute the ratio of off-axis counts to the on-axis counts, the normalized integrated beam flux, we can make predictions of the experimental detector signal with respect to the lattice control parameters which are shown in fig. 5.18

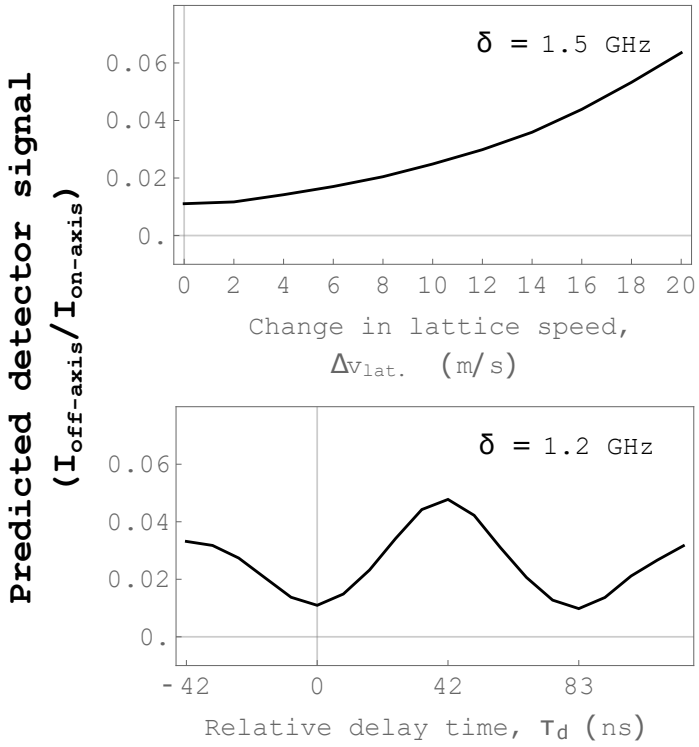

Figure 5.18: Expected signal shapes of the ratio of off-axis to on-axis counts for experimentally reasonable conditions and control variables.

5.2 Experiment

Figure 5.19 shows a diagram of the experimental apparatus used to implement the 45° optical lattice deceleration and deflection for the initial demonstration.

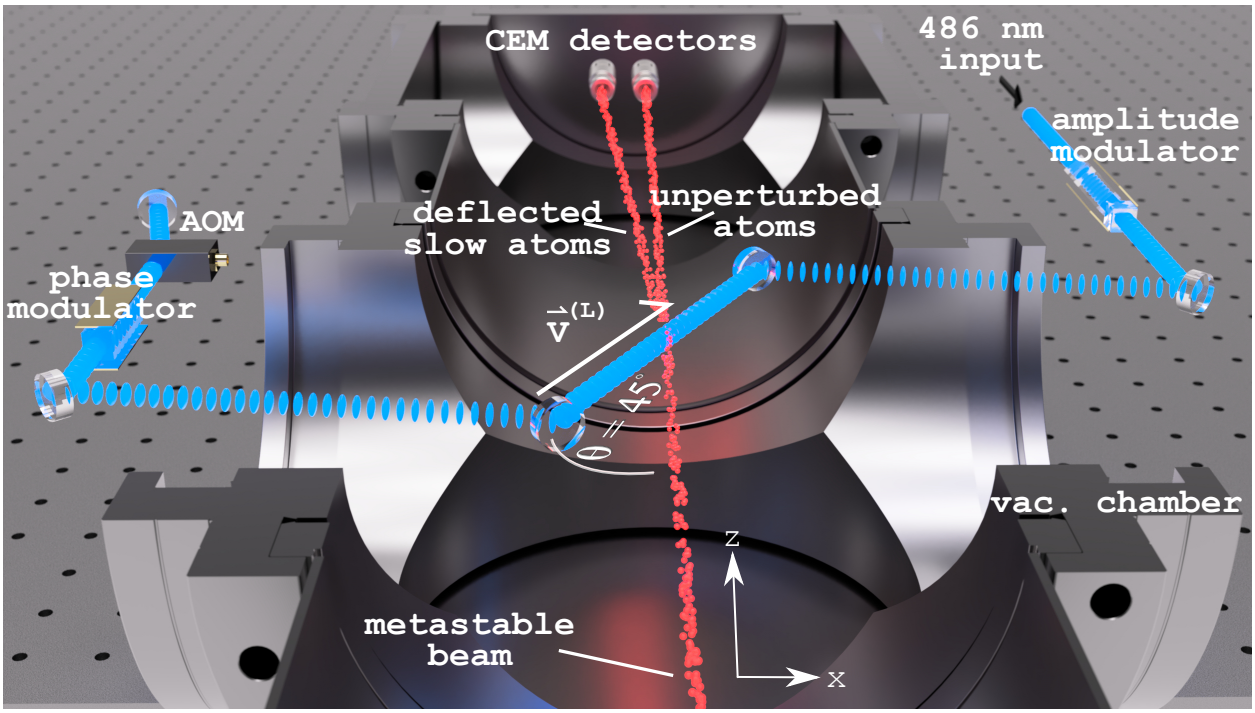

Figure 5.19: Diagram of the experimental apparatus used to demonstrate initial optical slowing of atomic hydrogen. The metastable H2S beam is generated upstream of the 486 nm slowing lattice. Two CEM detectors are placed down stream, one on axis of the H2S beam to measure the overall metastable beam flux for normalization, and the off axis detector at 3.9° serves as the slowed atom detector. For clarity, the Faraday cage which shields the metastable beam from stray electric fields has been omitted. The lattice is controlled with double passed AOM and EOM to set the central velocity and acceleration, and the input beam amplitude is modulated with a home-built Pockels cell before the optical viewport into the vacuum chamber. In vacuum high power 532 nm HR mirrors steer the lattice beam to intersect with the H2S beam at 45°.

Generation of an optically excited and velocity characterized cryogenic atomic beam of metastable 2S hydrogen using cavity enhanced 243 nm light to excite the two photon 1S-2S transition is described in Chapter 3 and in our previous works [8, 10, 12, 54]. The 486 nm optical lattice intersects the metastable H2S beam at a 45° angle. For this work, the metastable beam defines the $+z$-direction of the experiment, the x-direction is in the plane of the optical lattice and metastable beam, and the y-direction is normal to the optical table. Atoms which are decelerated are also deflected in the $-x$ direction of the original metastable beam and are detected off axis by a channel electron multiplier as explained in Sec. 3.3. A second detector is placed on axis to measure the on axis metastable flux for signal collection normalization and system diagnosis. The optical

modulation system controls the intensity and motion of the optical lattice through the amplitude modulator, phase modulator, and AOM respectively to achieve the control previously described in Sec. 5.1.4. The design, construction, and control of the optical modulation system are described next.

5.2.1 Setup

The slowing lattice laser source follows the Master Oscillator Power Amplifier (MOPA) scheme from [10] minus the fiber amplification stage. Laser light begins with a Littrow configuration extended cavity diode laser (ECDL) at 972 nm, is amplified with a commercial DILAS tapered amplifier (TA) and frequency doubled to 486 nm using an AR coated lithium triborate (LBO) crystal in a resonant bowtie cavity. Typical operational conditions of the 486 nm beam were ≈850 mW CW and we were able to produce up to 1.3 W with only one TA stage and no fiber amplifier. The output of the doubling stage is shaped and collimated and we measured $m^2 = 1.2$. After optical losses the laser typically had approximately 750 mW of forward going and 600 mW of backward going power and is focused to an 80 µm spot size at the atomic slower intersection. These values lead to $I_0 = 37\ \mathrm{MW\,m^{-2}}$, $R = 0.8$. The detuning of the laser was tuned by adjusting the ECDL cavity length with a piezoelectric transducer (PZT) and the absolute frequency of the ECDL seed light was monitored on an optical spectrum analyzer. The ECDL frequency was free running and not phase locked to a frequency comb or stable cavity and therefore would drift by 100s of MHz but would remain steady enough for our experiments since the overall detuning was a factor of 10 greater than the drift.

The layout of the 486 nm MOPA system is laid out in Fig. 5.20. To form the optical lattice trajectories to perform deceleration, a system of optical modulators are used to control the amplitude of the lattice (well depth), phase modulation (acceleration), and central lattice velocity. For simplicity the system was arranged in a retro-reflected configuration to form the optical lattice wells. As shown in Fig. 5.19, the amplitude modulation is controlled on the input beam following the 486 nm source, and the phase and frequency modulation elements are placed in the beam after the

input beam crosses the atomic interaction region. After the atomic interaction region, the beam double-passes a phase modulation EOM and acousto optical modulator upon retroreflection. As discussed in the previous section, this causes the necessary relative frequency modulation between the forward and backward going beams which causes the optical lattice to translate and accelerate. The double-pass of the two modulation optics allows for a simple way to achieve greater phase and frequency modulations for the two optical elements.

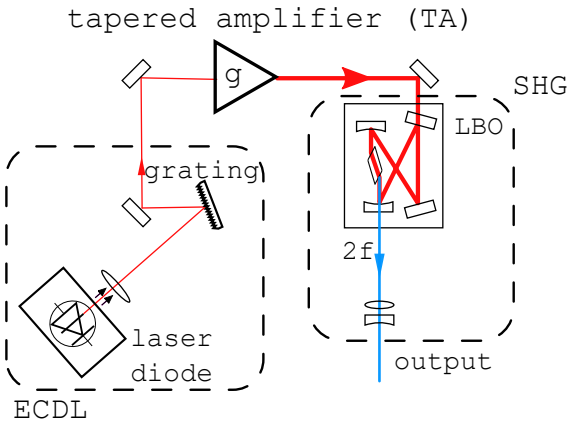

Figure 5.20: Diagram of the laser system used for the deceleration lattice. The seed laser is a home-built ECDL in Littrow configuration which was amplified in one stage with a tapered amplifer (TA) before blue 486 nm light was generated through second harmonic generation through a lithium triborate (LBO) crystal in a resonant bowtie build up cavity. The output power was capable of 1.3 W of CW 486 nm radiation with $m^2 \leq 1.2$.

Shuttering of the slowing laser was implemented using a Conoptics model 380 electro optical modulator described with more detail in section C. Motion of the optical lattice was monitored in situ using the Michelson interferometer on the input arm of the slower with a photodiode and oscilloscope shown in Fig. 5.21. The reflected arm of the beam was aligned with a cat-eye reflector which reduced the sensitivity to temperature related misalignment and also allowed for high quality beam overlap in the interaction region which could be monitored based on the quality of the interferometer fringe.

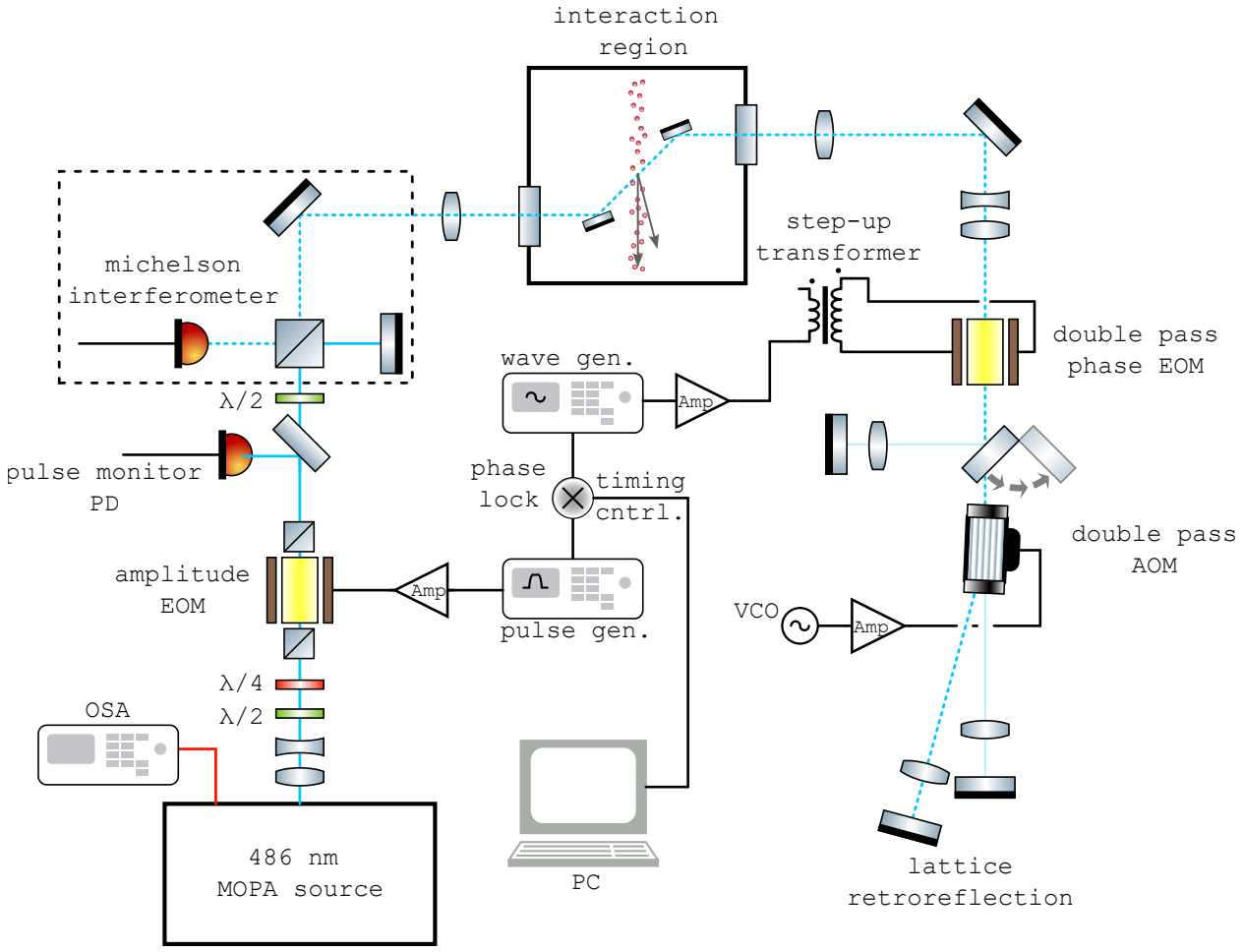

Figure 5.21: The lattice is controlled with double passed AOM and EOM to set the central velocity and acceleration, and the input beam amplitude is modulated with a Pockels cell before the optical viewport into the vacuum chamber. In vacuum high power 532 nm HR mirrors steer the lattice beam to intersect with the H2S beam at 45°. The slowing laser frequency is free-running and monitored for the detuning with an optical spectrum analyzer (OSA) at the 972 nm laser diode seed.

As shown in Fig. 5.19, direct RF electronic control of the phase velocity in 5.32 with an AOM and EOM placed in the 486 beam after the first pass through the interaction region. The return beam receives a frequency offset from the AOM with a tuning range of $700-900$ MHz after being double passed. This sets up a value of $v_l \approx 290\,\mathrm{m\,s^{-1}}$ at 45°. To apply the frequency chirp and accelerate the lattice the beam is double passed through a 3 by 20 mm long y-cut phase modulation EOM made from magnesium doped lithium niobate which exhibits a relatively high r_{33} coefficient ($r_{33} = 32\,\mathrm{pm\,V^{-1}}$). The magnesium doping helps improve the damage threshold of the crystal. A

longer Lithium Tantalate EO crystal was tried but was found to quickly degrade under the laser intensity operated here ($\approx 0.2\,\mathrm{MW\,m^{-2}}$). The second EOM is a phase modulator and is resonantly driven by a voltage step up circuit at $5-6$ MHz. Both the amplitude and phase modulation EOM's signals are seeded by the same function generator so that the relative timing between the two can be adjusted directly with the function generator. Figure 5.22 and fig. 5.23 show experimental data demonstrating our electro-optical control of the optical lattice. These are optical signals collected with photodiodes monitoring the optical beam pick-offs shown in fig. 5.21. The instantaneous frequency (or velocity) of the optical lattice interference is measured on a photodiode on the output arm of the Michelson interferometer. The experimental optical pulse shape and the control over the relative timing with respect to the lattice motion is shown in Fig. 5.22. The DC offset of the instantaneous lattice frequency is controlled by changing the double passed AOM frequency. Pulse timing is controlled by delaying the optical pulse triggered by the pulse generator. Control over the deceleration amount is shown in Fig. 5.23 which is done by changing the drive amplitude to the resonant step-up transformer EOM driver circuit.

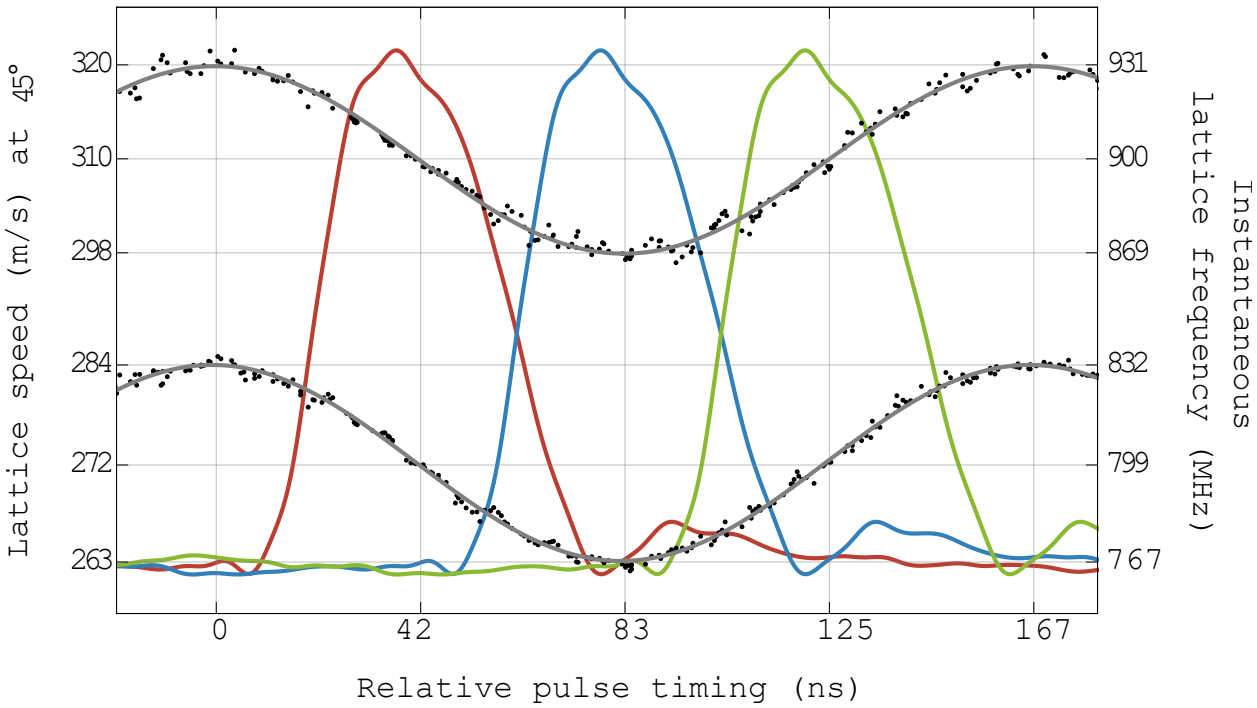

Figure 5.22: Experimental data on the deceleration of the optical lattice. Black data points along with grey fits correspond to the y-axes. The colored pulse shapes are signals of the lattice intensity and are plotted with arbitrary scale to show reltaive pulse timing. The lattice pulses are collected by a beam sample of the forward going beam from the 486 nm laser aimed at photodiode. The amplitude of the optical lattice velocity is adjusted by the phase modulation EOM voltage. This data is collected by observing the interference fringes on a photodiode placed on one arm of the Michelson interferometer while operating the AOM and phase modulation EOM shown in fig. 5.21. The interference fringes will generate chirped sinusoid signal traced over time which oscillates between roughly 930 MHz and 750 MHz depending on the AOM frequency and EOM amplitude/frequency as described in sec. 5.1.4. Shown here is with the AOM parked at two frequencies, 400 MHz and 450 MHz with a fixed EOM amplitude. The chirped sinusoid is then analyzed for the instantaneous frequency and converted to lattice speed as described in sec. 5.1.4.

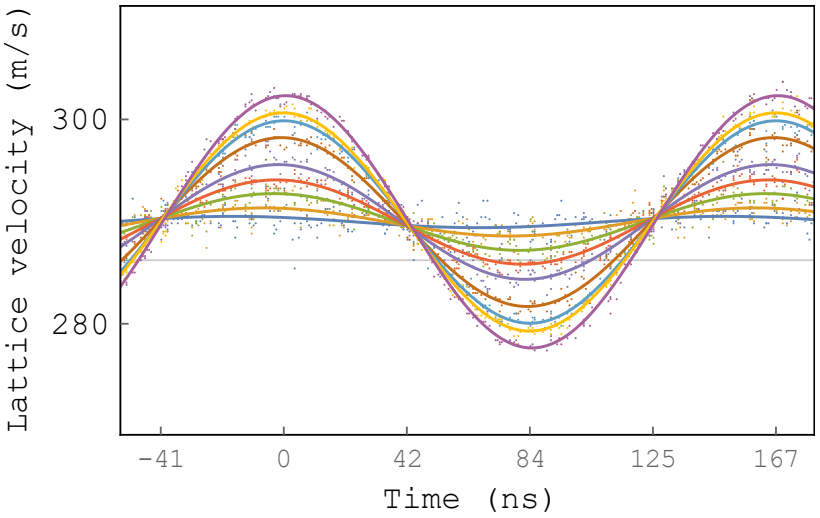

Figure 5.23: Data and sinusoid fit to the optical lattice velocity over a range of amplitudes. The amplitude of the optical lattice velocity is adjusted by the phase modulation EOM voltage. This data is collected by observing the interference fringes on a photodiode placed on one arm of the Michelson interferometer while operating the AOM and phase modulation EOM shown in fig. 5.21. The interference fringes will generate chirped sinusoid signal in time on a photodiode oscillating between roughly 930 MHz and 750 MHz depending on the AOM frequency and EOM amplitude/frequency. The chirped sinusoid is then analyzed for the instantaneous frequency and converted to lattice speed as described in sec. 5.1.4.

For detection of the metastable atoms a channel electron multiplier detector is installed on the axis of the H2S beam to monitor the flux of atoms which allows for normalization of the slowing signals that fluctuate due to factors such as 243 nm intracavity power fluctuations. Placed off axis by 5° a distance of 30 cm from the slowing intersection is another CEM H2S detector that serves to detect the slowed atoms as explained in Section 5.1.5. The channel electron multipliers have a quantum efficiency of approximately 0.1% and are used as in [8] which detect Lyman-α 121 nm emission by 2S atoms DC-Stark quenched through the 2P state which decays to the ground state with a lifetime of 1.6 ns.

Our method of retroreflecting a double passed EOM and AOM is simple to set up and requires few components to modulate and chirp the optical lattice. However, any creative configuration of two beams that have separate frequency control can also deliver the same or perhaps even greater control in slowing. Other methods including two separate frequency controlled lasers are also possible for this slower technique. A method of using travelling wave cavity enhanced slowing

light and modulating the cavity resonance to chirp the lattice position was also considered but not demonstrated here.

5.2.2 Deceleration/deflection signal

Experiments were conducted over the course of a couple of weeks using this setup and results are shown for one day of collection. During data collection, approximately $20000 - 50000$ metastable atoms were excited and detected per second with the on-axis detector. The off-axis count rate was collected with the atomic beam slower over a range of EOM phases, amplitudes, and laser detunings. Approximately 0.2% of the atoms were deflected into the off axis channeltron at the peak slowing alignment for a detuning of 1 GHz. As expected, for the same laser power and beam alignments, when the EOM phase modulation driving voltage was shut off, there would be no counts above background on the off axis detector, and when the EOM phase modulation was applied the greatest flux of deflected atoms would be when the Pockels cell pulse was aligned with the lattice deceleration down ramp as can be seen in Fig. 5.24

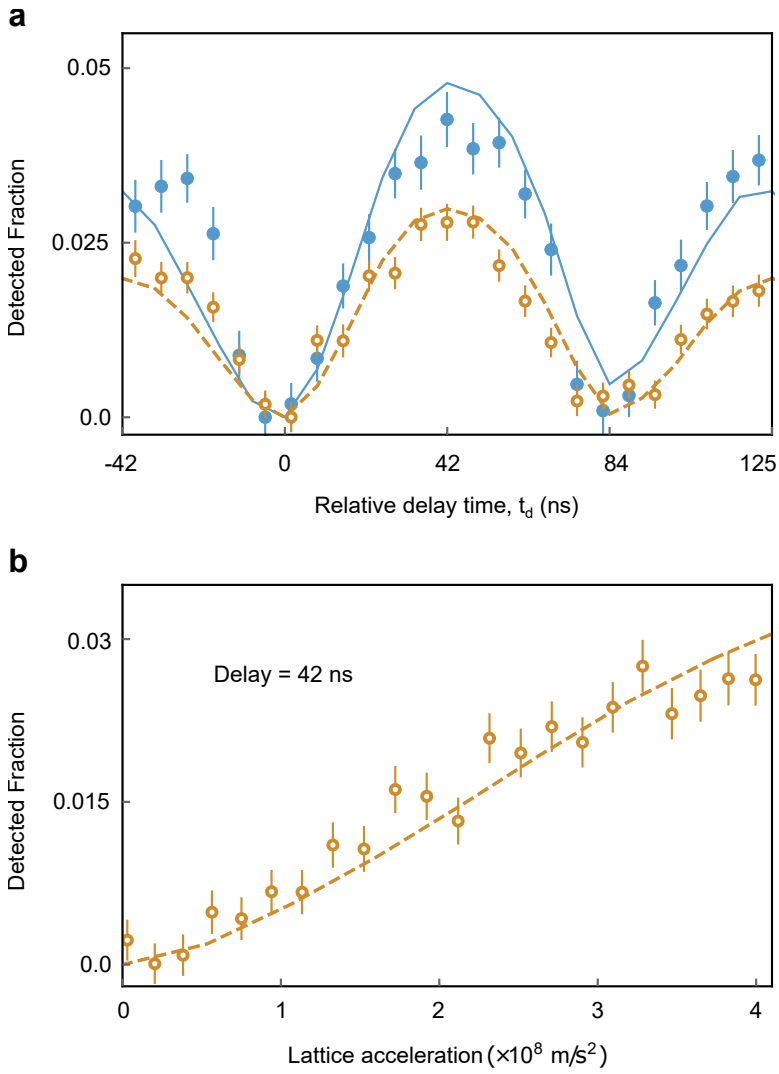

Figure 5.24: Experimental results of the off-axis detection signal for the 45° deceleration experiment over a range of pulse timing delays and lattice accelerations. **a)** The pulse delay was varied with respect to the lattice acceleration for a fixed modulation rate of 6 MHz. See fig. 5.22 for details on what the relative delay is defined by. At $t_d = 0$, 84 ns, the lattice is no longer accelerating, therefore there is no expected signal in the off axis detector and at t_d =42 ns the lattice is at its maximum deceleration ramp of 20 $\mathrm{m\,s^{-1}}$ leading to a peak signal in the off axis detector. Interestingly, there is also a peak when the lattice is at its peak acceleration at t_d =125 ns. This behavior is also expected as the atoms are still decelerated when the lattice is accelerating if they happen to bounce off of one of the wells moving away from it as the lattice shuts off – similar to the paddle slower in [13]. However, these two signals scale differently when moving to larger deceleration amounts and the paddle slowing peak is limited to the depth of the lattice. **b)** The signal in the off-axis detector when the EOM amplitude is varied from 0 to the maximum slowing amount. As expected there is an increase in hydrogen atoms deflected and therefore slowed for increased accelerations.

As was discussed previously in sec. 5.1.5, varying the lattice velocity amplitude or relative pulse timing, as described in Fig. 5.22, there will be a change in the fraction of atoms detected in

the region off axis from the H2S beam. The experimental signal for these two parameter sweeps is shown in Fig. 5.24. For a metastable detector placed 3.9° off of the atomic beam axis, we would expect to detect the greatest number of slowed and deflected atoms when decelerating the lattice by $20\,\mathrm{m\,s^{-1}}$. Perhaps surprisingly there are also slowed atoms expected when the light is switched on during the $v_p(t)$ up ramp. This can be understood in the frame where atoms bounce off of the lattice fringes that are accelerating away, leaving atoms with a lower velocity when the light is then shut by the the pulse. This is fully captured in the model. As can be seen from the density plots in fig. 5.12c, for greater deceleration amounts, the slowed atom signal for an accelerating lattice will stay approximately constant whereas the trapped atoms will be decelerated by the lattice deceleration amount.

Time of flight was not set up during these measurements but could be done by adding another chopper after the slowing region. Although a direct measurement of the velocity of the decelerated atoms was not yet performed, it is also not critical to verifying the method of slowing implemented. The measured signal of phase vs the fraction of the beam deflected into the off axis channeltron definitively shows the high degree of control our lattice method exhibits over a cryogenic beam of atomic hydrogen and indicates the very high accelerations were accomplished over the duration of an optical pulse of 30 ns.

Conclusion

Precision spectroscopy in atomic hydrogen has been a major testing grounds to develop the understanding of physics to date and today is useful in the precise determination of fundamental constants in QED. Moving forward, there is potential to improve the measurements of R_∞ and the proton radius as well as test beyond the physics of the standard model, however this would require improved precision of the experimental techniques available.

So far, the limiting systematics in hydrogen precision measurement boil down to motional effects, be it second-order Doppler shifts, line distortions, transit time broadening, etc. This is why it has been a long sought goal to advance hydrogen spectroscopy with laser cooling or optical manipulation and control of hydrogen and mitigate the motional systematics that arise due to hydrogen's relatively light mass and high speeds. This has been very difficult due to hydrogen's energy structure requiring VUV lasers to do the most basic Doppler cooling.

After some successful, albeit slow, demonstrations of Lyman-α Doppler cooling [37, 119], other methods have been proposed to circumnavigate the highly difficult to engineer lasers including pulsed magnetic field switching [40, 120], two-photon microwave quenched Doppler cooling, molecular hydride trapping and photodissociation [43, 44]. Some ideas have been proposed to perform pulsed laser cooling [41], pulsed sisyphus cooling [36] where an experiment was conducted with Strontium for the method demonstrated in hydrogen/antihydrogen [121]. Also currently pursued is a method of bichromatic force cooling of atomic hydrogen [122]. In this work, we pursued the direct deceleration of continuous effusive beam of metastable atomic hydrogen using pulsed optical lattice where by first exciting the hydrogen atoms into the metastable 2S state with a two-photon transition, a significant dipole force could be exerted on the metastable atoms.

To accomplish this experiment required the construction of a cryogenic atomic beam of hydrogen with time-of-flight velocity characterization as well as the generation of a high powered UV laser source to populate the metastable 2S state. A high powered 486 nm laser source to generate an optical lattice was also constructed, and the electro-optical modulation system was built from

basic components. Simulations of the atomic motion in the optical lattice were performed to study the experimental parameter space and predict experimental signals. By leveraging electro-optical components and RF electronics, we were able to manipulate the motion of a far detuned optical lattice trap to manipulate trapped metastable atoms where we trap a portion of the thermal velocity distribution and adiabatically lower the speed of those atoms. Ultimately, this effort lead to the successful demonstration of proof-of-principle optical deceleration and deflection of an atomic beam of hydrogen.

The successful method of deceleration opens new opportunities to the field of precision hydrogen spectroscopy. To go a step beyond proof-of-principle and take this method toward the ultimate goal of significantly impacting the precision with which measurements can be made becomes a matter of surmounting relatively straightforward technical challenges. Greater electro optical modulation is required to modulate the lattice velocity to a standstill. To achieve a phase modulation that delivers the chirped amplitude demonstrated in chapter 5, we used a 20x3x3 mm Lithium Niobate crystal with a resonant step up transformer up driving voltage of approximately 306 V. To move a velocity class from the most probable velocity of $500\,\mathrm{m\,s^{-1}}$ to zero would require on the order of 10 times the EOM phase shift. This is not a significant challenge as greater lattice acceleration ranges are accessible by increasing this phase modulation voltage (kV are accomplished in Pockels cell drivers), as well as the frequency of the phase modulation, or properties of the EO crystal. The phase shift per volt can be modified significantly by reducing the thickness of the crystal, as well as an increase in crystal length. Additionally, many crystals can be placed in series and multi-passed to achieve larger lattice acceleration ranges. Along another route, significantly greater optical forces are attainable with greater laser power, and other optical transitions may be explored to leverage longer upper state lifetimes or high power lasers. Additionally, Q-switched or ultra-fast pulsed lasers may be used to achieve higher lattice intensities along with chirped pulse shaping accomplish the lattice motion. With some technical improvements of the experiment, bringing hydrogen to a complete stop becomes viable.

Our method of retroreflecting a double passed EOM and AOM is only one way to accomplish the optical control demonstrated here. We chose this method because it was straightforward to set up and requires only three electro optical modulation components to modulate and chirp the optical lattice. However any creative configuration of two beams that have separate frequency control can also deliver the same or perhaps even greater control or slowing. Other methods including two separate frequency controlled lasers or travelling wave optical cavities to power enhance the lattice beam are also possible.

An ideal system would have a slowing lattice aligned parallel with the atomic beam. To directly adapt our retroreflected lattice method for the most parallel to an atomic beam as possible, one could conceivably align the optics beam to within 1° of the atomic beam. We also have explored the simulations of magnetic atomic beam optics to colinearly overlap atomic and optical beams. By reflecting the atomic beam off of a magnetic mirror which can be constructed to be optically transparent, the atoms in the hyperfine stretched m_F state would experience a bounce that could be oriented along with the optical beam of light. Additionally using two separated beams of light one could arrange crossed beams at an angle with respect to each other as in [46] so that at the slowing region the standing wave is travelling axially with the atomic beam.

The direct motional control of hydrogen with optical fields has a bright future benefiting precision measurement. Should a beam of atomic hydrogen be slowed enough to be deflected into an atomic fountain geometry or loaded into a magic wavelength trap for the 1S-2S transition [123, 124], huge benefits may be possible for the ultimate precision of hydrogen spectroscopy. We can only speculate what is next to be discovered when digging into the next few decimal places of hydrogen's lines, regardless, it will be an exciting generation of experiments to witness.

Bibliography

[1] S. S. Schweber, Shelter Island, Pocono, and Oldstone: The emergence of American quantum electrodynamics after World War II, OSIRIS **2**, 265-302 (1986).

[2] W. E. Lamb, R. C. Retherford, Fine structure of the hydrogen atom by a microwave method, Phys. Rev. **72**, 241–243 (1947).

[3] Moscatelli, A. Deviations from 2, Nat. Phys. **13**, 518 (2017).

[4] J. E. Nafe, E. B. Nelson, I. I. Rabi, The hyperfine structure of atomic hydrogen and deuterium **71**, 914–915 (1947).

[5] N. Bezginov, Measurement of the 2S1/2, f = 0 – 2P1/2, f = 1 transition in atomic hydrogen, Dissertation (2020).

[6] C. G. Parthey, A. Matveev, J. Alnis, B. Bernhardt, A. Beyer, R. Holzwarth, A. Maistrou, R. Pohl, K. Predehl, T. Udem, T. Wilken, N. Kolachevsky, M. Abgrall, D. Rovera, C. Salomon, P. Laurent, T. W. Hänsch, Improved measurement of the hydrogen 1S-2S transition frequency, Phys. Rev. Lett. **107**, 203001 (2011).

[7] M. P. A. Jones, R. M. Potvliege, M. Spannowsky, Probing new physics using rydberg states of atomic hydrogen, Phys. Rev. Research **2**, 013244 (2020).

[8] A. Brandt, S. Cooper, C. Rasor, Z. Burkley, A. Matveev, D. Yost, Measurement of the $2S_{1/2}$ – $8D_{5/2}$ transition in hydrogen, Phys. Rev. Lett. **128**, 023001 (2022).

[9] Z. Burkley, C. Rasor, S. F. Cooper, A. D. Brandt, D. C. Yost, Yb fiber amplifier at 972.5 nm with frequency quadrupling to 243.1 nm, Appl. Phys. B **123**, 5 (2017).

[10] Z. Burkley, A. D. Brandt, C. Rasor, S. F. Cooper, D. C. Yost, Highly coherent, watt-level deep-UV radiation via a frequency-quadrupled yb-fiber laser system, Appl. Opt. **58**, 1657–1661 (2019).

[11] J. T. M. Walraven, I. F. Silvera, Helium temperature beam source of atomic hydrogen, Rev. Sci. Instr. **53**, 1167–1181 (1982).

[12] S. F. Cooper, A. D. Brandt, C. Rasor, Z. Burkley, D. C. Yost, Cryogenic atomic hydrogen beam apparatus with velocity characterization, Rev. Sci. Instr. **91**, 013201 (2020).

[13] E. Narevicius, A. Libson, M. F. Riedel, C. G. Parthey, I. Chavez, U. Even, M. G. Raizen, Coherent slowing of a supersonic beam with an atomic paddle, Phys. Rev. Lett. **98**, 103201 (2007).

[14] S. Scheidegger, D. Schlander, J. A. Agner, H. Schmutz, P. Jansen, F. Merkt, Barrier-discharge source of cold hydrogen atoms in supersonic beams: Stark effect in the 1S-2S transition, J. Phys. B: At. Mol. Opt. Phys. **55**, 155002 (2022).

[15] P. J. Mohr, D. B. Newell, B. N. Taylor, CODATA recommended values of the fundamental physical constants: 2014, Rev. Mod. Phys. **88**, 035009 (2016).

[16] E. Tiesinga, P. J. Mohr, D. B. Newell, B. N. Taylor, CODATA recommended values of the fundamental physical constants: 2018, Rev. Mod. Phys. **93**, 025010 (2021).

[17] D. Djukanovic, T. Harris, G. von Hippel, P. Junnarkar, H. Meyer, D. Mohler, K. Ottnad, T. Schulz, J. Wilhelm, H. Wittig, Isovector electromagnetic form factors of the nucleon from lattice QCD and the proton radius puzzle, Phys. Rev. D **103**, 094522 (2021).

[18] P. J. Mohr, B. N. Taylor, D. B. Newell, CODATA recommended values of the fundamental physical constants: 2010 J. Phys. Chem. Ref. Data **41**, 043109 (2012).

[19] M. Horbatsch, E. A. Hessels, Tabulation of the bound-state energies of atomic hydrogen Phys. Rev. A **93**, 022513 (2016).

[20] D. Taqqu, F. Biraben, C. A. N. Conde, T. W. Hansch, F. J. Hartmann, P. Hauser, P. Indelicato, P. Knowles, F. Kottmann, F. Mulhauser, C. Petitjean, R. Pohl, P. Rabinowitz, R. Rosenfelder,

J. M. F. Santos, W. Schott, L. M. Simons, Laser spectroscopy of the Lamb shift in muonic hydrogen, Hyperfine Interact. **119**, 311–315 (1999).

[21] P. J. Mohr, B. N. Taylor, CODATA Recommended Values of the Fundamental Physical Constants: 2002, Reviews of Modern Physics, (2005), <https://tsapps.nist.gov/publication/get_pdf.cfm?pub_id=102337>, Accessed March 30, 2023.

[22] J. Flowers, H. Klein, H. Margolis, Hydrogenic systems, frequency standards and fundamental constants, Contemp. Phys. **45**, 123–145 (2004).

[23] F. Kottmann, W. Amir, F. Biraben, C. A. N. Conde, S. Dhawan, T. W. Hänsch, F. J. Hartmann, V. W. Hughes, O. Huot, P. Indelicato, L. Julien, P. Knowles, S. Kazamias, The muonic hydrogen lamb shift experiment at PSI, Hyperfine Interact. **138**, 55–60 (2001).

[24] R. Pohl, R. Gilman, G. A. Miller, K. Pachucki, Muonic hydrogen and the proton radius puzzle, Annu. Rev. Nucl. Part. Sci. **63**, 175–204 (2013).

[25] R. Pohl, A. Antognini, F. Nez, F. D. Amaro, F. Biraben, J. M. R. Cardoso, D. S. Covita, A. Dax, S. Dhawan, L. M. P. Fernandes, A. Giesen, T. Graf, T. W. Hänsch, P. Indelicato, L. Julien, C.-Y. Kao, P. Knowles, E.-O. Le Bigot, Y.-W. Liu, J. A. M. Lopes, L. Ludhova, C. M. B. Monteiro, F. Mulhauser, T. Nebel, P. Rabinowitz, J. M. F. dos Santos, L. A. Schaller, K. Schuhmann, C. Schwob, D. Taqqu, J. F. C. A. Veloso, F. Kottmann, The size of the proton, Nature **466**, 213–216.

[26] Krauth, J. J., et al., The proton radius puzzle, *arXiv preprint arXiv:1706.00696* (2017).

[27] G. W. Bennett, B. Bousquet, H. N. Brown, G. Bunce, R. M. Carey, P. Cushman, G. T. Danby, P. T. Debevec, M. Deile, H. Deng, W. Deninger, S. K. Dhawan, V. P. Druzhinin, L. Duong, E. Efstathiadis, F. J. M. Farley, G. V. Fedotovich, S. Giron, F. E. Gray, D. Grigoriev, M. Grosse-Perdekamp, A. Grossmann, M. F. Hare, D. W. Hertzog, X. Huang, V. W. Hughes, M. Iwasaki, K. Jungmann, D. Kawall, M. Kawamura, B. I. Khazin, J. Kindem, F. Krienen,

I. Kronkvist, A. Lam, R. Larsen, Y. Y. Lee, I. Logashenko, R. McNabb, W. Meng, J. Mi, J. P. Miller, Y. Mizumachi, W. M. Morse, D. Nikas, C. J. G. Onderwater, Y. Orlov, C. S. Ã–zben, J. M. Paley, Q. Peng, C. C. Polly, J. Pretz, R. Prigl, G. zu Putlitz, T. Qian, S. I. Redin, O. Rind, B. L. Roberts, N. Ryskulov, S. Sedykh, Y. K. Semertzidis, P. Shagin, Y. M. Shatunov, E. P. Sichtermann, E. Solodov, M. Sossong, A. Steinmetz, L. R. Sulak, C. Timmermans, A. Trofimov, D. Urner, P. von Walter, D. Warburton, D. Winn, A. Yamamoto, D. Zimmerman, Final report of the E821 muon anomalous magnetic moment measurement at BNL, Phys. Rev D **73**, 072003 (2006).

[28] P. Girotti, Status of the fermilab muon *g*-2 experiment, EPJ Web Conf. **262**, 01003.

[29] A. Beyer, L. Maisenbacher, A. Matveev, R. Pohl, K. Khabarova, A. Grinin, T. Lamour, D. C. Yost, T. W. Hänsch, N. Kolachevsky, T. Udem, The rydberg constant and proton size from atomic hydrogen, Science **358**, 79–85 (2017).

[30] A. Grinin, A. Matveev, D. C. Yost, L. Maisenbacher, V. Wirthl, R. Pohl, T. W. Hänsch, T. Udem, Two-photon frequency comb spectroscopy of atomic hydrogen, Science **370**, 1061–1066 (2020).

[31] N. Bezginov, T. Valdez, M. Horbatsch, A. Marsman, A. C. Vutha, E. A. Hessels, A measurement of the atomic hydrogen lamb shift and the proton charge radius, Science **365**, 1007–1012 (2019)

[32] S. G. Karshenboim, Precision physics of simple atoms and constraints on a light boson with ultraweak coupling, Phys. Rev. Lett. **104**, 220406 (2010).

[33] Yang, Qiaoli, and Shiqin Dong, Probe dark matter axions using the hyperfine structure splitting of hydrogen atoms, *arXiv preprint arXiv:1912.11472* (2019).

[34] A. Grinin, A. Matveev, D. C. Yost, L. Maisenbacher, V. Wirthl, R. Pohl, T. W. Hänsch, T. Udem, Two-photon frequency comb spectroscopy of atomic hydrogen, Science **370**, 1061–1066 (2020).

[35] I. D. Setija, H. G. C. Werij, O. J. Luiten, M. W. Reynolds, T. W. Hijmans, J. T. M. Walraven, Optical cooling of atomic hydrogen in a magnetic trap, Phys. Rev. Lett. **70**, 2257–2260 (1993).

[36] S. Wu, R. C. Brown, W. D. Phillips, J. V. Porto, Pulsed sisyphus scheme for laser cooling of atomic (anti)hydrogen, Phys. Rev. Lett. **106**, 213001 (2011).

[37] C. J. Baker, W. Bertsche, A. Capra, C. Carruth, C. L. Cesar, M. Charlton, A. Christensen, R. Collister, A. C. Mathad, S. Eriksson, A. Evans, N. Evetts, J. Fajans, T. Friesen, M. C. Fujiwara, D. R. Gill, P. Grandemange, P. Granum, J. S. Hangst, W. N. Hardy, M. E. Hayden, D. Hodgkinson, E. Hunter, C. A. Isaac, M. A. Johnson, J. M. Jones, S. A. Jones, S. Jonsell, A. Khramov, P. Knapp, L. Kurchaninov, N. Madsen, D. Maxwell, J. T. K. McKenna, S. Menary, J. M. Michan, T. Momose, P. S. Mullan, J. J. Munich, K. Olchanski, A. Olin, J. Peszka, A. Powell, P. Pusa, C. Ã. Rasmussen, F. Robicheaux, R. L. Sacramento, M. Sameed, E. Sarid, D. M. Silveira, D. M. Starko, C. So, G. Stutter, T. D. Tharp, A. Thibeault, R. I. Thompson, D. P. van der Werf, J. S. Wurtele, Laser cooling of antihydrogen atoms, Nature **592**, 35–42 (2021).

[38] S. D. Hogan, A. W. Wiederkehr, H. Schmutz, F. Merkt, Magnetic trapping of hydrogen after multistage zeeman deceleration, Phys. Rev. Lett. **101**, 143001 (2008).

[39] S. D. Hogan, F. Merkt, Demonstration of three-dimensional electrostatic trapping of state-selected rydberg atoms, Phys. Rev. Lett. **100**, 043001 (2008).

[40] M. G. Raizen, Comprehensive control of atomic motion, Science **324**, 1403–1406 (2009).

[41] D. Kielpinski, Laser cooling of atoms and molecules with ultrafast pulses, Phys. Rev. A **73**, 063407 (2006).

[42] I. C. Lane, Production of ultracold hydrogen and deuterium via doppler-cooled feshbach molecules, Phys. Rev. A **92**, 022511 (2015).

[43] S. F. Vázquez-Carson, Q. Sun, J. Dai, D. Mitra, T. Zelevinsky, Direct laser cooling of calcium monohydride molecules, Direct laser cooling of calcium monohydride molecules, New J. Phys. **24**, 083006 (2022).

[44] R. L. McNally, I. Kozyryev, S. Vazquez-Carson, K. Wenz, T. Wang, T. Zelevinsky, Optical cycling, radiative deflection and laser cooling of barium monohydride (^{138}Ba^{1}H), New J. Phys. **22**, 083047 (2020).

[45] A. Huber, B. Gross, M. Weitz, T. W. Hänsch, Two-photon optical Ramsey spectroscopy of the 1*S*-2*S* transition in atomic hydrogen, Phys. Rev. A **58**, R2631–R2634 (1998).

[46] R. Fulton, A. I. Bishop, M. N. Shneider, P. F. Barker, Controlling the motion of cold molecules with deep periodic optical potentials, Nat. Phys. **2**, 465–468 (2006).

[47] S. L. Campbell, R. B. Hutson, G. E. Marti, A. Goban, N. Darkwah Oppong, R. L. McNally, L. Sonderhouse, J. M. Robinson, W. Zhang, B. J. Bloom, J. Ye, A fermi-degenerate three-dimensional optical lattice clock, Science **358**, 90–94 (2017).

[48] C. J. Bustamante, Y. R. Chemla, S. Liu, M. D. Wang, Optical tweezers in single-molecule biophysics, Nature **1**, 25 (2021).

[49] T. M. Graham, Y. Song, J. Scott, C. Poole, L. Phuttitarn, K. Jooya, P. Eichler, X. Jiang, A. Marra, B. Grinkemeyer, M. Kwon, M. Ebert, J. Cherek, M. T. Lichtman, M. Gillette, J. Gilbert, D. Bowman, T. Ballance, C. Campbell, E. D. Dahl, O. Crawford, N. S. Blunt, B. Rogers, T. Noel, M. Saffman, Multi-qubit entanglement and algorithms on a neutral-atom quantum computer, Nature **604**, 457–462 (2022).

[50] M. B. Dahan, E. Peik, J. Reichel, Y. Castin, C. Salomon, Bloch oscillations of atoms in an optical potential, Phys. Rev. Lett. **76**, 4 (1996).

[51] R. H. Parker, C. Yu, W. Zhong, B. Estey, H. MÃ¼ller, Measurement of the fine-structure constant as a test of the standard model, Science **360**, 191–195 (2018).

[52] A. D. Cronin, J. Schmiedmayer, D. E. Pritchard, Optics and interferometry with atoms and molecules, Rev. Mod. Phys. **81**, 1051–1129 (2009).

[53] M. Prevedelli, L. Cacciapuoti, G. Rosi, F. Sorrentino, G. M. Tino, Measuring the newtonian constant of gravitation g with an atomic interferometer, Philos. Trans. Royal Soc. A PHILOS T R SOC A **372**, 20140030 (2014).

[54] S. F. Cooper, Z. Burkley, A. D. Brandt, C. Rasor, D. C. Yost, Cavity-enhanced deep ultraviolet laser for two-photon cooling of atomic hydrogen, Opt. Lett. **43**, 1375–1378 (2018).

[55] W. Gerlach, O. Stern, Der experimentelle nachweis der richtungsquantelung im magnetfeld, Z. Physik **9**, 349–352 (1922).

[56] I. I. Rabi, S. Millman, P. Kusch, J. R. Zacharias, The molecular beam resonance method for measuring nuclear magnetic moments. The magnetic moments of $_3Li^6$, $_3Li^7$ and $_9F^{19}$, Phys. Rev. **55**, 526–535 (1939).

[57] P. Kusch, H. M. Foley, The magnetic moment of the electron, Phys. Rev. **74**, 250–263 (1948).

[58] E. Vliegen, F. Merkt, Stark deceleration of hydrogen atoms, J. Phys. B: At. Mol. Opt. Phys. **39**, L241–L247 (2006)

[59] N. Vanhaecke, U. Meier, M. Andrist, B. H. Meier, F. Merkt, Multistage Zeeman deceleration of hydrogen atoms, Phys. Rev. A **75**, 031402 (2007).

[60] F. C. Fehsenfeld, K. M. Evenson, H. P. Broida, Microwave discharge cavities operating at 2450 MHz, Rev. Sci. Instrum. **36**, 294–298 (1965).

[61] W. Steckelmacher, A review of the molecular flow conductance for systems of tubes and components and the measurement of pumping speed, Vacuum **16**, 561–584 (1966).

[62] P. Clausing, The flow of highly rarefied gases through tubes of arbitrary length, J. Vac. Sci. Technol. A **8**, 636–646 (1971).

[63] W. H. Bröhl, H. Hartmann, On constant molecular gas flow through cylindrical tubes. A note concerning the information content of Clausing's equations, Vacuum **31**, 117–118 (1981).

[64] R. Bisson, L. Philippe, M. Châtelet, Angle-resolved study of hydrogen abstraction on Si(100) and Si(111): Evidence for non-activated pathways, Surf. Sci. **600**, 4454–4463 (2006).

[65] H. Jiang, Dynamics of hydrogen atoms scattering from surfaces, *Dissertation* (2017).

[66] S. N. Sami, M. Sanati, R. P. Joshi, Simulations of hydrogen outgassing and sticking coefficients at a copper electrode surface: Dependencies on temperature, incident angle and energy, Phys. Rev. Research **3**, 013203 (2021).

[67] M. Rondeau, L. Isnard, R. Arés, Point-to-source path tracing Monte Carlo to compute the clausing and distribution functions in high-vacuum systems, Phys. Rev. Fluids **2**, 073401 (2017).

[68] R. Siegel, *Thermal Radiation Heat Transfer, Fourth Edition* (CRC Press) (2001).

[69] I. Martínez, Heat transfer and thermal radiation modelling, (1995-2023), <http://imartinez.etsiae.upm.es/ isidoro/tc3/ Heat%20transfer%20and%20thermal%20radiation%20modelling.pdf/>, Accessed 2023/03/30.

[70] D. A. Bell, H. F. Hess, G. P. Kochanski, S. Buchman, L. Pollack, Y. M. Xiao, D. Kleppner, T. J. Greytak, Relaxation and recombination in spin-polarized atomic hydrogen, Phys. Rev. B **34**, 7670–7697 (1986).

[71] M. J. Yoo, T. J. Greytak, Thermal conductivity and accommodation coefficient of spin-polarized atomic-hydrogen gas, Phys. Rev. B **52**, 7215–7229 (1995)

[72] B. J. Wood, H. Wise, Kinetics of hydrogen atom recombination on surfaces, J. Phys. Chem. **65**, 1976–1983 (1961).

[73] H. Wise, B. J. Wood, Reactive collisions between gas and surface atoms, Adv. At. Mol. Opt. Phys. **3**, 291–353 (1968).

[74] A. A. Bergh, Atomic hydrogen as a reducing agent, Bell Syst. Tech. J. **44**, 261–271 (1965).

[75] J. T. M. Walraven, R. v. Roijen, T. W. Hijmans, Chapter: Atomic hydrogen in a magnetic trapping field. In: Bassani, G.F., Inguscio, M., Hänsch, T.W. (eds) The Hydrogen Atom. Springer, Berlin, Heidelberg, 112-122 (1989). <https:doi.org/10.1007/978-3-642-88421-4_11>, Accessed 2023/03/30.

[76] I. F. Silvera, J. T. M. Walraven, Direct determination of the temperature and density of gaseous atomic hydrogen at low temperature by atomic beam techniques, Phys. Lett. A **74**, 193–196 (1979).

[77] F. L. Walls and D. A. Howe, "A Passive Hydrogen Maser Frequency Standard," 32nd Annual Symposium on Frequency Control, Atlantic City, NJ, USA, (1978). <doi: 10.1109/FREQ.1978.200280 492-498>, Accessed 2023/03/30.

[78] A. C. Anderson, W. Reese, J. C. Wheatley, Thermal conductivity of some amorphous dielectric solids below 1K, Rev. Sci. Instrum. **34**, 1386–1390 (1963).

[79] P. Pierini, Fundamental of cryogenics (for superconducting RF technology), *arXiv preprint arXiv:1307.8286* (2013).

[80] P. Duthil, Material properties at low temperature, *arXiv preprint arXiv:1501.07100* (2015).

[81] A. L. Woodcraft, Predicting the thermal conductivity of aluminium alloys in the cryogenic to room temperature range, Cryogenics, **45**, 421–431 (2005).

[82] Y. A. Lebedev, M. V. Mokeev, Gas temperature in the plasma of a low-pressure electrode microwave discharge in hydrogen, Plasma Phys. Rep. **29**, 226–230, (2003).

[83] Z. Qing, D. K. Otorbaev, G. J. H. Brussaard, M. C. M. van de Sanden, D. C. Schram, Diagnostics of the magnetized low-pressure hydrogen plasma jet: Molecular regime, J. Appl. Phys. **80**, 1312–1324 (1996).

[84] B. Couillaud, T. W. Hänsch, S. G. MacLean, High power CW sum-frequency generation near 243 nm using two intersecting enhancement cavities, Opt. Comm. **50**, 127 – 129 (1984).

[85] C. Zimmermann, V. Vuletic, A. Hemmerich, T. Hänsch, All solid state laser source for tunable blue and ultraviolet radiation, Appl. Phys. Lett. **66**, 2318–2320 (1995).

[86] N. Kolachevsky, J. Alnis, S. D. Bergeson, T. Hänsch, Compact solid-state laser source for 1S-2S spectroscopy in atomic hydrogen, Phys. Rev. A **73**, 021801 (2006).

[87] A. Beyer, J. Alnis, K. Khabarova, A. Matveev, C. G. Parthey, D. C. Yost, R. Pohl, T. Udem, T. W. Hänsch, N. Kolachevsky, Precision spectroscopy of the 2S-4P transition in atomic hydrogen on a cryogenic beam of optically excited 2S atoms, Ann. Phys. (Berl.) **525**, 671–679 (2013).

[88] The ALPHA Collaboration, G. B. Andresen, M. D. Ashkezari, M. Baquero-Ruiz, W. Bertsche, P. D. Bowe, E. Butler, C. L. Cesar, M. Charlton, A. Deller, S. Eriksson, J. Fajans, T. Friesen, M. C. Fujiwara, D. R. Gill, A. Gutierrez, J. S. Hangst, W. N. Hardy, R. S. Hayano, M. E. Hayden, A. J. Humphries, R. Hydomako, S. Jonsell, S. L. Kemp, L. Kurchaninov, N. Madsen, S. Menary, P. Nolan, K. Olchanski, A. Olin, P. Pusa, C. Ã. Rasmussen, F. Robicheaux, E. Sarid, D. M. Silveira, C. So, J. W. Storey, R. I. Thompson, D. P. v. d. Werf, J. S. Wurtele, Y. Yamazaki, Confinement of antihydrogen for 1,000 seconds, Nat. Phys. **7**, 558–564, (2011).

[89] ATRAP Collaboration, G. Gabrielse, R. Kalra, W. S. Kolthammer, R. McConnell, P. Richerme, D. Grzonka, W. Oelert, T. Sefzick, M. Zielinski, D. W. Fitzakerley, M. C. George, E. A. Hessels, C. H. Storry, M. Weel, A. MÃ¼llers, J. Walz, Trapped antihydrogen in its ground state, Phys. Rev. Lett. **108**, 113002 (2012).

[90] M. Ahmadi, B. X. R. Alves, C. J. Baker, W. Bertsche, E. Butler, A. Capra, C. Carruth, C. L. Cesar, M. Charlton, S. Cohen, R. Collister, S. Eriksson, A. Evans, N. Evetts, J. Fajans, T. Friesen, M. C. Fujiwara, D. R. Gill, A. Gutierrez, J. S. Hangst, W. N. Hardy, M. E. Hayden, C. A. Isaac, A. Ishida, M. A. Johnson, S. A. Jones, S. Jonsell, L. Kurchaninov, N. Madsen, M. Mathers, D. Maxwell, J. T. K. McKenna, S. Menary, J. M. Michan, T. Momose, J. J. Munich, P. Nolan, K. Olchanski, A. Olin, P. Pusa, C. O. Rasmussen, F. Robicheaux, R. L. Sacramento, M. Sameed, E. Sarid, D. M. Silveira, S. Stracka, G. Stutter, C. So, T. D. Tharp, J. E. Thompson, R. I. Thompson, D. P.-v. d. Werf, J. S. Wurtele, - Observation of the 1S-2S transition in trapped antihydrogen **541**, 506 – 510 (2017).

[91] V. Zehnlé, J. C. Garreau, Continuous-wave doppler cooling of hydrogen atoms with two-photon transitions, Phys. Rev. A **63**, 021402, (2001).

[92] D. Gangloff, M. Shi, T. Wu, A. Bylinskii, B. Braverman, M. Gutierrez, R. Nichols, J. Li, K. Aichholz, M. Cetina, L. Karpa, B. JelenkoviÄ‡, I. Chuang, V. VuletiÄ‡, Preventing and reversing vacuum-induced optical losses in high-finesse tantalum (v) oxide mirror coatings, Opt. Express **23**, 18014–18028 (2015).

[93] R. R. Kunz, V. Liberman, D. K. Downs, Experimentation and modeling of organic photocontamination on lithographic optics, J. Vac. Sci. Technol. B **18**, 1306–1313, (2000).

[94] S. Heinbuch, F. Dong, J. J. Rocca, E. R. Bernstein, Gas-phase study of the reactivity of optical coating materials with hydrocarbons by use of a desktop-size extreme-ultraviolet laser, J. Opt. Soc. Am. B **25**, B85–B91 (2008).

[95] Z. Burkley, High-power deep-UV laser for improved and novel experiments on hydrogen, Dissertation (2019).

[96] A. D. Brandt, New measurement of the $2S_{1/2}$-$8D_{5/2}$ transition in atomic hydrogen, Dissertation (2020)

[97] J. Nilsson, J. D. Minelly, R. Paschotta, A. C. Tropper, D. C. Hanna, Ring-doped cladding-pumped single-mode three-level fiber laser, Opt. Lett. **23**, 355–357 (1998)

[98] R. W. P. Drever, J. L. Hall, F. V. Kowalski, J. Hough, G. M. Ford, A. J. Munley, H. Ward, Laser phase and frequency stabilization using an optical resonator, Appl. Phys. B **31**, 97–105 (2018).

[99] D. Goldovsky, V. Jouravsky, A. Pe'er, Simple and robust phase-locking of optical cavities with > 200 KHz servo-bandwidth using a piezo-actuated mirror mounted in soft materials, Opt. Express **24**, 28239–28246 (2016).

[100] K. S. Khaw, A. Antognini, T. Prokscha, K. Kirch, L. Liszkay, Z. Salman, P. Crivelli, Spatial confinement of muonium atoms, Phys. Rev. A **94**, 022716 (2016).

[101] W. E. Lamb, R. C. Retherford, Fine structure of the hydrogen atom. Part I, Phys. Rev. **79**, 549–572 (1950).

[102] H. K. Holt, I. A. Sellin, Time-dependent theory of stark quenching of 2S states in hydrogen and helium, Phys. Rev. A **6**, 508–512 (1972).

[103] M. Diermaier, C. B. Jepsen, B. Kolbinger, C. Malbrunot, O. Massiczek, C. Sauerzopf, M. C. Simon, J. Zmeskal, E. Widmann, In-beam measurement of the hydrogen hyperfine splitting and prospects for antihydrogen spectroscopy, Nat. Comm. **8**, 15749, (2017).

[104] C. Malbrunot, M. Diermaier, M. C. Simon, C. Amsler, S. Arguedas Cuendis, H. Breuker, C. Evans, M. Fleck, B. Kolbinger, A. Lanz, M. Leali, V. Maeckel, V. Mascagna, O. Massiczek, Y. Matsuda, Y. Nagata, C. Sauerzopf, L. Venturelli, E. Widmann, M. Wiesinger, Y. Yamazaki, J. Zmeskal, A hydrogen beam to characterize the ASACUSA antihydrogen hyperfine spectrometer, Nucl. Instrum. Methods Phys. Res. A: Accel. Spectrom. Detect. Assoc. Equip. **935**, 110–120 (2019).

[105] N. Ramsey, *Molecular beams*, The International series of monographs on physics (Clarendon Press), (1985).

[106] H. Fleurbaey, Frequency metrology of the 1s-3s transition of hydrogen: contribution to the proton charge radius puzzle, Dissertation (2017).

[107] D. C. Yost, A. Matveev, A. Grinin, E. Peters, L. Maisenbacher, A. Beyer, R. Pohl, N. Kolachevsky, K. Khabarova, T. W. Hänsch, T. Udem, Spectroscopy of the hydrogen 1s-3s transition with chirped laser pulses, Phys Rev. A **93**, 042509 (2018).

[108] I. Estermann, O. C. Simpson, O. Stern, The free fall of atoms and the measurement of the velocity distribution in a molecular beam of cesium atoms, Phys. Rev. **71**, 238–249 (1947).

[109] J. W. Sheldon, E. J. Manista, Atomic beam determination of the cesium-cesium total scattering cross section. No. NASA-TN-D-3160. (1965).

[110] D. R. Olander, R. H. Jones, W. J. Siekhaus, Molecular beam sources fabricated from multichannel arrays. IV. Speed distribution in the centerline beam, J. Appl. Phys. **41**, 4388–4391 (1970).

[111] G. C. Angel, R. A. Giles, The velocity distribution of atoms issuing from a multi-channel glass capillary array and its implication on the measurement of atomic beam scattering cross sections, J. Phys. B: At. Mol. Phys. **5**, 80–89 (1972).

[112] H. Fleurbaey, S. Galtier, S. Thomas, M. Bonnaud, L. Julien, F. Biraben, F. Nez, M. Abgrall, J. Guéna, New measurement of the 1S-3S transition frequency of hydrogen: Contribution to the proton charge radius puzzle, Phys. Rev. Lett. **120**, 183001 (2018).

[113] M. A. Chieda, E. E. Eyler, Bichromatic slowing of metastable helium, Phys. Rev. A **86**, 053415 (2012).

[114] G. Dong, W. Lu, P. F. Barker, Decelerating and bunching molecules with pulsed traveling optical lattices, Phys. Rev. A **69**, 013409 (2004).

[115] R. Fulton, A. I. Bishop, P. F. Barker, Optical stark decelerator for molecules, Phys. Rev. Lett. **93**, 243004 (2004).

[116] W. A. Bowers, The classical polarizability of the hydrogen atom, Am. J. Phys. **54**, 347–350 (1986).

[117] D. A. Steck, Quantum and atom optics (2007-2022) <http://atomoptics.uoregon.edu/d̃steck/teaching/quantum-optics/quantum-optics-notes.pdf>, Accessed 2023/03/30.

[118] C. M. Rasor, Precision measurement and symmetry properties of metastable hydrogen, Dissertation (2021).

[119] T. W. Hijmans, O. J. Luiten, I. D. Setija, J. T. M. Walraven, Optical cooling of atomic hydrogen in a magnetic trap, J. Opt. Soc. Am. B **6**, 2235–2243 (1989).

[120] E. Narevicius, A. Libson, C. G. Parthey, I. Chavez, J. Narevicius, U. Even, M. G. Raizen, Stopping supersonic beams with a series of pulsed electromagnetic coils: An atomic coilgun, Phys. Rev. Lett. **100**, 093003 (2008).

[121] C.-C. Chen, S. Bennetts, R. González Escudero, F. Schreck, B. Pasquiou, Sisyphus optical lattice decelerator, Phys. Rev. A **100**, 023401 (2019).

[122] N. D. McDonough, T. M. Morrison, G. Gabrielse, Simulation of Decelerating Metastable Hydrogen with the Bichromatic Force, 53rd DAMOP conference, Poster presentation V01.16, **67**(7) 2022.

[123] A. Kawasaki, Magic wavelength for the hydrogen 1S-2S transition, Phys Rev. A **92**, 042507 (2015).

[124] P. Crivelli, N. Kolachevsky, Optical trapping of antihydrogen towards an atomic anti-clock, Hyperfine Interact. **241**, 1–11 (2020).

Appendix A

Differential pumping

The goal of this appendix is to give a short review on some of the important conceptual tools used throughout this chapter related to the design design and operation of a vacuum system. For gas flow in a tube or container as pressure is reduced there are three gas flow regimes, viscous flow, Knudsen flow, and molecular flow, the latter being the regime of an low density atomic beam. In each of these regimes a gas of the same composition with vary significantly and the parameter defines the boundary between flow regimes is called the Knudsen number, $K = l/d$, which is a ratio of the mean free path l of the gas at a specified pressure and temperature to a characteristic dimension of the vessel or pipeline the gas is flowing in, d. The mean free path is related to the size of the particles in the gas and their density as

$$l = \frac{1}{\sigma n}, \tag{A.1}$$

where σ is the collisional cross section (approximately one Bohr radius, a_0, for hydrogen) of the species and n is the number density of the gas. The mean free path is represented in units of distance and can be understood as the average distance a particle will travel before colliding with another particle. This factor is intuitively inversely dependent on the pressure of a gas, since for a fixed volume of gas at a constant temperature, if the pressure decreases, the density decreases, therefore there must be more space between particles. Since at the fixed temperature, the atoms will have the same velocity distribution, collisions will occur less frequently for the greater average spacing of the particles. Roughly speaking, when the mean free path of the gas is much less than the container characteristic dimension, i.e $K \ll 1$, the gas is said to be in the viscous flow regime, and the walls contribute fewer collisions within the gas than intragas interactions. The turn over range where $K \approx 1$ is called Knudsen flow, and the regime describing vacuum and the flow of an effusive molecular beam is called molecular flow where $K \gg 1$. The molecular flow regime

describes typical high vacuum conditions where molecules or atoms can be thought of interacting with the walls of the container or tube many times before they ever interact with each other in free space.

The gas state variables, P, V, N and T (pressure, volume, particle number, and temperature) allow us to determine the flow rates of gas in our vacuum system and are well described by the Ideal Gas law (IGL),

$$PV = Nk_BT \tag{A.2}$$

where $k_B = 1.380649 \times 10^{-23}\,\mathrm{J\,K^{-1}}$ is the Boltzmann constant (exact as of 2018 CODATA [16]). Since we're interested in the flow of gasses through the pipelines of our apparatus and between chambers, we should differentiate Eq. A.4 with respect to time,

$$\frac{\partial(PV)}{\partial t} = k_BT\frac{\partial N}{\partial t} \tag{A.3}$$

where we've assumed the temperature to be constant. Both sides of Eq. A.3 represent an energy flow, which must remain conserved, therefore the flow of energy into and out of one part of a vessel must be equal to the net flow into and out of another part of the vessel. This energy flow per unit time is defined as the "throughput", Q, of a system, defined as $Q = \partial(PV)/\partial t$. In system that has reached steady state where the input throughput of a gas system is equal to the outgoing throughput of the system, there will be a static pressure differential (constant in time) across constrictions in the flow or across vacuum pumps which compress the gas. The static pressure differential between two locations in a system motivates the throughput of gas flow across constrictions. It is then useful to think of the volumetric flow rate of a system, $\partial V/\partial t$ which can be thought of a section of volume per time passing through the pipeline of a vacuum system containing an amount of particles determined by the pressure and temperature of the gas. This quantity is equivalent the useful specification for a vacuum pump, "pumping speed" $S = \partial V/\partial t$, and conductance, $C = \partial V/\partial t$, which can be calculated for a given constriction in the system such as an orifice, long channel, or bend in a pipe. The typical unit for pumping speed and conductance is $\mathrm{L\,s^{-1}}$. It is then evident that

a $\Delta V = I \times R$ Ohm's circuit law analog describes the flow of gasses where the current is replaced by throughput, $I \rightarrow Q$, the voltage difference by pressure differential, $\Delta V \rightarrow \Delta P$, and the resistance with the pipeline or pump conductance, $R \rightarrow 1/C$, giving

$$Q = \Delta P \times C. \tag{A.4}$$

The circuit law for the gas flow allows for a simple method to analyze vacuum systems. Figure A.1 shows examples of how to set up the equivalent resistance circuits for the the analysis of two gas flow systems. The throughput values Q_n add linearly at vacuum chamber intersections like current junctions in a electric circuit, and the mass conservation of gas flow in steady state allows for the circuit to be constructed in series.

Figure A.1b shows a useful example for stepping down the pressure for the UV cavity mirrors which require an environment of $\approx 500\,\mathrm{mTorr}$ of oxygen to keep them from degrading. Because the optical beam must be coupled into the chamber without intracavity windows which would otherwise spoil the enhancement cavity finesse, the oxygen environment must have a hole to allow for the laser beam path to travel. Obviously, this would be bad for the vacuum quality in the spectroscopy region, so the gas must be stepped down in pressure though differential pumping by the time the vessel connects to the main vacuum chamber. This is accomplished by adding low resistances to atmosphere (vacuum pumps) in parallel with highly constricting channels separating each pumpout chamber, as shown in Fig. A.1b. If each pumpout chamber has a significantly greater pumping speed than the conductance of the narrow separation channels, then there will be many orders of magnitude difference in pressure between P_0 and P_f. The conductance of an orifice by itself is

$$C_o = \frac{A\bar{v}}{4}, \tag{A.5}$$

where A is the area of the orifice, and $\bar{v}$ is the mean speed of the gas, which is approximately $445\,\mathrm{m\,s^{-1}}$ for oxygen at room temperature. For gasses flowing in the molecular flow regime, gas to surface collisions do not follow the hard sphere "billiard ball" bounce model. Instead, a better

model is that particles adsorb to the surface for some amount of time where they have some surface mobility to move around and interact before desorbing back into the volume following a $\cos\theta$

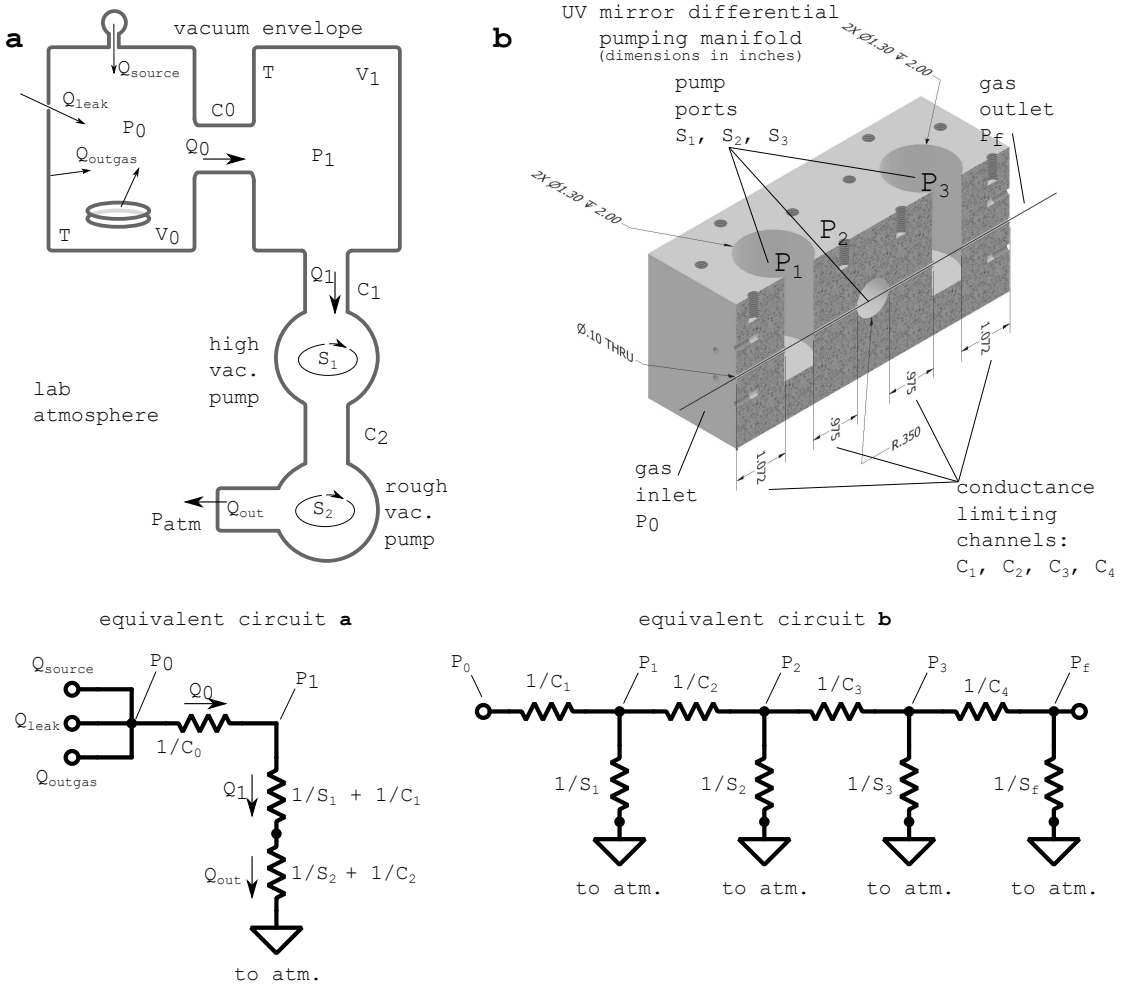

Figure A.1: Two gas circuits. **a)** An example of dealing with leaks, outgassing, and a source gas load on a vacuum chamber with multiple chambers and in steady state. The throughput adds linearly like electrical current and the circuit is accomplished by treating inverse conductances as resistances. In steady state, the conductance out to atmosphere and through the vacuum pumps is equal to the throughput transferred between chambers 0 and 1, assuming there are no additional gas loads in chamber 1. In the case of **a**, one could determine the size of the combined leaks (virtual and real) if the pressure in each chamber is measured and the pumping speeds and chamber geometry is known using just a simple voltage divider model. **b)** A useful vacuum circuit for differentially pumping the oxygen in the UV enhancement cavity chambers. The dimensions of what is used in the current apparatus are labeled which yields the channel conductance of $C_1 = C_2 = C_3 = C_4 = C \approx 0.07\,\mathrm{L\,s^{-1}}$, and each chamber is pumped with a $80\,\mathrm{L\,s^{-1}}$ turbo pump connected by approximately 4 feet of 1" diameter bellows, yielding a reduced effective conductance of $S_1 = S_2 = S_3 = S_4 = S \approx 6\,\mathrm{L\,s^{-1}}$. With $P_0 \approx 0.5\,\mathrm{Torr}$ of oxygen on the input and a turbo pump with $300\,\mathrm{L\,s^{-1}}$ pumping speed in the final chamber, this brings $P_f < 1\times10^{-6}\,\mathrm{Torr}$ which is compatible with our spectroscopy chamber requirements.

angular dependence [61, 62, 65, 66]. This effect means that an orifice that is elongated into a tube will have further reduced conductance as gas flowing from high to low pressure well have some probability of flowing back toward the higher pressure region. The adjustment to the conductance in a long round tube of gas was solved analytically by Clausing in [62], where he found that

$$C_{tube} = C_o \frac{4d}{3l}, \tag{A.6}$$

where C_o is the opening conductance to the channel, d is the diameter of the channel, and l is the length of the channel. For the example in Fig. A.1b, the channels between vacuum pump out regions have conductances of $C \approx 0.07\,\mathrm{L\,s^{-1}}$. The vacuum pump out regions have $80\,\mathrm{L\,s^{-1}}$ turbo pumps connected by approximately 120 cm long by 4 cm diameter hoses. This gives an effective pumping speed of the differential pumping chambers of approximately $S = 6\,\mathrm{L\,s^{-1}}$. The final chamber has an unthrottled $S_T = 300\,\mathrm{L\,s^{-1}}$ turbo pump directly coupled to the chamber. Evaluating the voltage divider circuit in Fig. A.1b with these conductances, we get

$$P_f = \xi_1^3 \times \xi_2 \times P_0, \tag{A.7}$$

where ξ_1 and ξ_2 are the two voltage divider ratios,

$$\xi_1^3 = \frac{R_s}{R_s + R_c},$$

$$\xi_2 = \frac{R_{S_T}}{R_{S_T} + R_c},$$

and the equivalent resistances are inverse of the conductances, as in $R_c = 1/C$, $R_S = 1/S$, and $R_{S_T} = 1/S_T$. Plugging in the values calculated from the channel geometry leads to a final pressure of $P_f = 9 \times 10^{-7}$ Torr which is manageable for the spectroscopy chamber.

When the system is not yet in steady state, such as in initial pumpdown or when a new gas load is introduced, the pressure and particle number in each vessel will vary in time. This is however a useful way to determine the minimum pressure, or base pressure, and pumpout time for a system

with some quantity of unknown leaks and limited pumping speed. In this case differentiating the ideal gas law by time, the pressure will decrease at a rate directly proportional to the time varying particle density,

$$\frac{\partial P}{\partial t} = \frac{k_B T}{V} \frac{\partial N}{\partial t} \tag{A.8}$$

where V is assumed to be a known volume of the chamber. Since $P(t)$ is easy to measure over time on a pressure gauge, then the particle flow, $\frac{\partial N}{\partial t}$, is easy to determine from this data. This is a useful way to calibrate throughput by charging the chamber to an initial pressure with a fixed initial quantity of gas at a constant temperature and volume and measure the rate of pressure decrease over time. This is used in the Section 2.1 to determine the atomic beam flux.

Appendix B

Decelerator application to pulsed supersonic beams

Our deceleration method and apparatus was built around and designed for an effusive atomic beam. Effusive beams have been the central component to all of the high precision spectroscopy experiments in hydrogen to date. However, because pulsed supersonic beams have much narrower velocity spectra as compared to effusive thermal beams, significant effort has been contributed to the development of a high quality supersonic source of hydrogen. Typically supersonic beams are not great candidates for high precision measurements because they are pulsed and require long wait times between pulses (many milliseconds to seconds on average) where precision experiments require high atomic fluxes and high duty cycles to achieve the SNR required to verify and quantify systematic checks. Despite these disadvantages, the narrow starting velocity distribution offers significant benefit and with enough development supersonic hydrogen beams could be seen in the future of precision hydrogen spectroscopy and other experiments. Previous demonstrations of deceleration of atomic hydrogen beams in fact were accomplished using a pulsed supersonic source [39, 40]. Unfortunately however, the methods using pulsed magnetic field deceleration require valiant efforts controlling high-current high-field solenoids, and has not since been demonstrated to improve a precision measurements. Recently, the Merkt group in France has demonstrated an impressive new form of pulsed supersonic hydrogen beam [14] which has 15 mK axial temperatures which are centered as low as 1200 m/s. The method of deceleration we have developed and demonstrated in the last two chapters in fact has the ability to target this velocity range very ideally, and accomplish a full deceleration of a supersonic pulse to a stop during one optical pulse using reasonable laser powers and optoelectronic performance that have been demonstrated to date. A single stage of our deceleration method can can be used in place of multi-stage pulsed magnetic field decelerators for experiments originally envisioned for use with pulsed supersonic beams.

To explore the performance requirements and expectations to decelerate or stop a pulse of hydrogen atoms from a supersonic source, we performed Monte Carlo (MC) simulations of the optical lattice interacting with a pulsed beam of atoms with conditions similar to that of [14]. The cryogenic system from [14] is capable of producing an atomic beam with a Gaussian shaped velocity distribution centered at 1200 m/s and a FWHM width of 14 m/s. This velocity distribution is shown in Fig. B.1

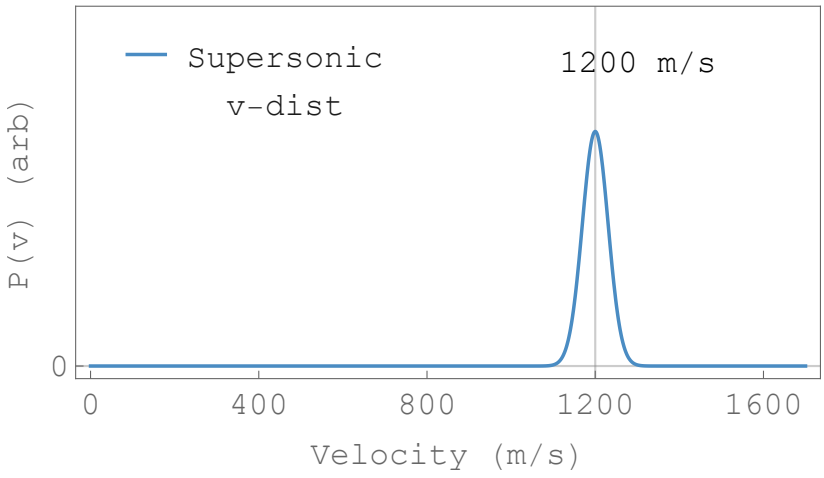

Figure B.1: Gaussian velocity distribution used in the Monte Carlo simulation of decelerating a pulsed supersonic expansion source of atomic hydrogen based on the work in [14].

The MC simulation for this investigation assumed a even spatial distribution of atomic initial trajectories, and the Gaussian velocity profile for the initial phase space. We also assumed that there would be 4.2 W of available 486 nm laser light which could be focused to a 80 micron flat top intensity profile. This is so that each atom in the transverse direction experiences the same force due to a relatively uniform intensity profile. The optical lattice deflection angle was removed so that the deceleration force would be applied directly coaxial with the pulsed supersonic beam direction. Atomic initial conditions were randomly selected from the phase space weighted by the Gaussian velocity profile, and the atomic trajectories and excited state population (quenching) were tracked using the same simulation code as from Chap. 5.

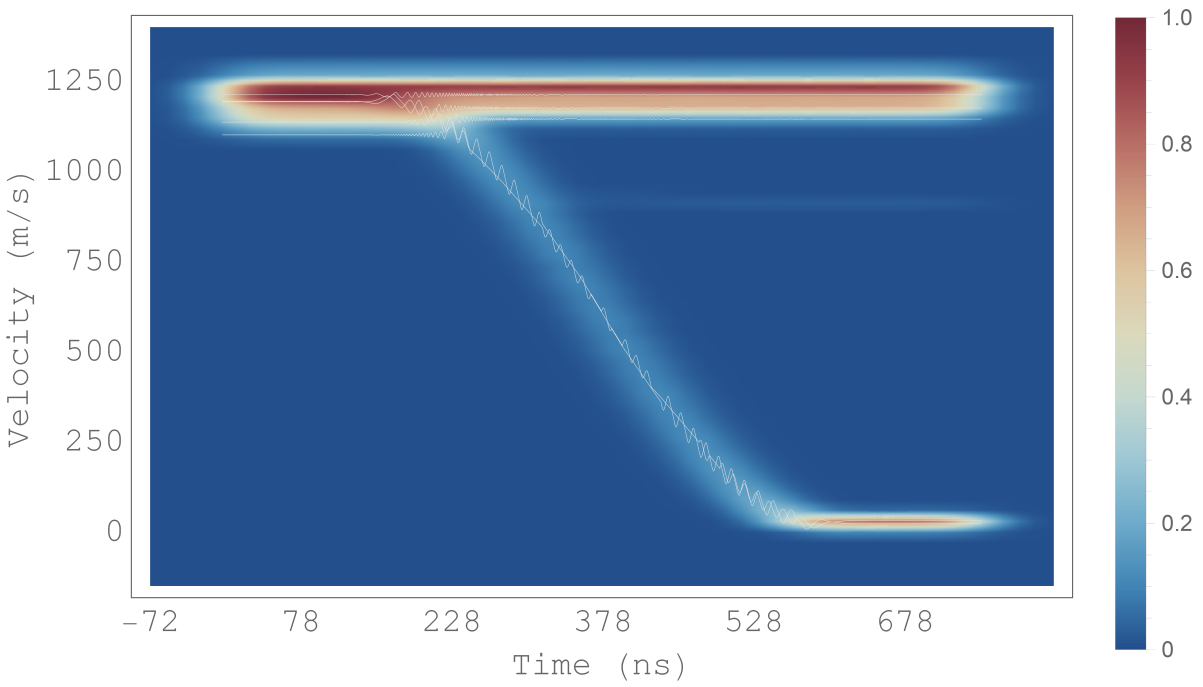

Figure B.2: Deceleration simulation results for a pulsed supersonic atomic beam with gaussian initial velocity distribution from [**?**]. The fraction of atoms decelerated to a near stop depends on the trap depth of the lattice, determined by the intensity and detuning of the optical beams.

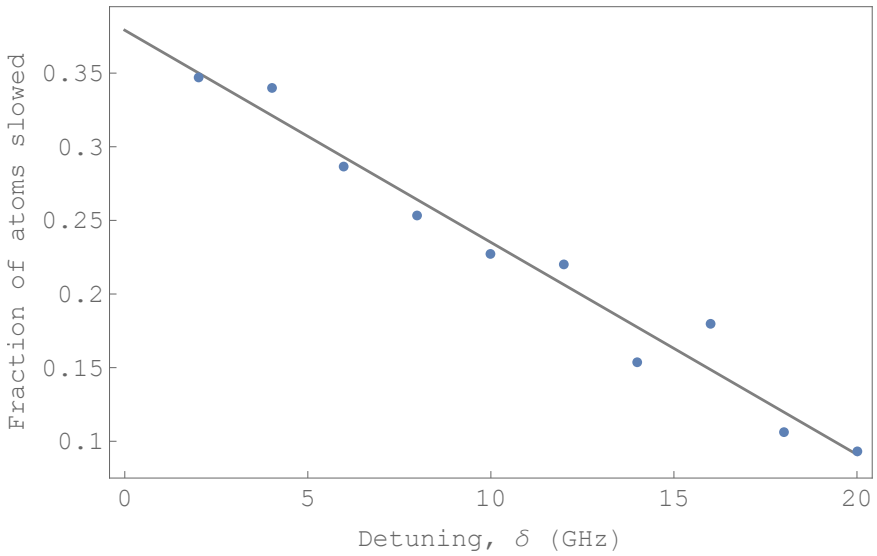

Figure B.3: Simulated fraction of atoms decelerated of the gaussian velocity distribution for a fixed intensity over a varied detuning. This does not include quenching of the atoms through excitation of the 2S-4P transition and spontaneous emission.

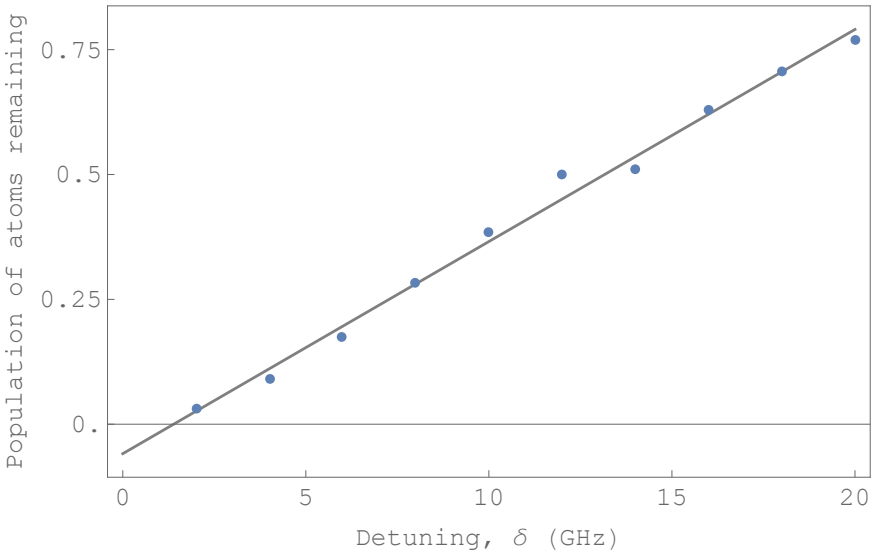

Figure B.4: Simulated fraction of atoms quenched through spontaneous emission from the off resonant excitation of the 2S-4P transition.

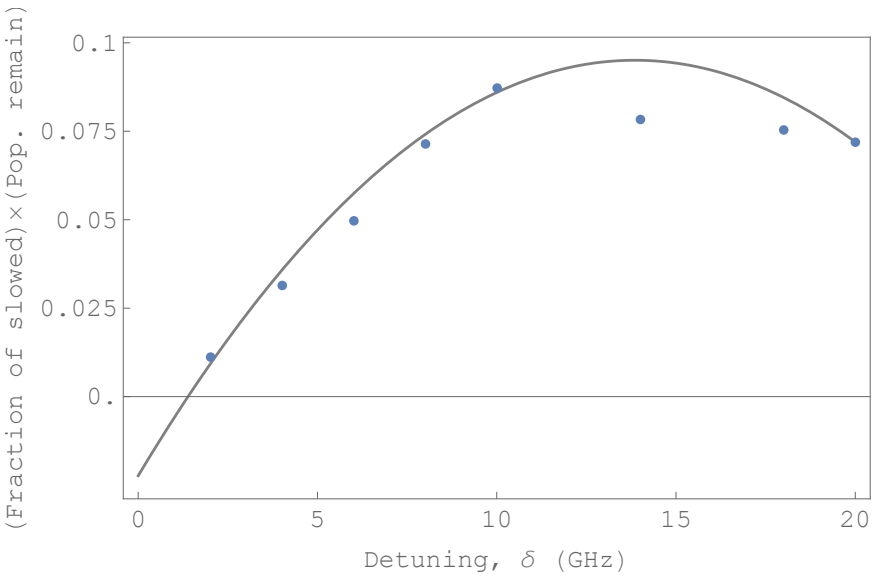

Figure B.5: Combination of deceleration fraction and spontaneous emission loss to give the approximate optimal detuning range of the optical lattice which occurs around 10 GHz. The fit is a quadratic.

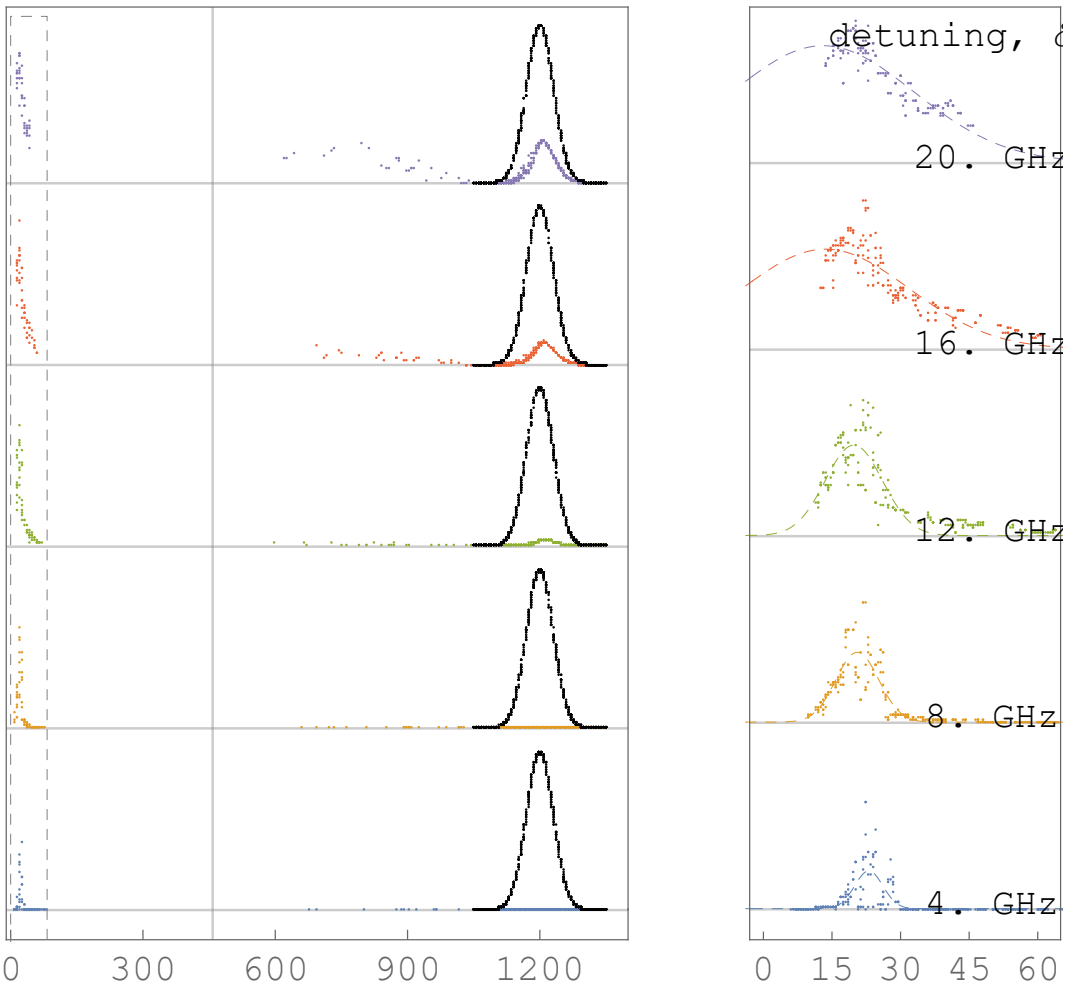

Figure B.6: Monte Carlo simulation of the overall effect a deceleration pulse has on the velocity distribution. Initial gaussian velocity distribution is in black. As can be seen by the reduction of the distribution near the initial gaussian. Lower detunings a significant amount of spontaneous emission occurs for the unslowed atoms as can be seen by the reduction of atoms at the gaussian profile.

Appendix C

MOSFET shutter control

Shuttering of the slowing laser was implemented using a Conoptics model 380 electro optical modulator (capacitance $C_{EO} = 180\,\text{pF}$, $V_\pi = 92\,\text{V}$ at 500 nm) in amplitude modulation configuration and was driven using a home built MOSFET circuit and was capable of generating the 30 ns pulses shown in Fig. 5.11. Pulse generation to switch the MOSFET gate was controlled by pulse generator (AVTECH 1015-B-FLTA, ebay $525) with a maximum repetition frequency of 1 MHz. Our target optical shuttering speed was on the order of 10 ns rise and fall time. With the relatively fast target speed, along with the relatively high desired output voltage range of $90-180$V, the relatively large capacitance of the EO required specialized circuit design to successfully meet the EO shutter constraints. To drive rapidly drive a high voltage with a large current capability, we chose a high power switching MOSFET based driver circuit. A few MOSFET part numbers that would work are IRFU214, IRF710, and IRF720. For our work we chose MOSFET P/N IRF720. These MOSFET's have high gate capacitance (on the order of 420 pF) meaning a standard function generator or pulse generator would not be able to supply enough current to fully turn on the MOSFET gate to drive current drain to source. Therefore, we also require a low-side MOSFET driver chip to step up the input pulse signal to supply the appropriate current. We chose part number EL7104CN as the low-side gate driver because of its fast rise and fall times ($\approx$7 ns. An overview circuit schematic is shown in fig. C.1 along with the SPICE model simulation we used to predict the validity of the circuit.

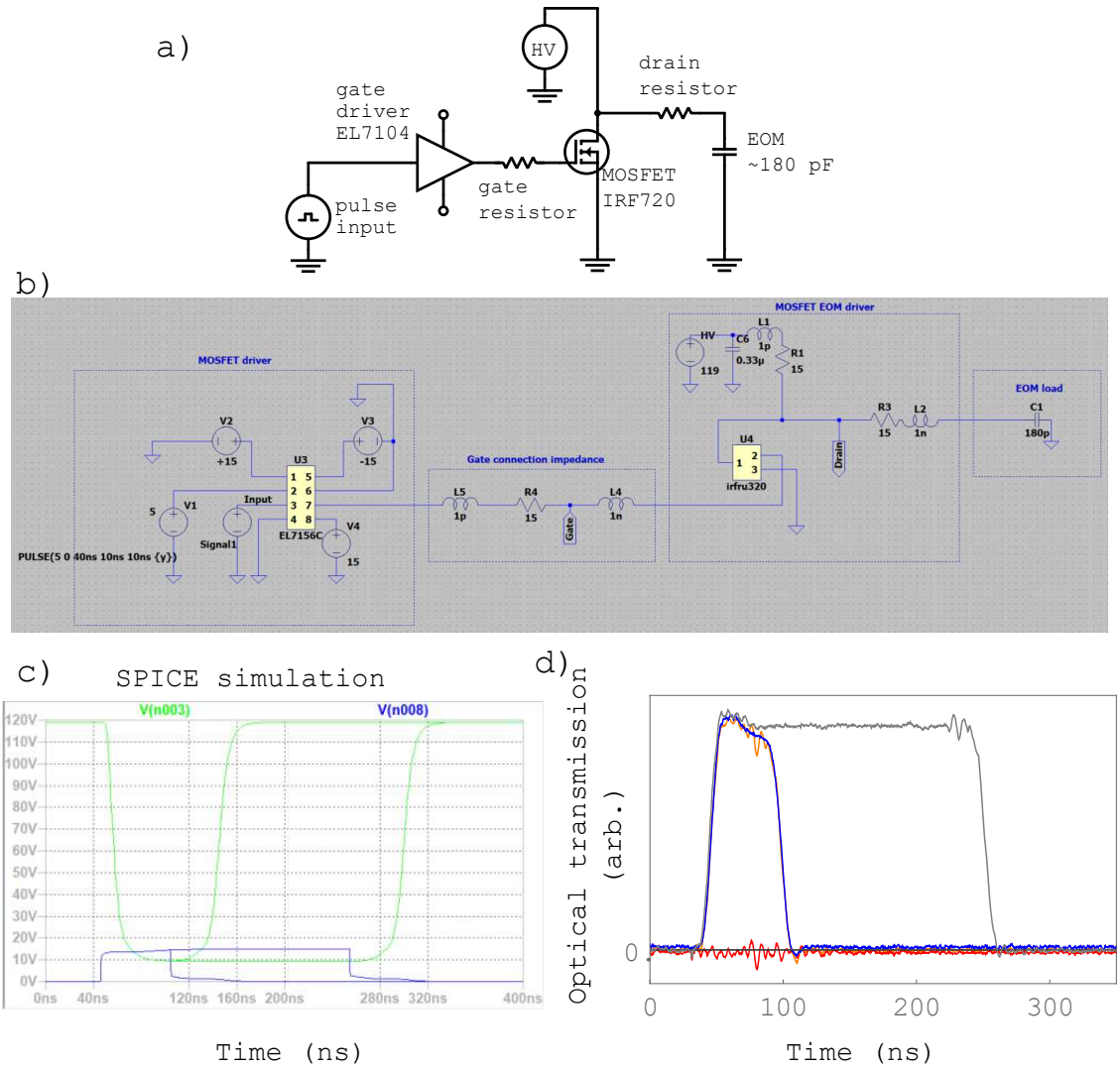

Figure C.1: MOSFET EOM shutter driver circuit. **a)** Pulse driver input is current amplified with a MOSFET gate driver (EL7104). While the MOSFET is open, charge accumulates on the EOM plates, and the MOSFET (IRF720) acts as a switch to short the charge built up on the EOM plates to ground. A gate resistor is added in to reduce on/off switching ringing. **b)** LTSPICE model circuit using components with nearest model performance specifications. None ideal impedances are simulated on the gate and drain of the MOSFET. **c)** results of SPICE simulation which show that the turn on and turn off times are sufficiently fast. Notice the voltage does not reach all of the way to 0 V, this is due to the drain-source impedance of the ON state MOSFET. This leads to an imperfect shuttering of the laser beam to full intensity. **d)** Shutter driver performance as measured by photodiode signal transmitted through the EOM device.